MINERALOGY AND GEOCHEMISTRY OF PB, ZN AND AG MINE TAILINGS ORIGINATING FROM CARBONATE-RICH DEPOSITS

A Thesis

by

ROBERTA JEAN MCCLURE

Submitted to the Office of Graduate Studies of
Texas A&M University
in partial fulfillment of the requirements for the degree of

MASTER OF SCIENCE

Approved by:

Co-Chairs of Committee	Bruce Herbert
	Youjun Deng
Committee Member	Richard Loeppert
Head of Department	Richard Giardino

December 2012

Major Subject: Geology

ABSTRACT

Mining for silver, lead, zinc, and copper in Zimapan, Hidalgo State, Mexico has been ongoing since 1576. Unsecured tailings heaps and associated acid mine drainage have presented problems related to soil quality, water quality, and dust emission control in the Zimapan area. Objectives of the study of the mine tailings are (1) to determine mineralogy of the tailings in order to identify acid-producing minerals and identify heavy metals at risk for release in acidic conditions, and (2) to quantify carbonate minerals and (3) to determine heavy metal content that may be released by the products of sulfide mineral weathering. Representative mine tailings have been sampled from a site located north of Zimapan. Mineralogical characterization has been conducted with X-ray diffraction (XRD), and scanning and transmission electron microscopes (SEM and TEM). Total carbonates have been determined the Chittick procedure. X-Ray Fluorescence (XRF) has been utilized to determine total elemental composition. XRD and SEM analyses have confirmed the presence of pyrite and arsenopyrite indicating a potential for acid mine drainage. Calcite has been confirmed to have a significant presence in the unweathered samples by XRD and the Chittick procedure, with some samples containing an average of 19.4% calcite. NAA and XRF have revealed significant concentrations of toxic elements such as As, Pb and Zn in both the oxidized and unoxidized samples.

TABLE OF CONTENTS

LIST OF FIGURES

CHAPTER I

INTRODUCTION, LITERATURE REVIEW AND METHODS

Introduction

Historical and current lead, zinc, silver and copper mining and lack of sufficient regulatory standards in Zimapan, Hidalgo State, Mexico have lead to environmental problems resulting from unsecured tailing heaps. Some environmental problems include acid mine drainage, wind and gravity dispersion of mine tailings, and contamination of soil and water with heavy metals. In order to mitigate these problems, an initial analysis of the tailings must be performed in order to assess the extent of the environmental problems present and to assist in future mitigation strategies.

Sulfide Mineral Oxidation

Sulfide minerals such as pyrite (FeS_2), arsenopyrite (FeAsS), chalcopyrite ($CuFeS_2$) and sphalerite ((Zn, Fe)S) are commonly present in ore deposits of Pb, Zn, Ag and Cu worldwide (e.g. Garcia & Querol, 1991, Courtin-Nomade et al., 2009, Arroyo & Siebe, 2007). These minerals are characterized by the presence of reduced sulfur (S^{2-}) and Fe (Fe^{2+}) in the mineral structures. Mining process exposes these minerals to surface conditions, where oxidation of sulfide minerals occurs in the presence of water and oxygen via the generalized reactions below (Singer & Stumm, 1970):

$$Fe^{2+} + 1/4O_2 + H^+ \rightarrow Fe^{3+} + 1/2H_2O \quad (1)$$

$$FeS_2 + 7/2O_2 + H_2O \rightarrow Fe^{2+} + 2SO_4^{2-} + 2H^+ \quad (2)$$

$$FeS_2 + 7Fe_2(SO_4)_3 + 8H_2O \rightarrow 15FeSO_4 + 8H_2SO_4 \quad (3)$$

$$Fe^{3+} + 3H_2O \rightarrow Fe(OH)_3(s) + 3H^+ \quad (4)$$

During the initial oxidation reaction, Fe(II) is oxidized to Fe(III) (Reaction 1) and S^{2-} to SO_4^{2-} (Reaction 2) to form ferric sulfate (Reaction 3) and iron oxide (Reaction 4). The production of Fe(III) has been established as the rate-determining step of the reaction (Singer & Stumm, 1970). The presence of Fe(III) greatly accelerates the oxidation and acid generation process by oxidizing remaining Fe(II) more efficiently than water and oxygen. Acidophilic bacteria greatly enhance the production of Fe(III) from Fe(II) at low pH (Silverman, 1967). The production of sulfuric acid (Reaction 3) resulting from oxidation of residual sulfide minerals in mine tailings is what leads to acid mine drainage conditions in the field.

Other sulfides present will also oxidize in the presence of oxygen and water. These include sphalerite, chalcopyrite and arsenopyrite. Reactions of arsenopyrite and zinc sulfide are detailed in the following reaction (Corkhill and Vaughan, 2009; Sherwood Lollar, 2005; respectively). Not all sulfides will produce acidity when oxidation occurs, as indicated in the reaction for ZnS following. However, sulfides such as arsenopyrite will produce acidity:

$$ZnS + 2O_2 + Zn^{2+} + SO_4^{2-} \tag{5}$$

$$FeAsS + 7Fe^{3+} + 4H_2O \rightarrow H_3AsO_4 + 8Fe^{2+} + S^0 + 5H^+ \tag{6}$$

Acid Mine Drainage and its Mitigation

Acid mine drainage is caused by exposure of sulfide minerals previously buried within the Earth's crust to water and oxygen via excavation related to mining activities. Exposure results in the oxidation of the sulfide minerals and production of sulfuric acid/acid mine drainage. Acid mine drainage water pH can drop to negative values and tends to be rich in heavy metals such as As, Cu, Pb and Zn due to greater solubility of these metals at lower pHs. Thus, these metals are more easily transported in AMD, leading to contamination of nearby soils and waters.

Mitigation of acid mine drainage is most commonly achieved by the addition of alkaline material such as calcium carbonate (e.g. calcite) directly to potentially acid-producing mine waste. The alkaline material neutralizes the acidity and serves as a pH buffer, which can induce the precipitation of heavy metals in the neutral to basic pH (Evangelou & Zhang, 1995). Calcium carbonate neutralizes acidity via the following reaction (Doner & Grossl, 2002):

$CaCO_3 + 2H^+ \rightarrow Ca^{2+} + CO_{2(g)} + H_2O$ (7)

Dissolution of certain silicates is capable of neutralizing acidity during the exchange of not easily hydrolyzed ions such as Ca, Na, K, Mg and Mn with H+ (Weber et al., 2005, Fernandez-Caliani et al., 2008, Jonckbloedt, 1997). For example, dissolution of wollastonite in acidic conditions can consume H+ via the following reaction (Murphy and Helgeson, 1987):

$CaSiO_3 + 2H^+ \rightarrow Ca^{2+} + H_2SiO_3$ (8)

Fernandez-Caliani et al. (2008) determined that wollastonite dissolution in sulfuric acid raised the pH of acidic water.

Silicate minerals that contain easily hydrolyzed cations such as Fe and Al, however, will not have a net neutralization affect. The hydrolyzation process produces acidity, which would negate any neutralizing affects caused by the release of the cations from the silicate structure.

However, it should be noted that because of the slow reaction rate of rock-forming silicate minerals (Jambor et al., 2000; Jurjove et al., 2002; Garcia et al., 2004; Jonckbloedt, 1997) the potentially acid-neutralizing silicates may offer only limited neutralization potential.

Other methods for mitigation include a cap placed on top of a tailings heap, construction of wetlands to sequester metals in a reducing environment, and other various engineering designs such as alkaline filter drainage mechanisms (Johnson et al., 2005).

Study Site and Zimapan Area Environmental Problems

Like at many acid mine drainage sites around the world, environmental problems related to mining activities in the Zimapan study site include acid mine drainage, and heavy metal and arsenic contamination of surface and ground water. Arsenicosis, or arsenic toxicity, is common in people who reside in the Zimapan area due to high concentrations of arsenic in the public water supply (Armienta et al., 1996).

Many studies have been conducted to determine sources and sinks for As contamination. Mining activities are thought to be a major contributor to contamination. Romero et al. (2006) examined the concentrations and mineralogical constraints of the bulk samples on arsenic mobility of oxidized and unoxidized mine tailing heaps. The study found that the unoxidized tailings contained abundant sulfides, including pyrite, pyrrhotite, sphalerite, galena, chalcopyrite and arsenopyrite. Other minerals identified included quartz and calcite. It was also found that the unoxidized tailings contained high concentrations of As, Pb, Zn and Cu. Oxidized tailings contained K-jarosite, lepidocrocite, goethite, gypsum, kaolinite and gypsum. When compared to the unoxidized tailings, concentrations of As and Pb were relatively high but Zn and Cu were relatively low in the oxidized samples (Romero et al., 2006). Mendez and Armienta (2002) conducted a study on As and heavy metal concentrations in mine tailings using extractions. For oxidized tailings, it was found that most of the As and metals were found in the Fe and Al oxyhydroxide and residual fraction, which includes sulfides and silicate minerals. For unoxidized tailings, most of the As and heavy metals were found to be associated with the residual fraction, which includes sulfide minerals, such as arsenopyrite.

Ongley et al. (2003) studied soil As contamination. The study found that soils nearby mine slag heaps contained as much as 400 mg/kg As, with decreasing concentrations at increasing distance from the heaps. The study also found that As was associated with the upper 100cm of the soil, which would suggest particulate deposition from the tailing heaps.

Surface and groundwater contamination by arsenic has also been studied. Scarcek et al. (2009), found higher concentration of As in shallow groundwater formations downstream of tailing heaps, suggesting As contamination from the tailing heaps. However, Scarcek et al. (2009) and Armienta et al. (2000) found that groundwater As contamination could be partially attributed to natural conditions related to mineralized areas, with higher arsenic concentrations observed downstream of mineralized areas. Garcia et al. (2000) studied arsenic concentrations in river sediments along the Toliman River, which flows within the Zimapan Valley and is the only surface body of water in the valley. The study found that arsenic concentrations were elevated downstream of tailing heaps relative to other segments of the river, with concentrations reaching as high as 6575 mg/kg in the sediments.

Geology of Zimapan Ore Deposits and Formations

The studied tailings heaps originate from the San Francisco (associated with El Monte deposits) and Carrizal mining areas. Both of these mining areas are near the heaps and the city of Zimapan. They share similar geology and mineralization processes. El Monte deposits are characterized by monzonite-latite igneous intrusions in limestone bedrock. New mineralization occurred from the interaction of hydrothermal fluids with the igneous rock and limestone (Garcia & Querol, 1991). The two types of mineralization that occur in these deposits include endoskarn, in which the mineralization occurs on the outside of of the igneous rock in the form of fracture fills, and exoskarn, in which mineralization replaces minerals contained in the igneous rock resulting from exchange of ions (Garcia & Querol, 1991). Typical mineralogy of El Monte deposits includes wollastonite, garnet, quartz, calcite, chlorite, dolomite, sericite, pyrite, sphalerite, arsenopyrite, galena, and chalcopyrite (Garcia & Querol, 1991).

El Carrizal deposits are formed by quartz-monzonite stocks intruding on limestones that have been slightly recrystallized or completely replaced by silicates and other minerals resulting from hydrothermal interaction between the igneous rock and host limestone rock (Garcia & Querol, 1991). Typical mineralogy of El Carrizal deposits include wollastonite, garnet, calcite, diopside, epidote, chlorite, quartz, sphalerite, chalcopyrite, pyrrotite, pyrite and galena (Garcia & Querol, 1991).

More information is needed to identify the potential risk of the tailing heaps considered in this study. The objectives of this study include: (1) to determine mineralogy of the tailings in order to identify acid-producing minerals and identify heavy metals at risk for release in acidic conditions, and (2) to quantify carbonate minerals and (3) to determine heavy metal content that may be released by the products of sulfide mineral weathering. The data collected in this study will aid future studies to potentially mitigate the hazards presented by the Zimapan waste tailing heaps.

Materials and Methods

Site and Background Information

The Zimapan mining area is located in the Sierra Madre Mountains near the town of Zimapan, Hidalgo state. The city of Zimapan is 200 km north of Mexico City (Figure 1). The area has been known for lead, zinc, silver, gold and copper mining for many centuries (Romero, 2006). Historical and modern mining has led to a concentration of uncontained tailing heaps in the area. The study site is located near the city of Zimapan at 20° 49.295 N and 99° 22.431 W and situated in a mountain valley.

There are nine heaps located in the valley of various ages and weathering stages. The older tailing heaps (20 years and more) were piled using a downstream procedure. A dike was built up using coarse tailing materials. Waste slurry from the ore processing plant was directed to the dike, and suspended finer materials were placed upstream and allowed to drain. The method is now in question due to possible engineering instability of the dike due to the unstable angle of the dike. A two-year old heap has been placed using a newer upstream method, in which a geotextile material and gravel are placed at the base of the heap to allow drainage of the tailing suspension upon placement. Coarser tailing particles that are not in suspension are placed directly in front of the dike downstream, and the tailing material suspension is then placed behind the dike upstream. The drain water is collected and sent back to the processing plant for re-use. This method is thought to be more stable than the downstream method.

Tunnels were constructed around three of the tailing heaps to divert water flow around the heaps. Although some water has been diverted, water flow over the heaps had occurred, along which some oxidation had taken place. Wind dispersion of the tailings also occurred as directly observed in the field. Dust dispersions was also indicated by grey dust coatings on nearby structures and vegetation.

Figure 1. Zimapan, Mexico location map and aerial photo of the site. Photo courtesy Google Earth.

Relative weathering stages of the heaps were evaluated in the field based on visual evidence of iron oxides and cementation. The red, orange and/or yellow coloration is a good visual indicator. Some heaps exhibited red, orange and/or yellow cemented crusts, pockets, and horizons that had undergone extensive weathering. Other heaps exhibited less red to yellow coloration to no red, yellow or orange coloration. The heaps showing little to no red, yellow or orange coloration were also less cemented, indicating less weathering had occurred.

A single tailing heap was selected for detailed mineralogical and geochemical analysis. Tailing heap number four was located at the top of the valley relative to the other heaps. The color of the heap was gray, indicating little to no weathering. The heap was originally placed in 1970 following the downstream procedure. At the time of the site visit, there was 20 meters of new tailing material aged approximately three years with particles sorted by size placed atop the tailings aged 40 years. The coarse particles were placed adjacent to the dike downstream, and the fine particles placed upstream of the dike in suspension form. There is an oxidized zone in a drainage ditch at the foot of the heap, presumably from weathering of the tailings placed in the 1970s.

Sampling and Analysis Methods

Sampling was performed along a transect longitudinally across the heap to ensure adequate sampling of both the coarse and the fine tailings. Samples were also taken from the drainage ditch immediately downstream from the heap, where red to yellow oxidized material was present. A total of four samples (4D, 4K, 4L and 4M) were evaluated in the study.

Detailed mineralogical analysis of the samples was carried out using various methods. The bulk sample and the separated sand, silt and clay size fractions were analyzed. A portion of the sample was processed to separate the sand, silt and clay fraction. First, the flocculated and cementing materials were removed. Twenty-five grams of tailing material and 50mL of pH 5 sodium acetate buffer were measured into a 250mL centrifuge bottle. The particles were mixed in the bottle using a vortex mixer. The centrifuge bottle was then placed in a water bath that had been heated to 90° C and allowed to react for 30 minutes. During this time, the bottle was shaken by hand every 10 minutes. If the reaction continued, as indicated by bubbling, the bottle was heated for an additional 20 minutes. The bottle was then centrifuged and the supernatant siphoned out of the bottle. The procedure was repeated three to four more times, or until no bubbles formed during the treatment.

Once the carbonates were destroyed, the sand fraction was separated from the silt and clay fractions by wet sieving the sample through an ASTM 270 sieve. Next, the remaining sample was placed in a 250 mL centrifuge bottle and approximately 100mL of 0.125 g/L, pH 10 sodium carbonate (Na_2CO_3) was added to the sample. The sample was agitated with a vortex mixer in order to disperse the sample. Next, an automatic size fractionator was used to separate the clay from the silt fraction. Dr. Youjun Deng (Texas A&M University, College Station, Texas, USA) designed the automatic size fractionator. The device shakes the samples in 250mL centrifuge bottles for approximately twenty minutes, and allows the particles to settle for 2-4 hours. After the time period has passed for the particles to settle, the fluid was siphoned out automatically into a 4 L plastic beaker. The 250 mL centrifuge bottle containing the sample was then refilled automatically with approximately 100mL of 0.125 g/L, pH 10 sodium carbonate (Na_2CO_3). The size fractionation process was repeated three to four times until the clay particles were separated from the silt particles. Once separated from the clay fraction, the silt fraction was washed several times with dionized water. Washing involved removing the supernatant from the separated silt fraction, contained in the 250 mL centrifuge bottle. The centrifuge bottle was then filled with approximately 100mL of dionized water and shaken vigorously by hand. Following shaking, the bottle was placed in a centrifuge and centrifuged at 750 rounds per minute for 3 minutes. The dionized water rinse process steps were repeated two additional times. Finally, the silt fraction was placed in aluminum trays and allowed to dry in an oven at 40° C. The clay fraction, contained in a 4 L plastic beaker, was flocculated by adding approximately 50 grams of sodium chloride (NaCl) powder to the solution. The fluid above the clay-sized material was removed and the clay was washed several times with dionized water following the same procedure used for washing the silt fraction with dionized water. Once the material was thoroughly washed, the clay fraction was transferred to aluminum trays and dried in an oven at 40° C.

Once dried, the size fractions were prepared for XRD analysis. The sand-sized fraction was ground in a marble mortar and pestle until all particles passed through an ASTM No. 140 sieve. The silt-size and the ground sand-size fractions were loaded into a XRD powder holder by front-loading into the cavity. The mounted samples were analyzed by X-Ray Diffraction. A Brucker D8 ADVANCE (Madison, Wisconsin, USA) X-Ray diffractometer operated at 35 kV and 45mA with a CuKα source was utilized to analyze the samples using X-Ray diffraction.

For clay fraction analysis, portions of the sample were saturated with Mg^{2+} and K^{+}. Samples were washed three times with 0.5M $MgCl_2$ and 1M KCl solutions for the Mg^{2+}- and K^{+} -saturations, respectively. The procedure involved placing 50 mg of the clay-sized fraction into 50 mL centrifuge tubes. Approximately 2 mL of saturation solution ($MgCl_2$ or KCl) was added to the tube. The sample and solution mixture was shaken on a shaker for 20 minutes. Next, the tube was centrifuged at 2000 rpms for 10 minutes and the supernatant removed with a disposable pipette. The procedure was repeated twice and a final repetition was done with dionized water. Oriented slides were prepared for full clay fraction analysis, including one slide each of clays treated with Mg^{2+}-saturation, K^{+}-saturation. The slides were prepared by dropping the clay suspension on glass slides with a disposal pipette and allowing them to air-dry overnight under a watch glass. The slides were then analyzed using XRD. Following the initial XRD analysis, the Mg^{2+}-saturated clay slide was treated with spray-on glycerol treatment for approximately 2 seconds, allowed to air dry under a watch glass for approximately 2 hours and reanalyzed by XRD. Also, following the initial XRD analysis of the K^+-saturated slide at room temperature, the K+-saturated slide was heated to 330° and 550° C and analyzed by XRD immediately following each heat treatment.

Further confirmation of mineral phases was accomplished using electron microscopy for samples 4D, 4K, 4L and 4M. For analysis of the silt fraction, Scanning electron microscopy sessions were carried out using the FEI-QUANTA 600FE-SEM (Hillsboro, Oregon, USA) equipped with a backscattered electron detector using carbon-coated slides. To prepare the slide, a 1 cm-diameter cylindrical stub was fitted with a round piece of tape. A 1:1 sample:dionized water suspension was dropped on the tape and allowed to dry. Next, the tape surface containing the sample was coated with carbon. For analysis of the clay fraction, transmission electron microscopy was carried out using a JEOL 2010 TEM (Toyko, Japan) with selected area electron diffraction (SAED) using holey carbon slides with copper backing. The slides were prepared by dropping a 1:100 sample:dionized water suspension on the holey carbon side of the slide. The slide was allowed to air-dry overnight under a watch glass. Finally, the sample side of the slide was coated with carbon.

X-Ray fluorescence analysis was carried out to determine total elemental composition of the samples. The Mineral Lab, Inc. of Golden, Colorado performed the X-Ray Fluorescence analysis. The lab performed XRF analysis of the bulk powder sample using a Phillips (The Netherlands) simultaneous, wavelength dispersive unit equipped with 26 fixed detectors, 2 scanned detectors and a Rh end-window tube.

Free iron content was determined using the citrate-dithionate-bicarbonate method The acid-base balance was evaluated based on $CaCO_3$ and sulfide mineral quantification. $CaCO_3$ determination was carried out by the Chittick procedure. The Chittick procedure involves the use of a Chittick apparatus (Dreimanis, 1962), which has a flask fitted with a magnetic stirrer that is connected to an adjustable graduated tube and fluid reservoir. The fluid reservoir contains a colored fluid to assist with readings of the gas volume. Dilute (6N) hydrochloric acid is added to the sample flask using a graduated burette. As CO_2 gas is produced from the reaction of the acid with the carbonates in the sample, the fluid in the reservoir is displaced and the displacement measured using the colored fluid as a reference.

Rietveld mineral quantifications were performed and the results are presented in Appendix C. The refinements were accomplished using the Rietveld fitting method (Young, 1993). First, the sample was ground in a marble mortar and pestle until it passed through an ASTM No. 60 sieve. Next, the sample was mixed with a 10% Zincite (ZnO) spike and 0.5% polyvinyl alcohol solution; and loaded into a micronizing mill with cylindrical, 2-cm diameter marble beads. The mixture was ground in the micronizer at 3700 rpms for a total of 5-10 minutes, with the resultant particle size approximately 5-10 μm. Next, the beads were removed and the mixture spray-dried into a spray direr following the design outlined in Hillier (1998). The spray-dried particles were collected on heavy white paper at the bottom of the spray-drier. Next, the spray-dried sample was front loaded into a front-load XRD slide and analyzed using XRD. The XRD pattern was evaluated for mineral phases and models for identified phases downloaded from the International Center for Diffraction Data (Newton Square, Pennsylvania, USA). The models were integrated into a master model and the phases quantified using Diffrac^{PLUS} TOPAS software (Madison, Wisconsin, USA).

CHAPTER II

FIELD OBSERVATIONS

As discussed in the site description, there were several heaps of tailings placed within a mountain valley. The more recent tailings were placed on either side of a dam. The particles were sorted and coarse particles placed on the down-gradient side of the dam, while the fine particles were placed on the up-gradient side of the dam. The most recent tailing heaps were placed such that the leachate drained towards the bottom and eventually downgradient of the heap into a catchment area.

During the initial site investigation, localized acid mine drainage conditions (AMD) were observed. AMD conditions were identified by a red, orange or yellow color occurring on or around existing heaps. The AMD-affected areas were most commonly found at the bottom of the heaps (Figures 2 and 3), where leachate drained from the tailing material. Localized acid mine drainage conditions were also observed along the top of tailing heaps at the site (Figure 4), despite efforts to drain the heaps through tunnels routed alongside the heaps (Figure 5). Within the areas of localized AMD, the yellow, orange and yellow materials were frequently very well cemented. Field pH measurements of cemented material collected from areas affected by AMD showed pH ranged from 1.7-2.0. Abundant carbonate minerals directly adjacent to AMD affected areas were identified using a field HCl test, which involved dropping 1M HCl

Figure 2. Acid mine drainage seeping from the bottom of Tailing Heap 8.

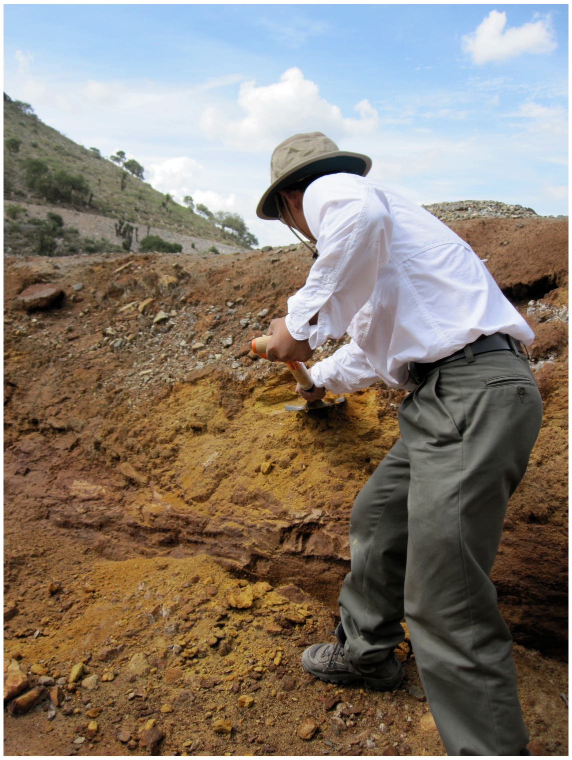

Figure 3. Acid mine drainage conditions observed at the bottom of Tailing Heap 4.

Figure 4. Acid mine drainage conditions observed over the top of Tailing Heap 5.

Figure 5. Tunnel routed alongside the tailings heaps to aid in drainage during rain.

on the sample and observing for bubbling. Bubbling indicates a reaction of the HCl with carbonate minerals. Beneath a crust formed on Tailing Heap 8, copiapite precipitates were observed (Figure 6). Nearby the crust was an unconsolidated, resin-like material consisting of ferric sulfate (Figure 7). These materials have a high solubility and may release "pulses" of contaminants when rain events occur. Sulfate salts were also found along the access road (Figure 8). Given their high solubility, these minerals would also be a potential source of contamination due to potential salinization of rain runoff water.

Based on field observations, Tailing Heap 4 was selected for sampling. The sampling scheme is further detailed in the materials and methods section of this report.

Figure 6. Copiapite observed beneath a crust formed over Tailing Heap 8.

Figure 7. Amorphous, resin-like ferric sulfate observed nearby a crust formed over Tailing Heap 8.

Figure 8. Sulfate salts observed nearby a tailing heap showing signs of acid mine drainage.

CHAPTER III

MINERALOGY

Coarse Unoxidized Mineralogy (4D)

The coarse section analyzed in this section was collected downgradient of the containment dam of Tailing Heap 4 (Figure 9). The tailings consisted of unconsolidated, light gray, dry silty sand. The lack of red, yellow or orange coloration indicated the sample was relatively unoxidized compared to the oxidized samples collected in the field.

Figure 9. Sample location for the coarse unoxidized tailings.

Bulk Sample Mineralogy

X-ray diffraction of the bulk sample (Figure 10) indicated the presence of sulfide minerals, including pyrite (FeS_2), chalcopyrite ($CuFeS_2$), arsenopyrite (FeAsS) and sphalerite ((Zn,Fe)S). Sulfide mineral phases produce acidity once they are oxidized. Arsenopyrite and sphalerite can release As and Zn, respectively, upon oxidation. The presence of gypsum was confirmed by the presence of white precipitates in a 1:1 mixture of sample extract and acetone. Gypsum forms when sulfuric acid generated from sulfide oxidation reacts with $CaCO_3$ according to the reaction below (Fanning et al., 2002):

$$CaCO_3 + H_2SO_4 + H_2O \rightarrow CaSO_4 * 2H_2O + CO_2 \qquad (9)$$

The presence of gypsum in this sample indicates that oxidation of sulfides had occurred during the short exposure to air and water at the tailing dump site. Fe-oxide mineral phases are also an oxidation product of sulfide minerals, as in the following reactions (Evangelou and Zhang, 1995):

$$FeS_2 + 7/2O_2 + H_2O \rightarrow Fe^{2+} + 2SO_4^{2-} + 2H^+ \qquad (10)$$

$$Fe^{2+} + 1/4O_2 + H^+ \rightarrow Fe^{3+} + 1/2H_2O \qquad (11)$$

$$Fe^{3+} + 3H_2O \rightarrow Fe(OH)_3\ (s) + 3H^+ \qquad (12)$$

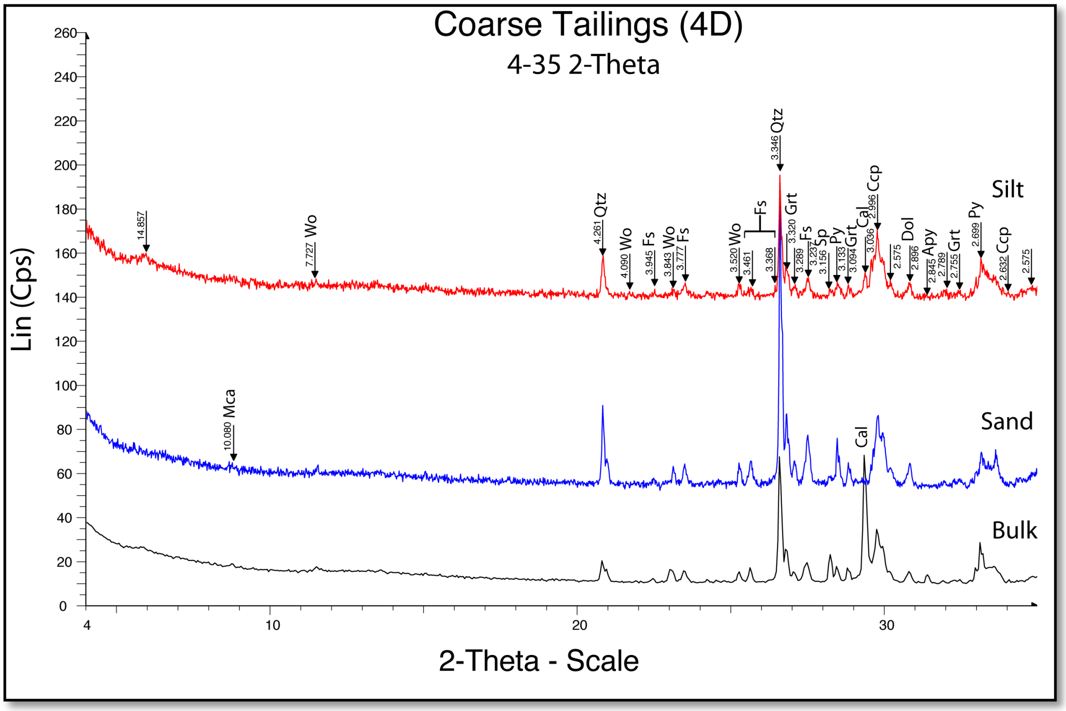

Figure 10. X-Ray Diffraction powder mount analysis of the bulk, sand and silt fractions of the coarse tailing sample. Sand and silt fractions have undergone carbonate destruction procedures. Key: Apy=arsenopyrite, Cal=calcite, Ccp=chalcopyrite, Dol=dolomite, Fs=feldspar, Grt=garnet, Mca=mica, Py=pyrite, Sp=spahlerite, Qtz=quartz, Wo=wollastonite

Fe-oxides were found to have a modest presence at 0.64% (wt %) Fe_2O_3 (Figure 11). However, definite Fe-oxide phases were not identifiable using X-Ray diffraction, presumably due to the low content of the Fe-oxides, the poor crystallinity of the phases, or both.

Carbonate minerals, which can mitigate acidity produced by sulfide mineral oxidation, were identified in the bulk sample by XRD. Both calcite ($CaCO_3$) and dolomite

($CaMg(CO_3)_2$) occurred in the sample. Total carbonates were found to comprise 17.1% (wt %) of the bulk sample (Figure 12).

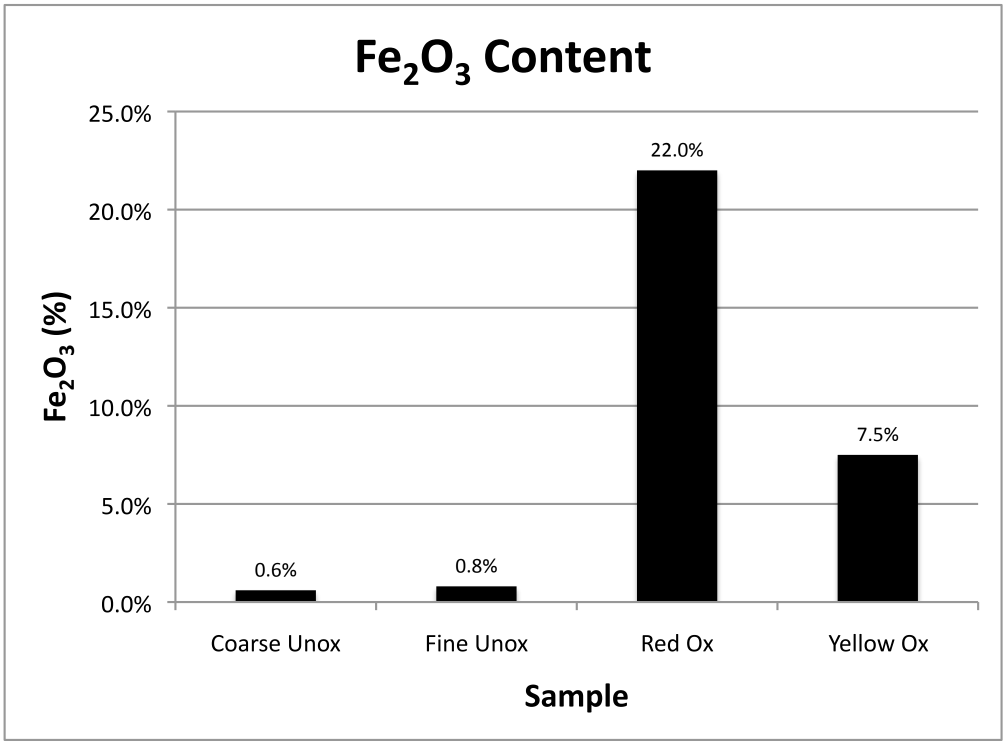

Figure 11: Fe_2O_3 content of coarse and fine oxidized; and red and yellow unoxidized samples.

The bulk sample contained abundant silicates including minerals from the tectosilicate, inosilicate and phyllosilicate groups. Tectosilicate minerals identified are feldspars ($XAl_{(1-2)}$ $Si_{(3-2)}$ O_8, X=Ca, Na, or K) and quartz (SiO_2). The inoslicate mineral identified was wollastonite ($CaSi_3O_8$). Phyllosilicate minerals identified include mica minerals

$[X_2Y_{4\text{–}6}Z_8O_{20}(OH,F)_4]$. The 14.9 Å peak in the bulk sample suggests the presence of secondary phyllosilicate phases, as confirmed in the clay fraction XRD analysis.

Silicate minerals containing Na, Ca, and K will neutralize acidity produced by sulfide mineral oxidation by exchanging these cations for H+ ions (Murphy & Helgeson, 1987; Nicholson, 2003). This sample will have some neutralization capacity via the cation exchange reaction and silicate dissolution. Feldspar minerals and wollastonite will react

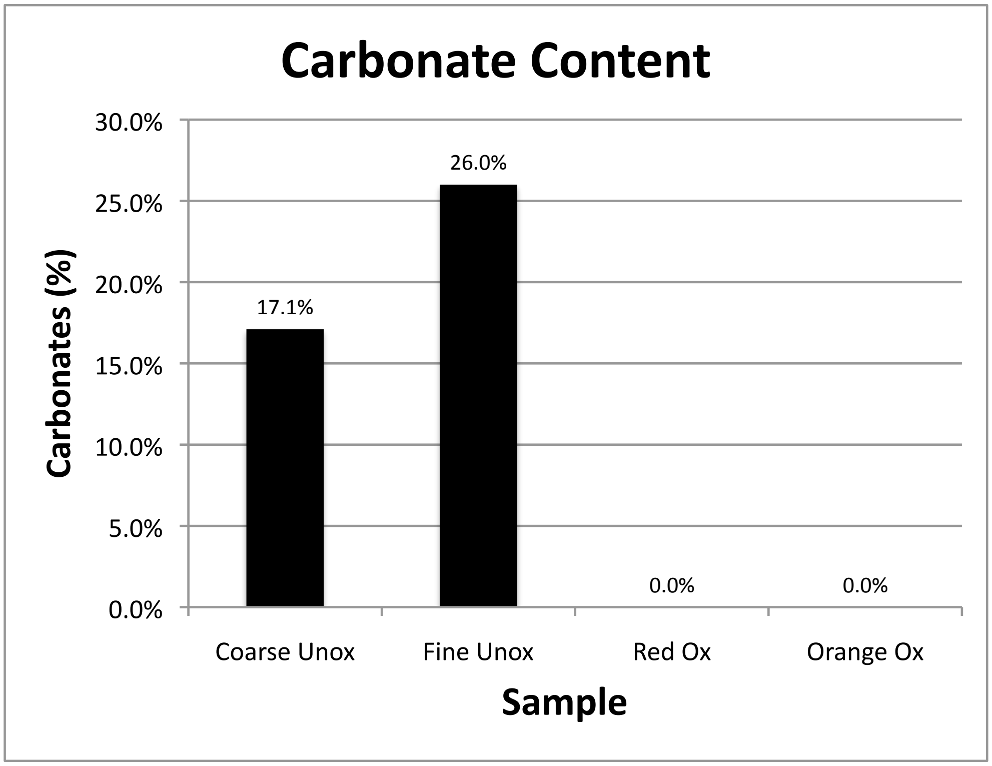

Figure 12: Carbonate quantification of the coarse and fine unoxidized and red and orange oxidized samples.

according to the generalized following reactions (Nicholson, 2003 and Murphy & Helgeson, 1987, respectively):

$$CaAl_2Si_2O_8 + 8H^+ \rightarrow 4H_2O + 2SiO_{2(aq)} + 2Al^{3+} + Ca^{2+} \qquad (13)$$

$$CaSiO_3 + 2H^+ \rightarrow Ca^{2+} + H_2SiO_3 \qquad (14)$$

However, the neutralization capacity of silicate minerals in an acid mine drainage settings is debated. Because of the slow reaction rate of rock-forming silicate minerals (Jambor et al., 2000; Jurjove et al., 2002; Garcia et al., 2004; Jonckbloedt, 1997) the potentially acid-neutralizing silicates present in the sample may offer only limited neutralization potential.

Sand Fraction Mineralogy

Sand-size particles take more time to weather than silt or clay-sized particles due to the smaller specific surface area available for attack by water and other weathering elements. XRD analysis confirmed pyrite was present in the sand fraction with prominent peaks (Figure 10), indicating a significant presence. The presence of pyrite as sand-sized particles may prolong the acid-production risk even after more reactive clay and silt-sized pyrite particles have reacted. Other sulfides such as sphalerite, arsenopyrite and chalcopyrite did not have a significant presence in the sand fraction.

Dolomite persisted in the sand-size fraction despite carbonate destruction treatment and will neutralize acidity produced by sulfide oxidation. However, Fe-oxides may coat sand-size carbonate minerals as a result of iron sulfide oxidation. This may be due to the tendency of gypsum and ferric oxyhydroxides to precipitate on carbonate surfaces during reaction with Fe(III)-rich acid mine waters (Simon et al., 2004). The low specific surface area available for reaction on the sand-size particles may exacerbate this tendency.

Other potentially neutralizing sand-fraction minerals include silicate minerals wollastonite and feldpars, also with prominent peaks on the XRD patterns (Figure 10). Wollastonite has been experimentally found to be coated with Fe-oxide by-products during the Wollastonite dissolution process in Fe(III)-rich acid mine waters (Fernandez-Caliani et al., 2008), which may reduce its acid-neutralizing capability.

Silt Fraction Mineralogy

X-ray diffraction analysis of the silt fraction (Figure 10) revealed similar mineralogy as the bulk sample, including feldspars, wollastonite, carbonates and sulfides. Of the sulfide minerals, pyrite, arsenopyrite, chalcopyrite and sphalerite were identified in XRD with greater prominence, as indicated by greater peak strength, than in the sand fraction. XRD also confirmed the presence of acid-neutralizing carbonates in the silt fraction, including calcite and dolomite. These carbonates persisted despite the carbonate

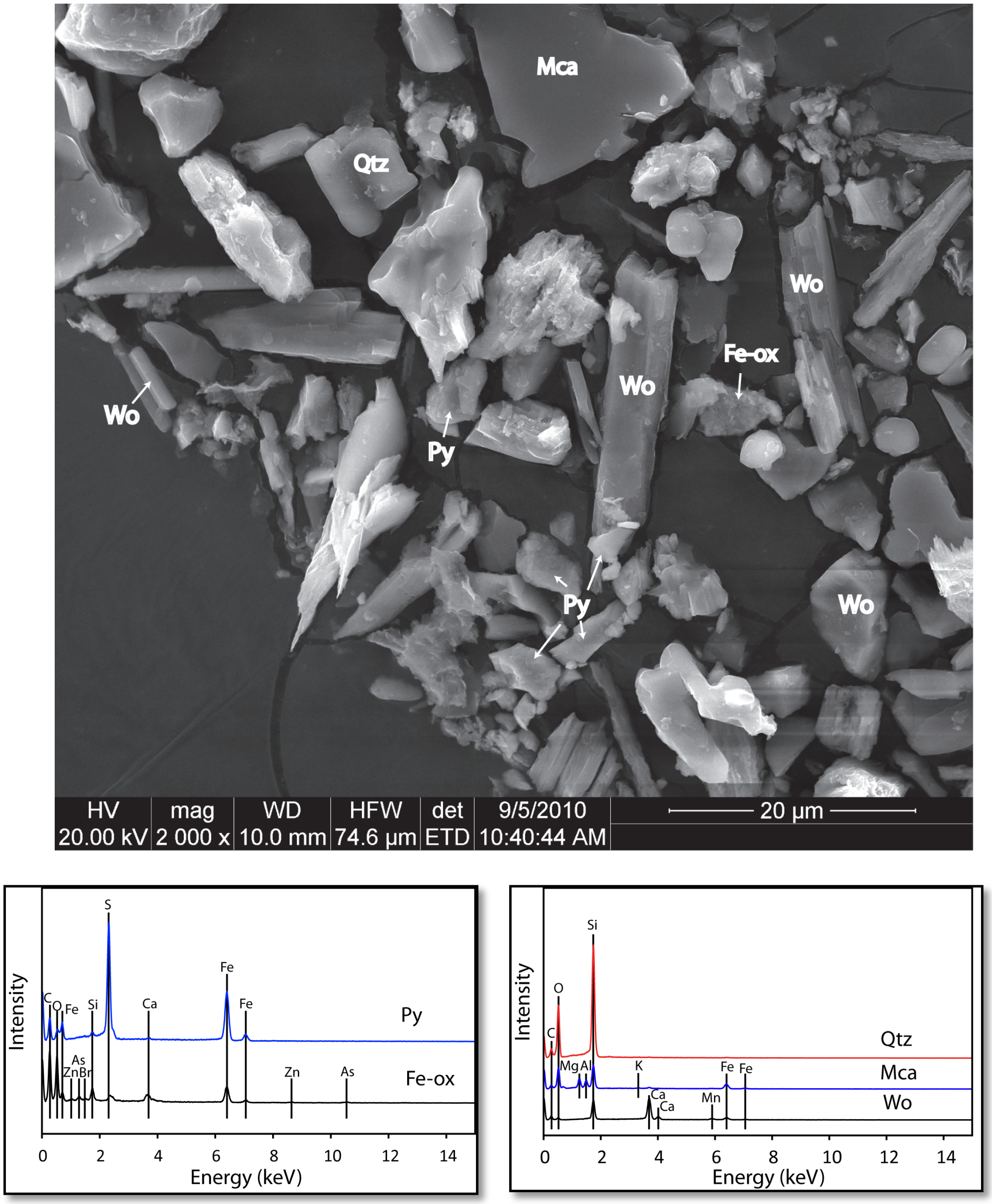

Figure 13. SEM Image and characteristic EDS spectra. Includes wollastonite (Wo), mica (Mca), quartz (Q) and pyrite (Py) particles. Ca and Si peaks on Py and Fe-ox likely due to small wollastonite particles settled on the larger particles.

destruction procedure, which may be due to the high crystallinity of the phases as indicated by sharp XRD peaks. Silicate minerals in the silt fraction confirmed by XRD include wollastonite, feldspars and quartz. Pyrite and Zn-Fe sulfide phases were also confirmed with scanning electron microscopy (SEM) with energy dispersive spectra (EDS). Figure 13 shows multiple pyrite particles mixed with other mineral particles. The pyrite particles are fractured, likely due to crushing during ore processing. The chemical composition, as determined by EDS, is Fe and S at a 1 to 2 molar ratio, congruent with the pyrite chemical formula of FeS_2. Ca and Si peaks at were also associated with some pyrite particles showing the characteristic Fe to S molar ratio of 1 to 2, which may indicate small particles of wollastonite that are resting on or directly adjacent to the pyrite. The suspension slide preparation method, which involves placing a sample suspension on the slide prior to carbon coating, may cause particles to rest atop each other.

The sample has undergone some weathering, as indicated by hydrous ferric oxide (HFO) phases associated with Zn and As; identified by SEM analysis. Figure 13 shows an HFO mineral coating atop another mineral particle. EDS analysis indicated Fe to be present; in addition to As and Zn. These metals typically can be adsorbed on the surface of Fe-oxides or co-precipitated with Fe-oxides as the mineral is forming (Madera et al., 2003; Acera et al., 2006; Moncur et al., 2009). Strong Ca and Si peaks in the spectra may suggest that the Fe-oxide precipitated atop a wollastonite particle. Wollastonite weathering in an environment where pyrite weathering has occurred can lead to

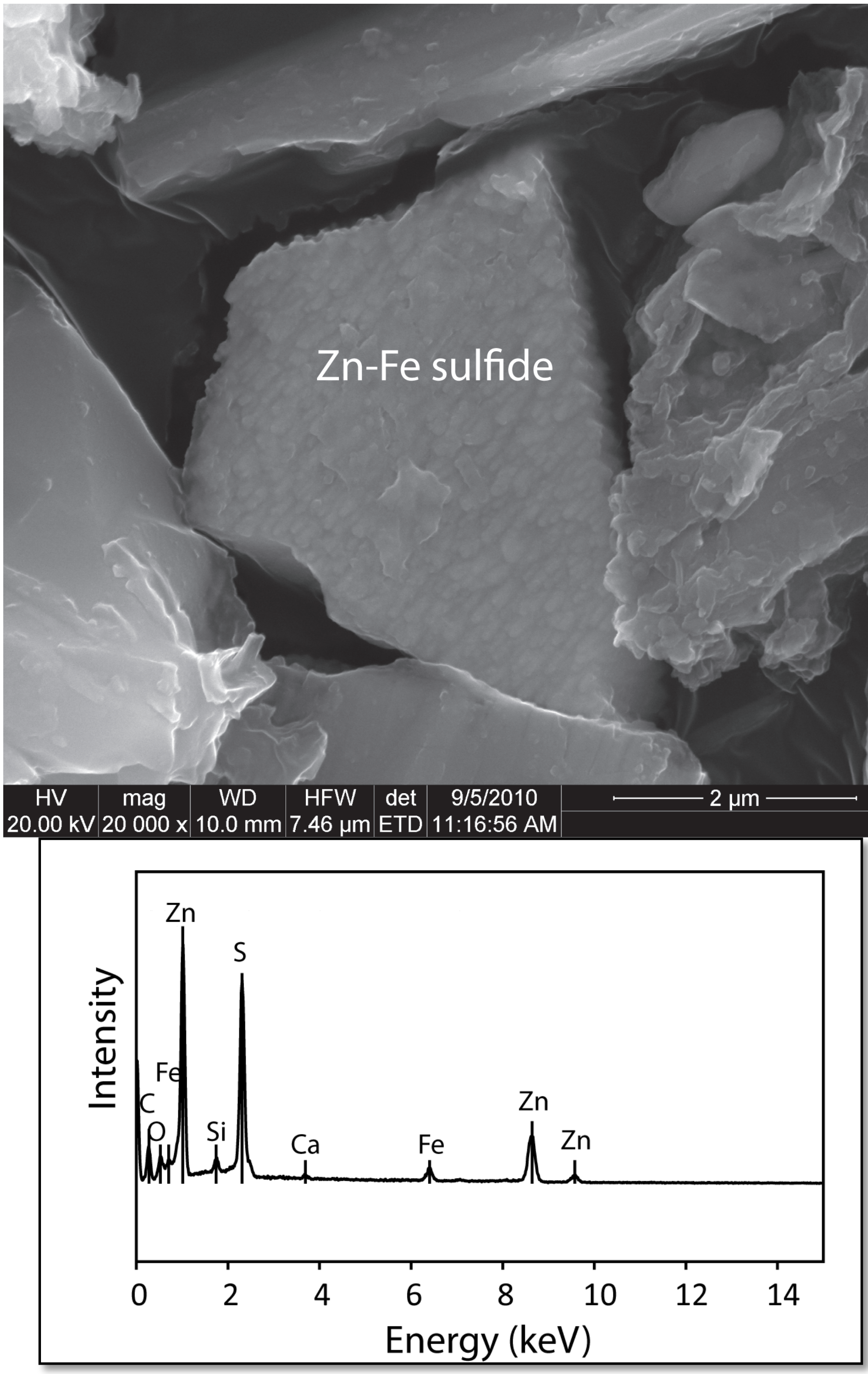

Figure 14: SEM image and EDS spectrum of a Zn-Fe sulfide particle. Ca and Si peaks are possibly due to smaller wollastonite particles settled on the larger particle.

precipitation of Fe-oxides on the wollastonite surface, which in turn can retain As and other metals as found by Caliani et al. (2008). Silicates confirmed in the silt fraction by SEM include wollastonite, mica and quartz. Figure 13 shows the presence of fractured quartz, with its characteristically strong Si and O EDS peaks. Biotite is also present, as confirmed by characteristic Fe, Mg, K and Si peaks and platy morphology. Wollastonite is also apparent with its typical elongated morphology and characteristic Ca and Si peaks. Many wollastonite particles also contained Fe and Mn, which can substitute for Ca in the mineral structure (Klein & Dutrow, 2008).

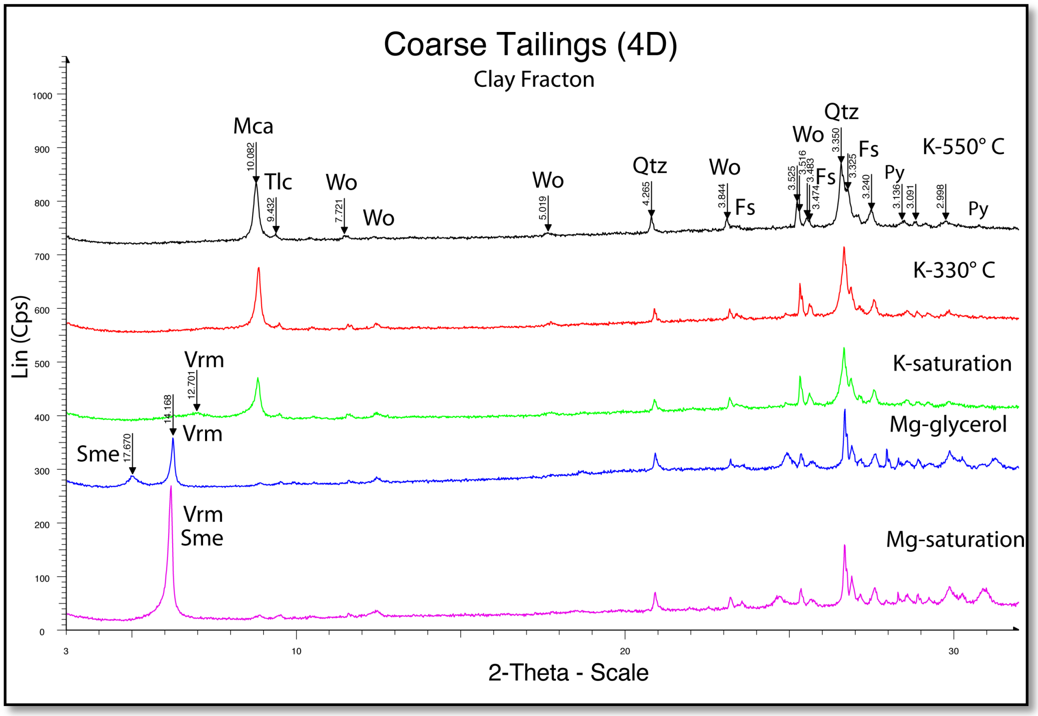

Figure 15 X-Ray Diffraction of oriented slides. Slides have undergone Mg2+ saturation, Mg2+ saturation and glycerol solvation, K+ saturation, K+ saturation and heat treatment to 330 C, and K+ saturation and heat treatment to 550 C.
Key: Fs=feldspars, Mca=mica, Py=pyrite, Sme=smectite, Vrm=vermiculite, Wo=wollastonite

Clay Fraction Mineralogy

Figure 14 shows the image and characteristic EDS spectrum of a zinc-iron sulfide mineral. In addition to acid generation upon dissolution, this mineral will release zinc into the environment.

Oriented clay slides analyzed with X-Ray diffraction (Figure 15) revealed the presence of primary and secondary phyllosilicates in the clay fraction. Mica was identified in the clay fraction, a primary mineral that neutralizes acidity upon dissolution (Nicholson, 2003). Secondary phyllosilicate minerals in the clay fraction confirmed by XRD include kaolinite, vermiculite and smectite. The formation of these secondary minerals will diminish the neutralization capacity of dissolving primary silicate minerals, as found by Nicholson (2003). Other phases identified by XRD analysis in the clay fraction include pyrite, talc, feldspars, wollastonite and quartz.

Transmission electron microscope (TEM) analysis revealed the presence of nanometer-scale amorphous Fe-oxide phases that are associated with As, Mn and Zn forming atop silicate minerals (Figures 16 and 17). Because these phases were not crystalline and had such a low concentration, they were not detectable by XRD analysis. The presence of the amorphous Fe-oxide phases confirms that some weathering has occurred, but that they had not had sufficient time to crystallize. The presence of As, Mn and Zn peaks on the EDS spectra of the iron oxides suggests that these heavy metals either co-precipitated with the iron oxides or adsorbed on the surface of the nanometer sized iron oxides.

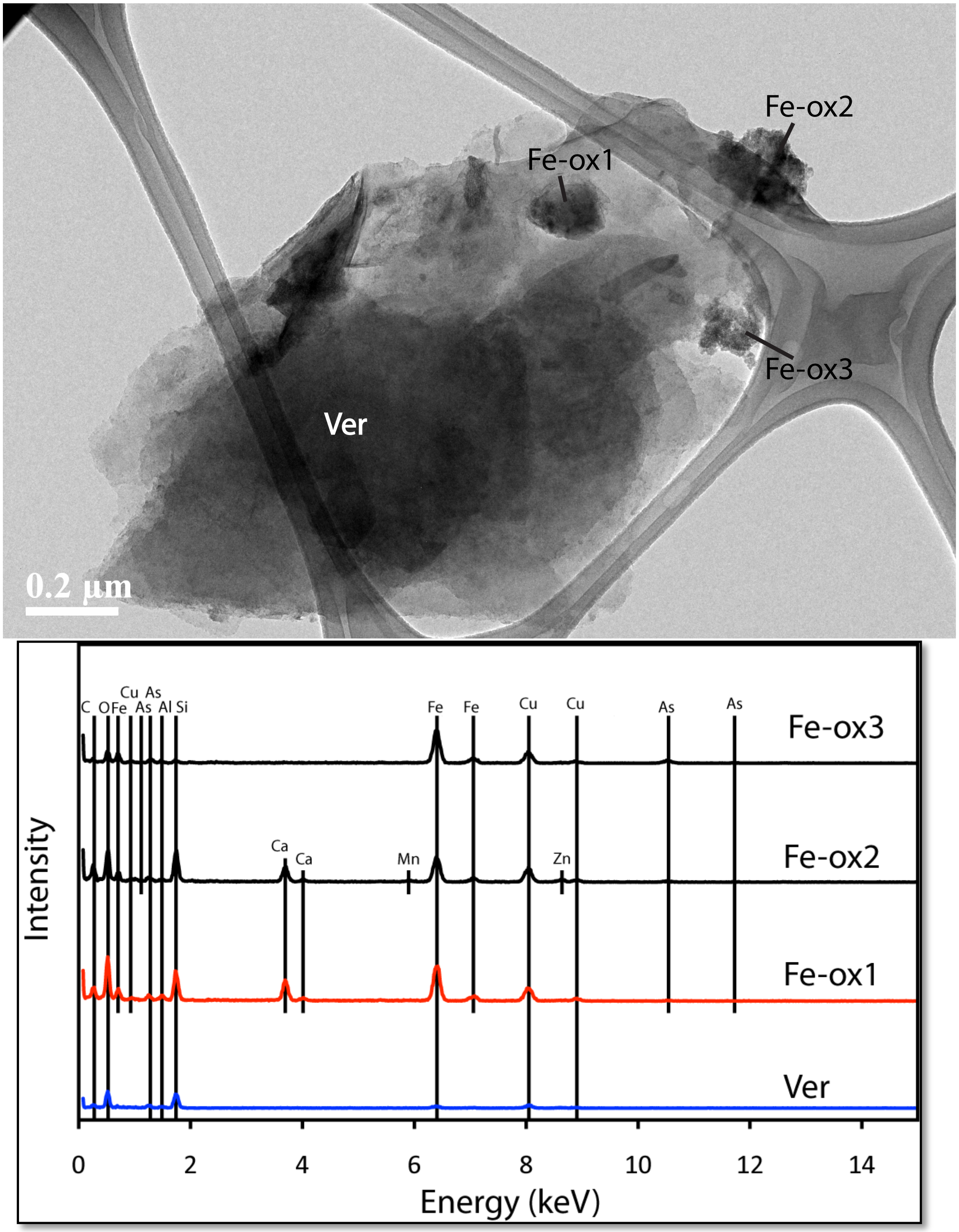

Figure 16: TEM image and EDS spectra. Includes are a vermiculite particle and Fe-oxide particles associated with As, Mn and Zn. The strong Ca and Si peaks present in Fe-ox1 and Fe-ox2 indicate the Fe-oxide particles are on the surface of a wollastonite particle as indicated by d-spacing measurements (Figure 8).

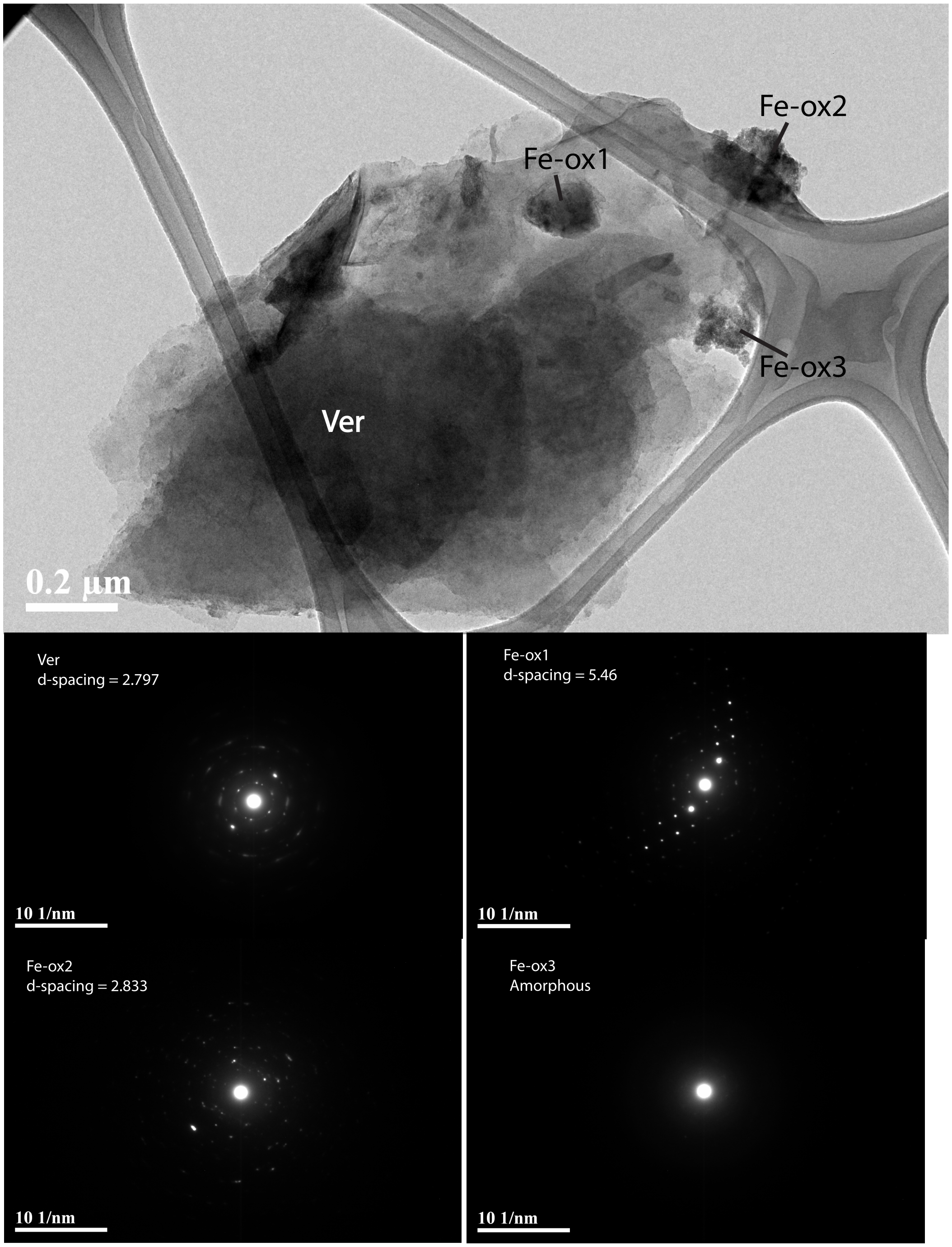

Figure 17: TEM Image and electron diffraction patterns from selected areas. Fe-ox1 and Fe-ox2 exhibit diffraction patterns with d-spacings of 5.46 and 2.833 characteristic of wollastonite. EDS spectra (Figure 7), reveals the presence of strong Ca and Si peaks, which suggests the Fe-oxide particles are amorphous and that the diffraction patterns are resulting from an underlying wollastonite particle. Fe-ox3 is amorphous, as indicated by the diffraction pattern (lower right).

Silicate phases confirmed with TEM analysis include vermiculite and wollastonite (Figures 16 and 17) as well as potassium feldspars as determined with EDS spectra and d-spacing measurements.

Fine Unoxidized Mineralogy (4K)

The fine unoxidized tailings evaluated in this section were collected upgradient from the containment dam of Tailing Heap 4. The sample area was characterized by large cracks and very fine material (Figure 18). The fine tailing material consisted of light gray silty clay. The lack of red, orange or yellow hues in the sample indicated the sample had undergone little to no oxidation.

Figure 18. Fine unoxidized tailings.

Bulk Sample Mineralogy

X-ray diffraction of the bulk sample (Figure 19) revealed similar mineralogy as the coarse unweathered tailings sample, 4D. XRD analyses indicated sulfide minerals, including pyrite (FeS_2), chalcopyrite ($CuFeS_2$), arsenopyrite (FeAsS) and sphalerite ((Zn,Fe)S). As discussed in the previous section (4D Coarse Tailings), sulfide mineral phases produce acidity during the oxidation process. Arsenopyrite, sphalerite and chalcopyrite can release As, Zn, and Cu, respectively, upon oxidation. Gypsum, also a by-product of sulfide oxidation, was confirmed in the bulk sample by the presence of white precipitates in a 1:1 mixture of sample extract and acetone.

Similar to sample 4D, Fe-oxides were found to have a modest presence at 0.85% (wt %) Fe_2O_3 (Figure 19). However, due to the low content of Fe-oxides and/or poor crystallinity of Fe-oxide phases, specific phases were not identifiable using X-ray diffraction.

Carbonates, which may potentially buffer acidity produced by sulfide oxidation, were found in the bulk sample. As in the 4D bulk sample, both calcite ($CaCO_3$) and dolomite ($CaMg(CO_3)_2$) occurred in the sample. Total carbonates were found to comprise 26% (wt %) of the bulk sample (Figure 20), significantly more than in the 4D bulk sample.

The primary silicate mineralogy in the bulk sample of 4K is very similar to that of 4D.

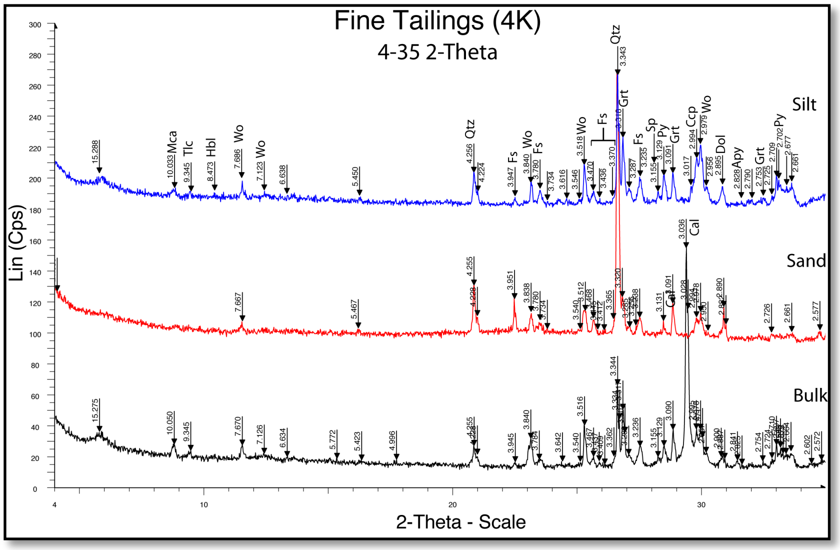

Figure 19. X-Ray diffraction of bulk, sand and silt fractions of 4K. Mineral key: Mca=mica, Tlc=talkc, Hbl=hornblende, Wo=wollastonite, Qtz=quartz, Fs=feldspar, Grt=garnet, Sp=sphalerite, Py=pyrite, Ccp=chalcopyrite, Dol=dolomite, Cal=calcite, Apy=arsenopyrite

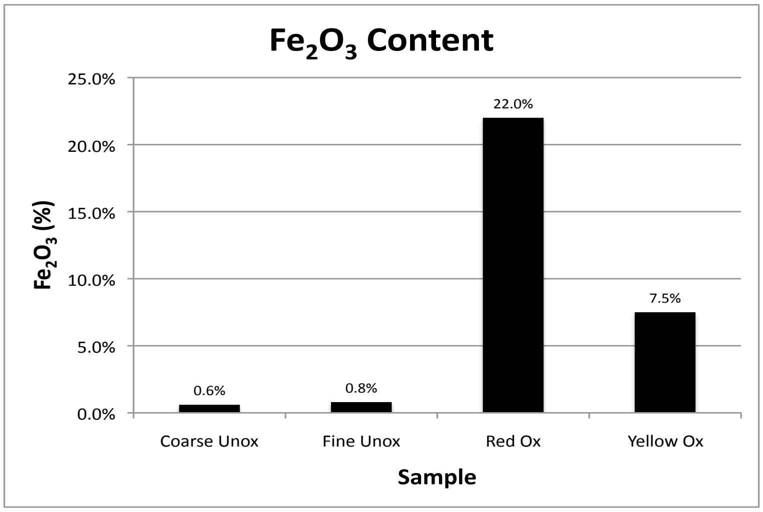

Figure 20: Fe_2O_3 content. Includes coarse and fine oxidized (4D and 4K, respectively); and red and yellow unoxidized samples (4L and 4M, respectively).

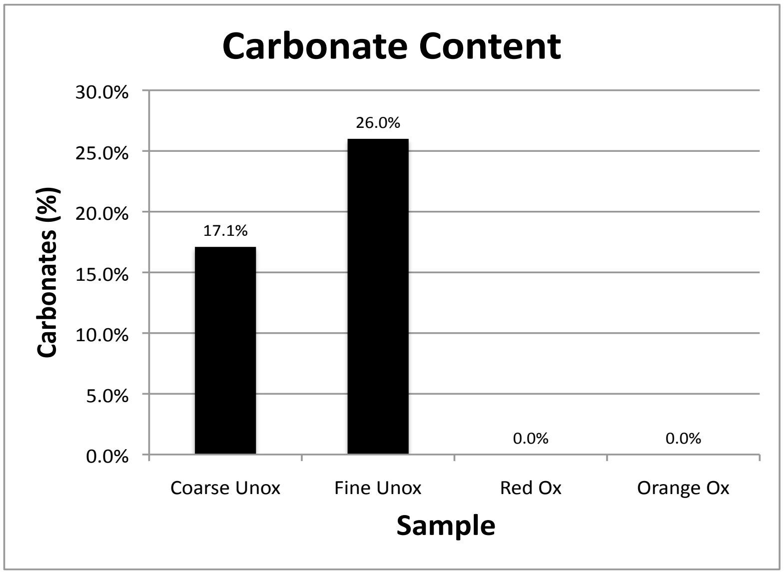

Figure 21: Carbonate quantification. Includes the coarse and fine unoxidized and red and orange oxidized samples.

Silicates in the bulk sample included minerals from the tectosilicate, inosilicate and phyllosilicate groups. The nesosilicate mineral ground was represented by garnet minerals, while tectosilicate group was represented by feldspars ($XAl_{(1-2)}$ $Si_{(3-2)}$ O_8, X=Ca, Na,or K) and quartz (SiO_2). Inoslicate ground minerals identified were wollastonite ($CaSi_3O_8$) and hornblende ($(Ca,Na)_{2–3}(Mg,Fe,Al)_5(Al,Si)_8O_{22}(OH,F)_2$). The phyllosilicate group was represented in the bulk sample by mica minerals [$X_2Y_{4–6}Z_8O_{20}(OH,F)_4$]. The 15.3 Å peak in the bulk sample suggests the presence of secondary phyllosilicate phases, as confirmed in the clay fraction XRD analysis.

Currently, the neutralization capacity of silicate minerals in an acid mine drainage settings is debated. Studies have determined that the weathering of silicate minerals containing Na, K, Mg, Ca and Mn provides some acid neutralization potential because these cations are relatively not easily hydrolyzed and thus would consume protons upon mineral dissolution (Weber et al., 2005; Jonckbloedt, 1997; Fernandez-Caliani et al., 2008). However, because of the slow reaction rate of rock-forming silicate minerals (Jambor et al., 2000; Jurjove et al., 2002; Garcia et al., 2004; Jonckbloedt, 1997) the potentially acid-neutralizing silicates present in the sample may offer only limited neutralization potential.

Sand Fraction Mineralogy

Minerals found in the sand fraction will take the longest to weather compared to their silt and clay-sized counterparts due to smaller specific surface area. Sand-sized particles had a very modest presence in 4K, with the sample being mostly comprised of silt and clay-sized particles. Pyrite was contained in the sand-size fraction; however, the presence was modest as suggested by the small XRD peaks. The presence of pyrite as sand-sized particles may prolong the acid-production risk even after more reactive clay and silt-sized pyrite particles have reacted. However, this risk is lessened by the very small concentration of sand-sized particles. Other sulfide phases were not identified in the sand-size fraction.

Similar to the coarse unoxidized sample, carbonates remained in the sample despite extensive carbonate destruction, specifically in the form of dolomite, which is more resistant to the carbonate destruction process. Sand-size carbonate particles will be at risk of being deactivated from active pH-buffering capabilities by coating with Fe-oxides in a sulfide oxidation environment due to a lower reactive surface area. Silicates identified in the sand fraction include wollastonite, quartz and feldspars (Figure 18).

Silt Fraction Mineralogy

Silt fraction mineralogy was close to that of the bulk sample. Minerals identified by XRD are feldspars, wollastonite, carbonates and sulfides (Figure 18). Of the sulfide minerals, pyrite, arsenopyrite, chalcopyrite and sphalerite were identified by XRD. XRD also confirmed the presence of acid-neutralizing dolomite in the silt fraction. The dolomite persisted despite the carbonate-destruction procedure, which may be due to the high crystallinity of the phase as indicated by sharp XRD peaks. Primary silicate minerals in the silt fraction confirmed by XRD include wollastonite, hornblende, garnet, feldspars, mica, talc and quartz. The 15.3 Å peak suggests the presence of secondary phyllosilicate minerals such as smectite in the silt fraction.

Sulfide phases pyrite, arsenopyrite and sphalerite were confirmed with scanning electron microscopy (SEM) with energy dispersive spectra (EDS). Figure 22 is a backscattered image, in which the particles that contain heavy elements (i.e. Fe) appear brighter than the other particles due to the higher incidence of electron backscattering to the detector that is typical of heavy elements such as Fe, Zn, Cu and Pb. The image is a representative of many backscattered images taken of the sample that show a relative abundance of sulfide particles in the sample.

Figure 23 shows arsenopyrite ($FeAsS$) and sphalerite ((Zn,FeS_2)) with the characteristic EDS spectra for each mineral. Pyrite was found to be abundant in the sample, with

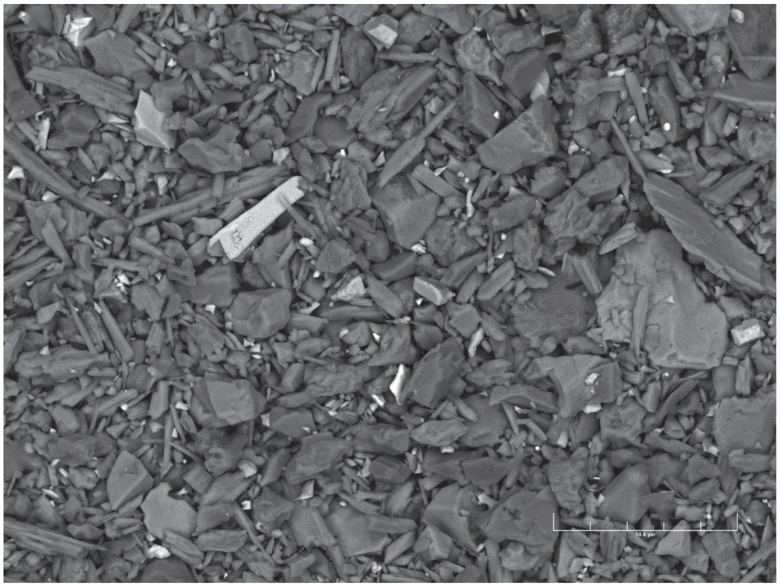

Figure 22: Backscattered SEM image. The brighter particles contain heavier elements such as Fe, Zn, Cu and Pb, among other metals. This image shows a relative abundance of sulfide minerals, which tend to be associated with heavy metals in the sample.

Figure 24 showing the characteristic EDS spectra with the typical 1 to 2 Fe to S molar ratio. The sulfide particles appear fractured, likely owing to the crushing and grinding process during the processing of the ore. Ca and Si peaks were also associated with some pyrite particles (Figure 22), which may indicate that there are silicate/sulfide aggregates in the sample or an interfering signal from directly adjacent particles.

Silicates were also found during SEM analysis. Wollastonite (Figure 24) was identified by its typical elongate morphology and characteristic Si and Ca EDS signals. Feldspar was also found, but with fractured morphology rather than its distinct rectangular morphology. Its characteristic Al, Si and Ca chemical signatures were recorded using EDS spectra.

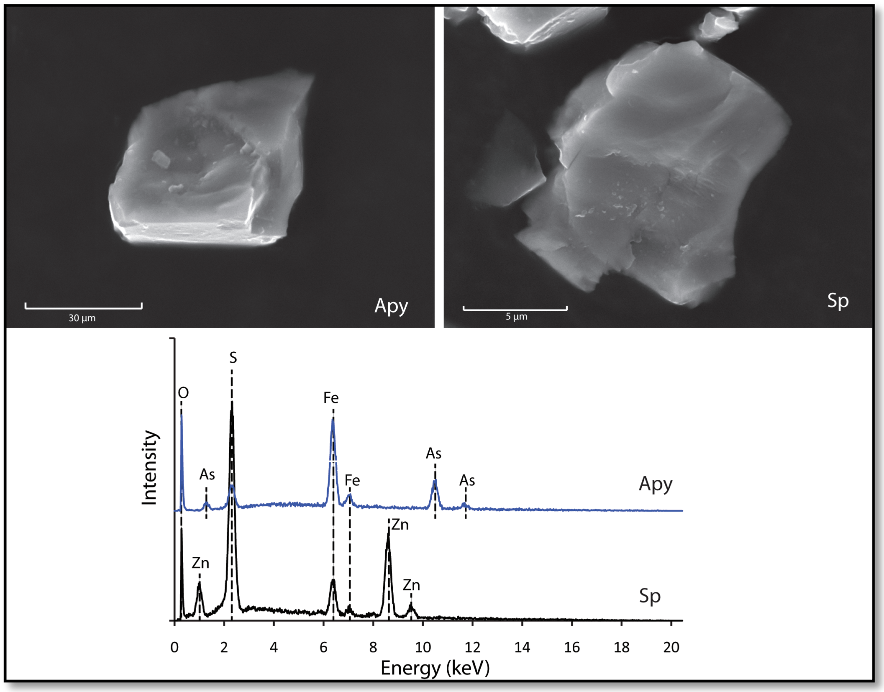

Figure 23: SEM Images and EDS spectra. Includes arsenopyrite (left) and sphalerite (right) particles, confirming their presence in the sample.

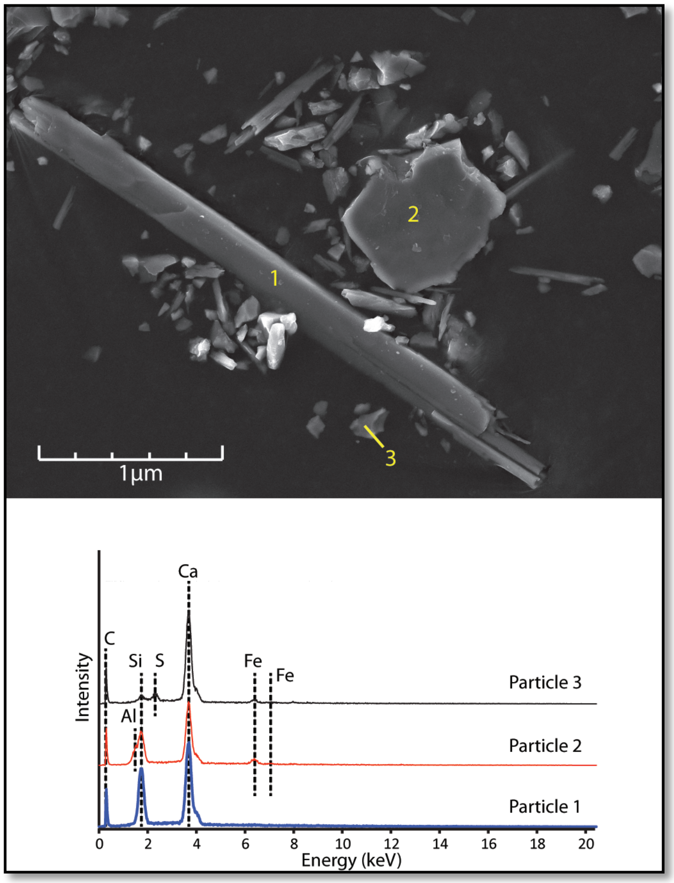

Figure 24: SEM Image and EDS spectra. Includes wollastonite (particle 1), Ca-feldspar (particle 2) and pyrite (particle 3)

Transmission electron microscope (TEM) analysis confirmed the presence of vermiculite and wollastonite (Figure 26). Vermiculite exhibited a slightly platy morphology with a characteristic chemical composition in EDS and characteristic d-spacing in the diffraction patterns (Figure 27). Wollastonite was also confirmed by EDS and SAED diffraction patterns (Figures 26 and 27, respectively), but the morphology was concealed by HFO phases atop the mineral crystal. HFO minerals that have precipitated on top of Clay Fraction Mineralogy

Oriented slides of the clay fraction analyzed with X-Ray diffraction (Figure 25) indicated that both primary and secondary phyllosilicate phases are present in the sample. Primary minerals include mica, chlorite and talc. Secondary phyllosilicate minerals in the clay fraction confirmed by XRD include kaolinite and smectite. Other phases identified by XRD analysis in the clay fraction include pyrite, feldspars, wollastonite and quartz.

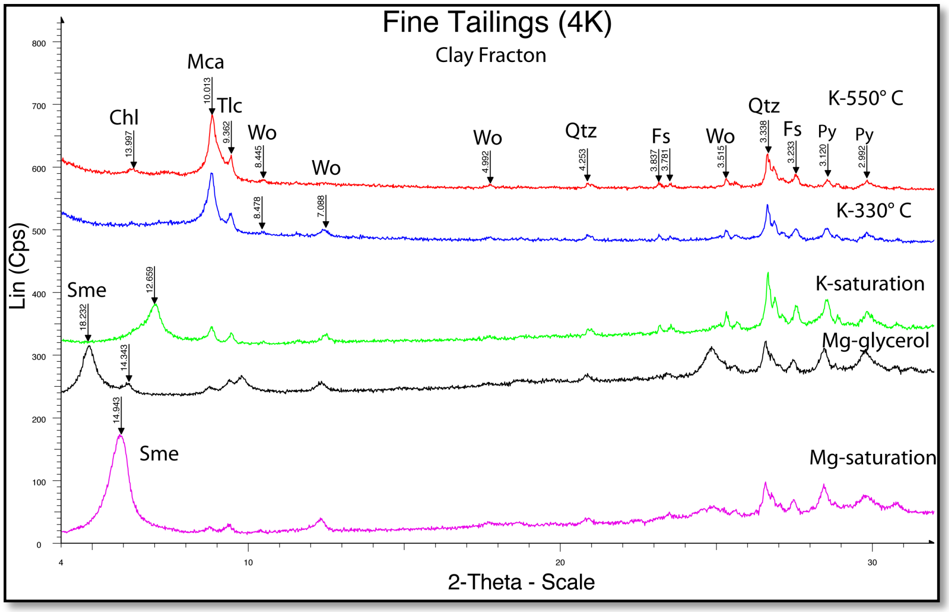

Figure 25: XRD diffraction of the clay fraction of the sample. Mineral key: Sme=smectite, Chl=chlorite, Mca=mica, Tlc=talc, Wo=wollastonite, Qtz=quartz, Fs=feldspar

the vermiculite and wollastonite crystals have a composition of Fe and trace Pb and Zn (Figure 26). It is possible that HFO forming on top of the more crystalline materials were poorly crystalline phases forming on top of more crystalline phases. This was

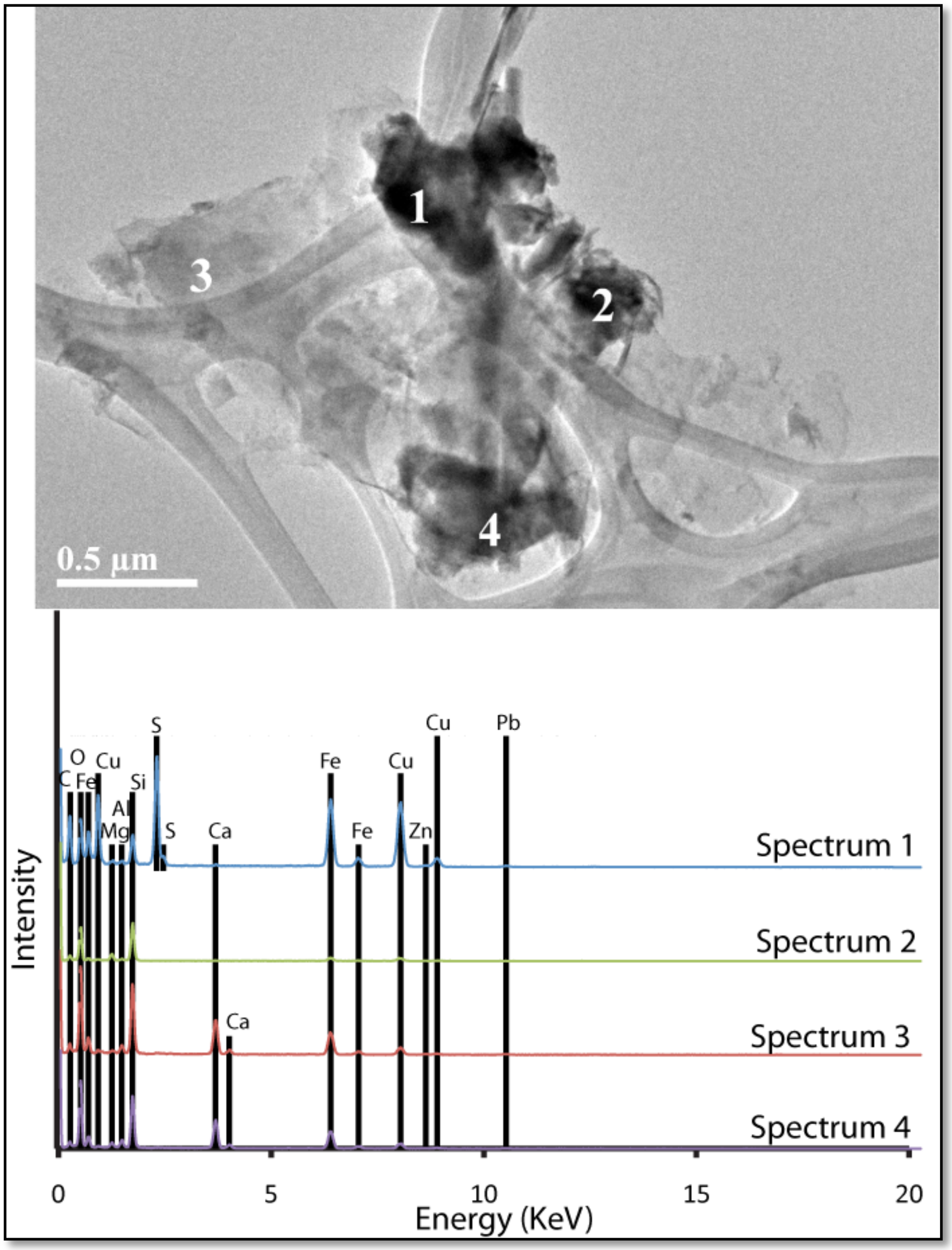

Figure 26: TEM Image with EDS Spectra. Includes a vermiculite particle (Spectrum 3) with characteristic chemical composition adjacent to a wollastonite particle (Spectrums 1, 2, 4) with characteristic chemical composition and diffraction patterns (Figure 12).

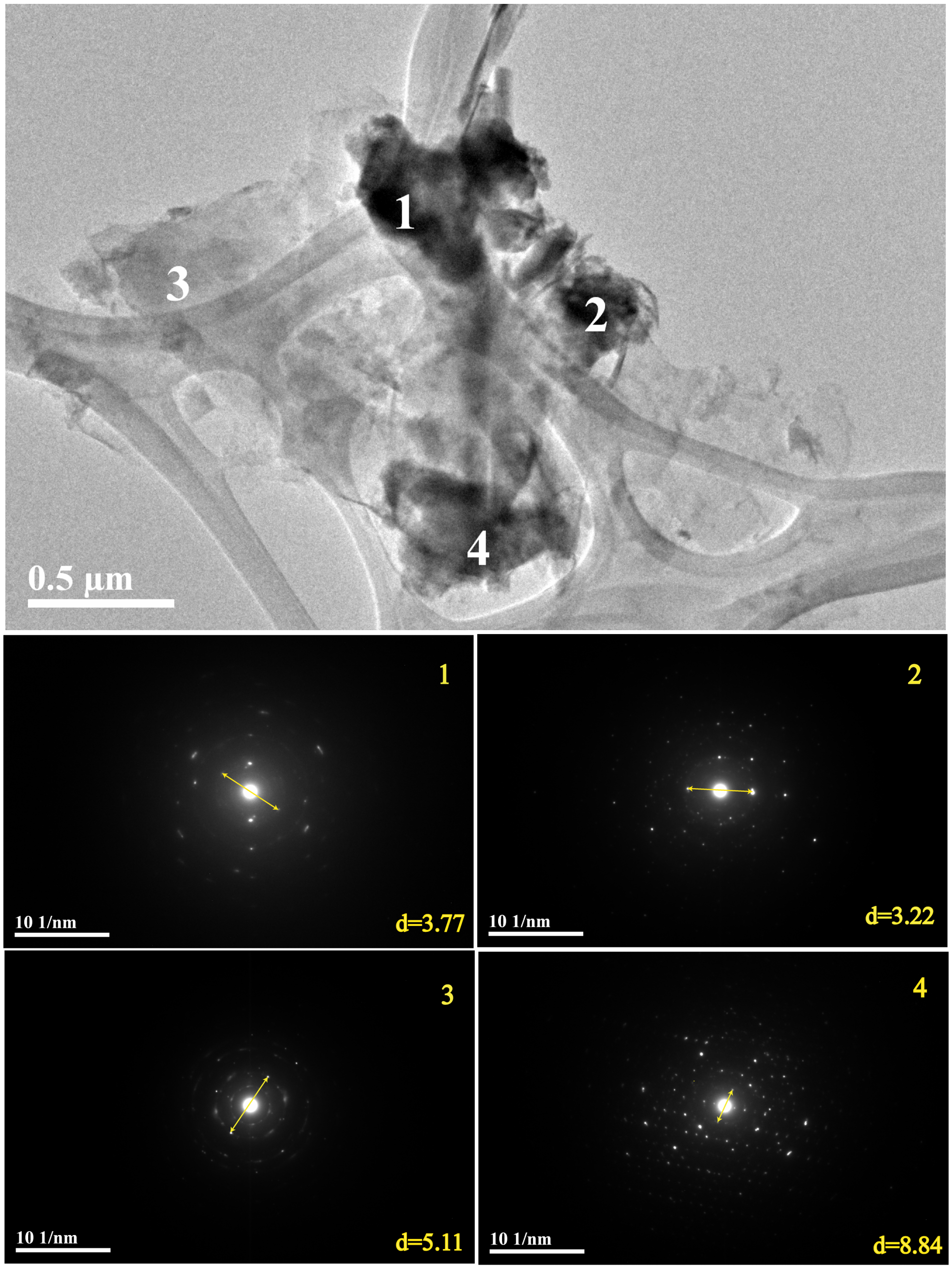

Figure 27: TEM Image with diffraction patterns. Includes characteristic d-spacing of vermiculite (3) and wollastonite (1, 2, 4). The combination of the characteristic d-spacings and Fe-composition along with other heavy metals (Figure 11) suggests Fe-oxides precipitating atop the vermiculite and wollastonite particles.

indicated by a symmetric pattern suggesting more crystalline phases integrated with a circular pattern that characterizes poorly crystalline materials. The formation of these minerals suggests that some oxidation of the sample had occurred by the time of sampling.

Oxidized (4L and 4M) Mineralogy

Weathered, or oxidized, tailings were identified in the field by color. A yellow to red coloration characterized oxidized materials. Several areas of the tailing impoundments showed signs of oxidation, but a highly oxidized location, indicated by abundant yellow to red materials, was chosen for sampling. Samples 4M and 4L originated from this area of the tailings impoundment. The samples were collected from a ditch approximately four foot deep that appeared to be in an area prone to experiencing wet/dry cycles. The ditch walls and bed were characterized by significant hardpan formation, i.e, the material was very strongly cemented. The upper two feet of the ditch was a moderately cemented silty sand and yellowish-red in color. The lower two feet of the ditch was a very strongly cemented silty sand and red in color. Sample 4M was collected from the upper two feet of the ditch, while 4L was collected from two to four foot depth below ground surface from the top of the ditch (Figure 28). Also, it is possible the composition of the oxidized samples prior to oxidation was similar to the unoxidizd samples because they came from the same mining deposits. It is also possible that leached components (e.g. dissolved Fe or dissolved Zn) have influenced the current composition of the oxidized tailings. Both oxidized samples had similar mineralogy, so they are evaluated together and the minor differences discussed in the sections below.

Bulk Fraction Mineralogy

The bulk sample, representing the sample composition as it was collected in the field, was analyzed by X-Ray diffraction (Figure 28). The analysis indicated the presence of various types of silicate, sulfate and hydrous ferric oxide (HFO) minerals. Minerals detected in the bulk sample were similar in both oxidized samples. Also, because all of the material in Tailing Heap 4 originated from the same mining deposits, it was assumed that the initial composition for the oxidized and unoxidized samples was similar.

Figure 28. Sample locations for sample 4M (yellow) and 4L (red).

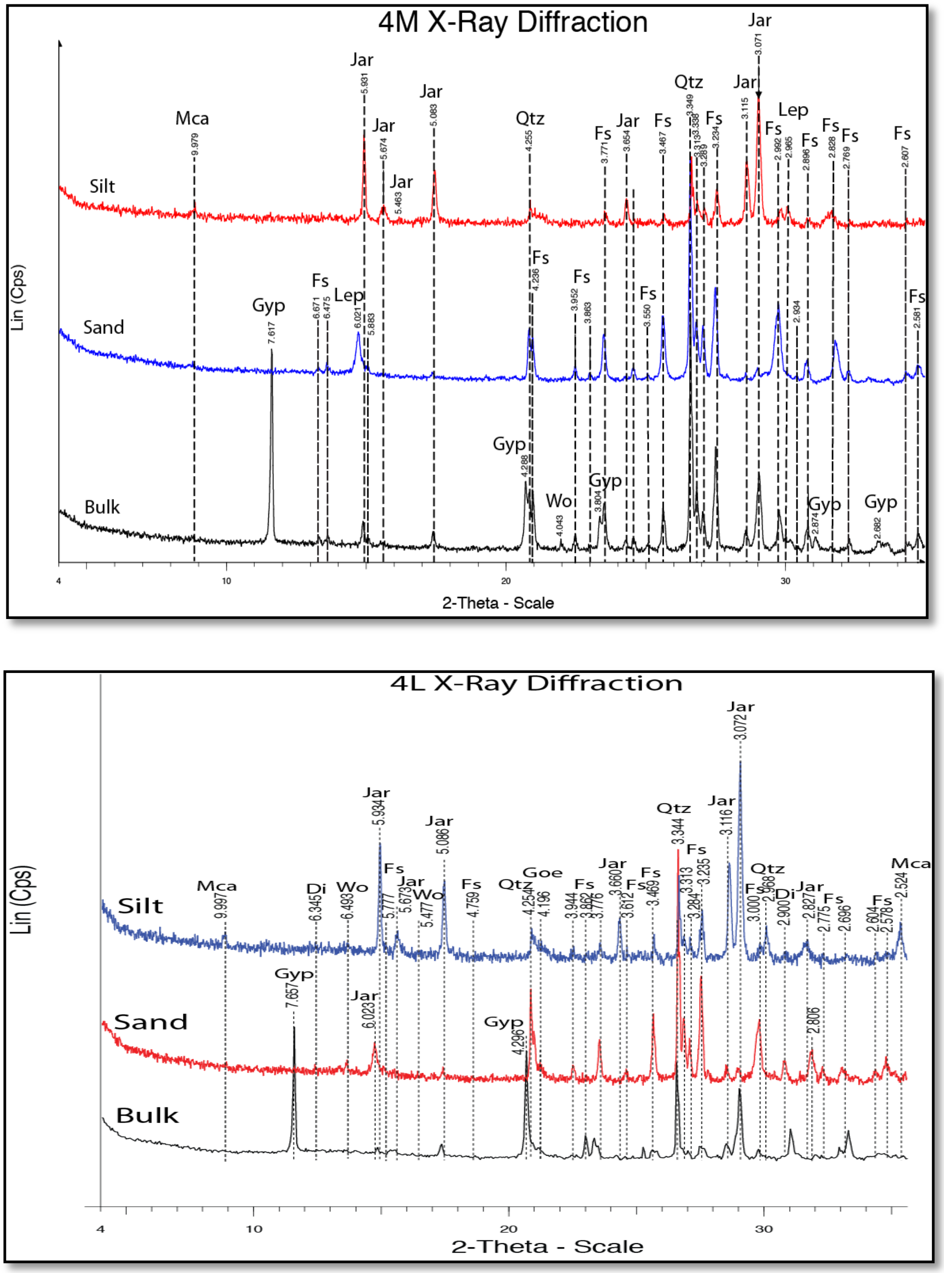

Figure 29. X-Ray Diffraction patterns. Includes the bulk, sand and silt fractions for samples 4M and 4L.
Di=diopside; Fs=feldspar; Goe=goethite; Gyp=gypsum; Jar=jarosite; Mca=mica; Qtz=quartz; Wo=wollastonite

Silicates present in the bulk sample include mica, feldspar, wollastonite, diopside and quartz. Mica's presence is indicated by the 9.979 A peak (Figure 29). The diminutive size of the peak suggests the mineral has relatively less abundance compared to other mineral species that were identified. Feldspars, common silicate minerals to el Monte deposits, were present in the sample. Characteristic peaks at 6.475 and 3.779 A, among others, indicate the presence of feldspars. Quartz was also detected with characteristic, strong peaks at 4.236 and 3.348 Angstrom. Wollastonite was not as abundant in the oxidized tailings as the unoxidized tailings, with small peaks at 4.043 and 6.493 Angstrom. Diopside, commonly associated with wollastonite, showed a small presence with diminutive peaks at 6.345 and 2.900. Of the common rock-forming minerals, mica, feldspar and quartz are the most resistant to weathering during low-pH conditions (Garcia et al., 2004; Thompson & Urainczyk, 2002). These minerals were also found to persist at other sites with similar characteristics (Courtin-Nomade and Grosbois, 2009; Romero, 2006). Silicates that were notably absent were chlorite, smectite and vermiculite. These minerals are discussed further in the weathered clay mineralogy section of this report.

Currently, the neutralization capacity of silicate minerals in an acid mine drainage settings is debated. Studies have determined that the weathering of silicate minerals containing Na, K, Mg, Ca and Mn provides some acid neutralization potential because these cations are not easily hydrolyzed (Weber et al., 2005; Jonckbloedt, 1997; Fernandez-Caliani et al., 2008). However, silicates with Fe and Al in the structure do not neutralize acidity because of the ease of which these cations are hydrolyzed, which is an acid-producing reaction (Weber et al., 2005; Jonckbloedt, 1997; Fernandez-Caliani et al., 2008). The prominence of silicates containing Na, K and Ca (e.g. feldspars, wollastonite and micas) and trace amounts of silicates containing Mg (diopside) in the already heavily oxidized samples suggests that some neutralization potential may remain. However, because of the slow reaction rate of rock-forming silicate minerals (Jambor et al., 2000; Jurjove et al., 2002; Garcia et al., 2004; Jonckbloedt, 1997) the potentially acid-neutralizing silicates present in the oxidized tailings may offer only limited neutralization potential. Also, the low pH measured in the field (See Chapter II) indicates that the pH is not controlled by the potentially neutralizing silicate minerals in the sample.

Sulfate minerals were abundant in the bulk sample, as indicated by sharp and strong characteristic diffraction peaks. Gypsum ($CaSO_4$ x $2H_2O$) was present, as shown by the very sharp and high 7.617 A peak (Figure 29). The abundance of this mineral is likely due to the extensive weathering of sulfide minerals, such as pyrite, in the oxidized tailings. Jarosite was also abundant and had a high degree of crystallinity in the sample, as indicated by the strong and sharp 5.948, 5.097 and 3.120 A peaks, among others.

Hydrous ferric oxide (HFO) minerals were also present in the bulk sample. Minerals of this type that are common to oxidized mine waste sites include goethite, lepidocrocite, schwertmannite, hematite and ferrihydrite. Particularly in hardpan cements, these minerals tend to be closely interrelated, especially goethite and hematite (Courtin-Nomade, 2009, Bigham et al., 2002). Schwertmannite, a very common mineral in acid mine drainage settings and associated with Fe(oxy)hydroxide mineral mixtures (Bigham et al., 2002), was also likely present. The short-range order of the schwertmannite crystal structure, however, makes the mineral difficult to identify by XRD (Bigham and Nordstrom, 2000). Goethite was indicated by the wide 4.196 peak in both samples, and hematite by the 2.696 peak in sample 4L. The presence of hematite in sample 4L likely causes the brilliant red color of the sample. The absence of hematite in sample 4M allows goethite to determine the yellowish-brown color of the sample (Bigham et al., 2002). Lepidicrocite shares many peaks with feldspar minerals, however the mineral was confirmed in the clay fraction of sample 4L with characteristic peaks occurring at 6.248 and 2.450. Free iron concentrations as Fe_2O_3 were 22.0% and 7.5% for samples 4L and 4M, respectively. The greater prominence of free iron concentration suggests greater sorptive capacity of heavy metals for 4L compared to 4M.

Over time, Fe(oxy)hydroxide minerals tend to undergo changes in crystallinity. In dry climates, acid mine drainage can lead to a transition from poorly crystalline to very crystalline (Bigham et al., 2002, Courtin-Nomade, 2005). However, the sorptive capacity of these minerals tends to go down with higher crystallinity due to higher surface area (Courtin-Nomade and Grosbois, 2009).

Due to the weathering of aluminosilicate minerals, aluminum oxides may be expected. However, the minerals have a pKa of 5, therefore, they would only precipitate at pH above pH 5 (Bigham and Nordstrom, 2000). The oxidized tailings have a pH of 2.5 or below. Jarosite, which tends to occur at pH 4 or below (Fanning et al., 2002), consumes Al in low-pH condition. The aluminum can substitute for Fe in the mineral structure, and will form a solid solution of jarosite and alunite (Stoffregen et al., 2000).

Carbonates were not observed in the sample, confirmed by XRD and carbonate quantification analyses, despite a likely initial abundance similar to the unoxidized tailings. Neutralization potential by carbonates has been largely consumed by the acid mine drainage. An absence of carbonates was also observed in other oxidized tailings heaps in the area (Romero, 2006; Romero et al., 2007).

Sand Fraction Mineralogy

Visual observation of the samples indicated that sand-size particles composed the majority of the sample. The sand fraction was evaluated using X-Ray Diffraction (Figure 29).

Of the silicate minerals, feldspars, quartz, wollastonite, diopside and mica were present in the sand fraction. Feldspars, quartz and mica minerals are also among the most persistent of the silicates in low-pH conditions (Romero, 2006; Courtin-Nomade and

Grosbois, 2009). Sulfate minerals observed in the sand fraction included Jarosite. Jarosite was very crystalline and abundant in the sand fraction, based on peak strength and sharpness. Gypsum may have also been present, but gypsum dissolves during the size fractionation procedure due to high solubility. HFO minerals were also present in the sand fraction, although many of the peaks are shared, as in the bulk fraction. Some wider peaks, e.g. 1.694, 1.849 and 2.129 A, among others, suggest poor crystallinity of HFO minerals. Based on the location of the peaks, these likely include schwertmannite, goethite, lepidocrocite and hematite. These minerals, especially goethite and hematite, are abundant. The minerals tend to be intimately related with one another (Bigham et al., 2002; Courtin-Nomade, 2009). Also, Fe(oxy)hydroxide minerals have a tendency to form on the surface of silicate minerals during silicate weathering (Bigham et al., 2002).

Silt Fraction Mineralogy

X-Ray diffraction revealed that the silt fraction had similar minerals as the sand fractions (Figure 29). Although silicates such as quartz, mica and feldspars were present, the silt fraction was dominated by jarosite and poorly-crystalline HFO minerals, based on peak intensity for these minerals.

The silt fraction was also analyzed by scanning electron microscopy (SEM). Analysis indicated that there is aggregated material present containing Fe-rich material associated with many elements that compose the common rock forming minerals as well as

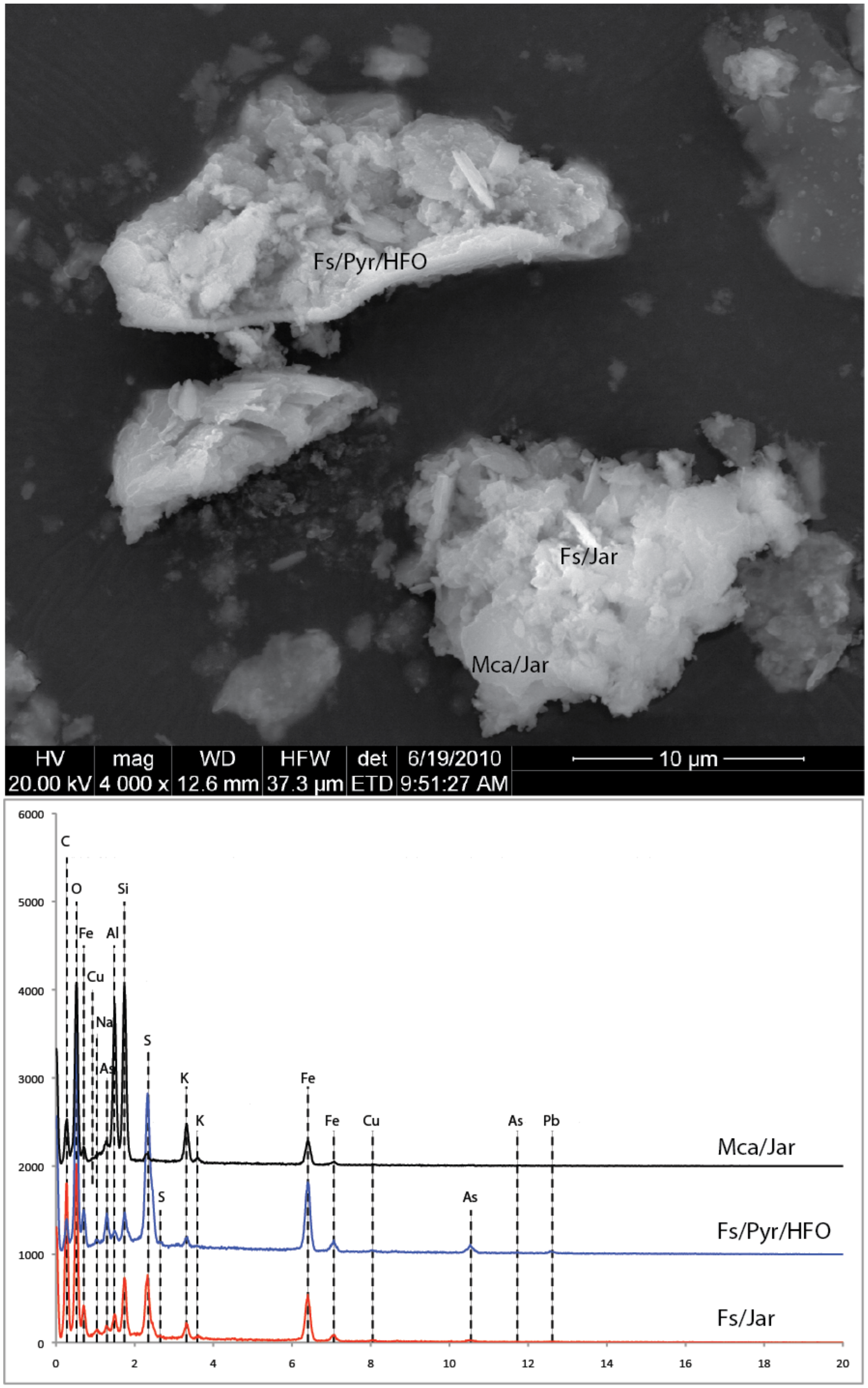

Figure 30. Scanning electron image with characteristic electron dispersive spectra.

potentially toxic heavy metals. Potentially toxic elements tend to originate from sulfide minerals and are retained in HFO minerals upon dissolution of the primary sulfide minerals. Figure 30 shows a SEM image and several particles rich in Fe, Na, Al, K, Si and trace amounts of As, Cu and Pb. The image also shows multiple particles with rounded (i.e. weathered) edges and what appears to be amorphous material. Representative spectra were taken of the particles. The area composed of mica and jarsoite (Figure 30), exhibits platy morphology similar to mica. The EDS signature shows a composition of Fe, Al, Si and S as major components, and Cu, As and Pb as minor components of the particle. The peak strength of Al, K and Si are at an approximately 1 to 1 to 3 molar ratio, similar to feldspar ($KAlSi_3O_8$). The peak strength ratio of Fe and S is similar to the proportions in jarosite ($KFe_3(OH)_6(SO_4)_2$, although slightly depleted in Fe. This may be due to intergrowth of HFO minerals with the jarosite or the substitution of Al for Fe in the jarosite structure. The minor elements associated with the particle are likely adsorbed on the jarosite and/or HFO surface or co-precipitated with these minerals (Romero, 2006).

On the lower part of the same particle (Figure 30) lies a fragment with platy morphology. The EDS spectra shows the major elemental components of the area to be Na, As, Al, Si, K, S and Fe. Minor elemental components include As, Cu and Pb. The presence of the minor elemental components may be partly due to the presence of unweathered sulfide minerals or associated with HFO minerals. The molar ratio of Al, K and Si is congruent with mica $(KAl_2(Si_3Al)O_{10}(OH)_2$, while the relatively small amount of S present, together with Fe and K, suggest the presence of jarosite.

Pyrite was also observed using SEM technology. A representative EDS spectra shows the mineral to be associated with feldspar and HFO (Figure 30). HFO is often associated with weathering sulfide minerals. Encasements composed of Fe(oxy)hydroxide minerals can prevent sulfide minerals from fully oxidizing in acid mine drainage settings (Courtin-Nomade and Grosbois, 2009; Jambor, 1994). Sulfides were also found to persist in the Zimapan-area study of oxidized tailings by Romero (2006) and in other studies of sulfide-containing oxidized mine waste (Courtin-Nomade, 2009).

Figure 31 shows another group of particles in the weathered tailings and characteristic EDS spectra. These particles consist largely of feldspar, jarosite and HFO; the particles are all associated with trace amounts of As. A persistent chalcopyrite ($CuFeS_2$) particle was also encountered, also associated with trace As. A backscattered electron image (Figure 32) confirms the continuity of the chalcopyrite particle and the heavy elements, likely sorbed and/or copreciptated with HFO and jarosite, associated with the feldspar particles in the upper portion of the image. The presence of As suggests there may be a coating of HFOs on the surface, with As sorbed on the surface and/or precipitated.

Ca and Mg are notably absent from all spectra, which confirms XRD observations that calcite and primary minerals such as amphiboles, pyroxenes and pyroxenoids such as

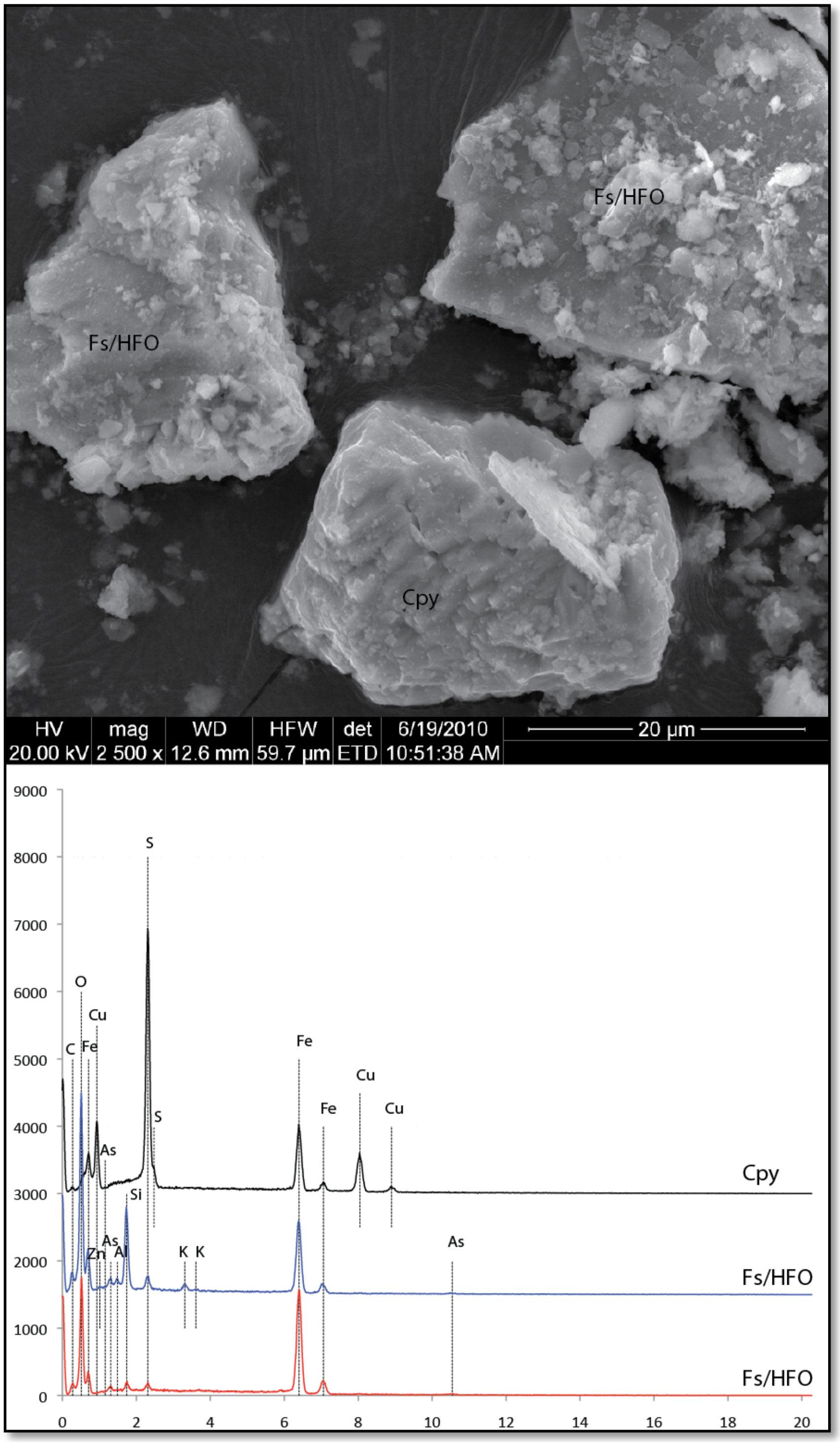

Figure 31. Scanning electron microscope image with representative EDS spectra.

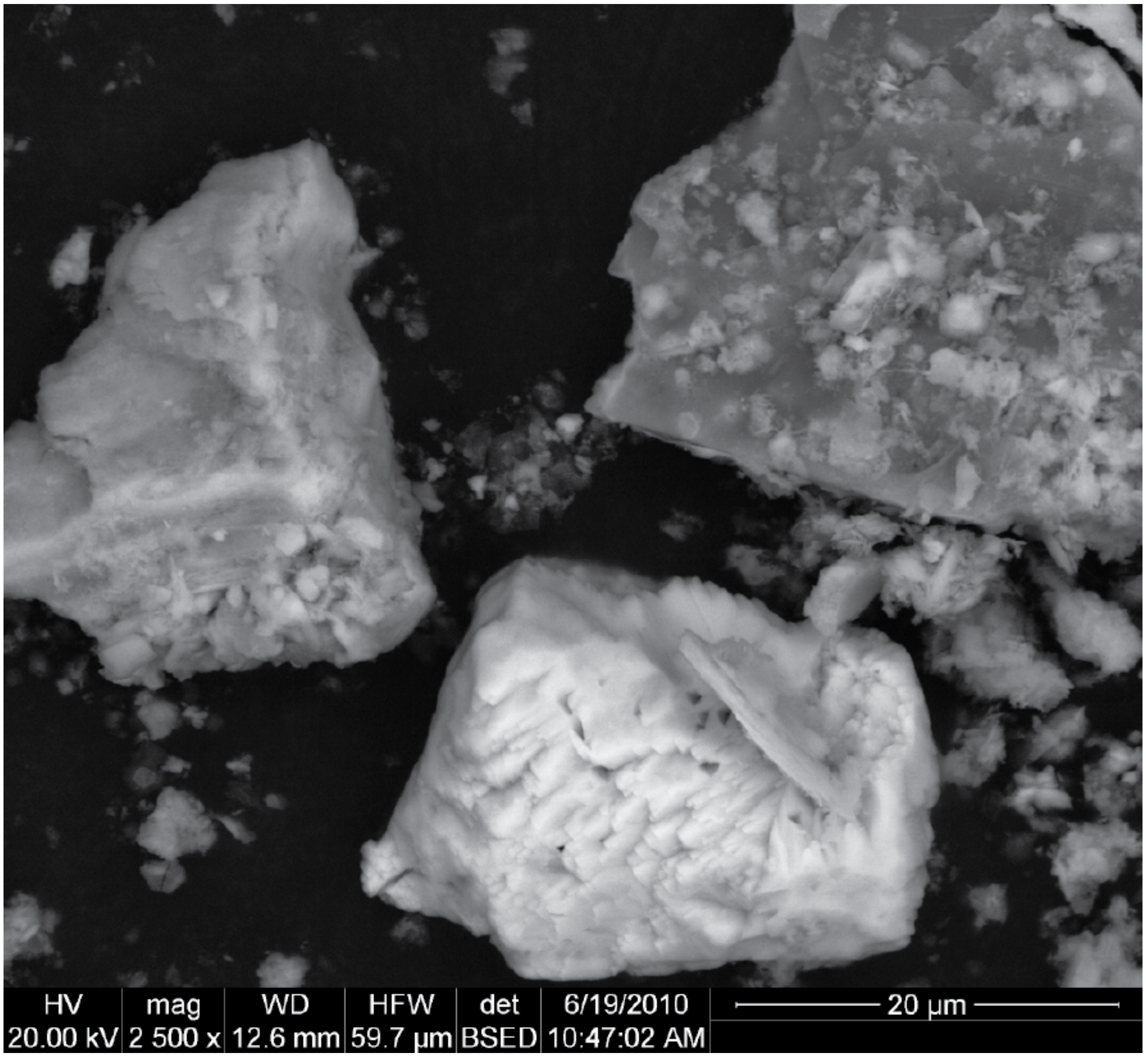

Figure 32. Backscattered scanning electron microscope image. The brighter portions of the image represent heavier elements such as Fe, Cu, As, and Zn.

wollastonite are either not present or are greatly depleted in the sample. This suggests that these minerals have partly dissolved from the tailings and that Ca and Mg have been leached from the system or transformed into more leachable, soluble minerals such as

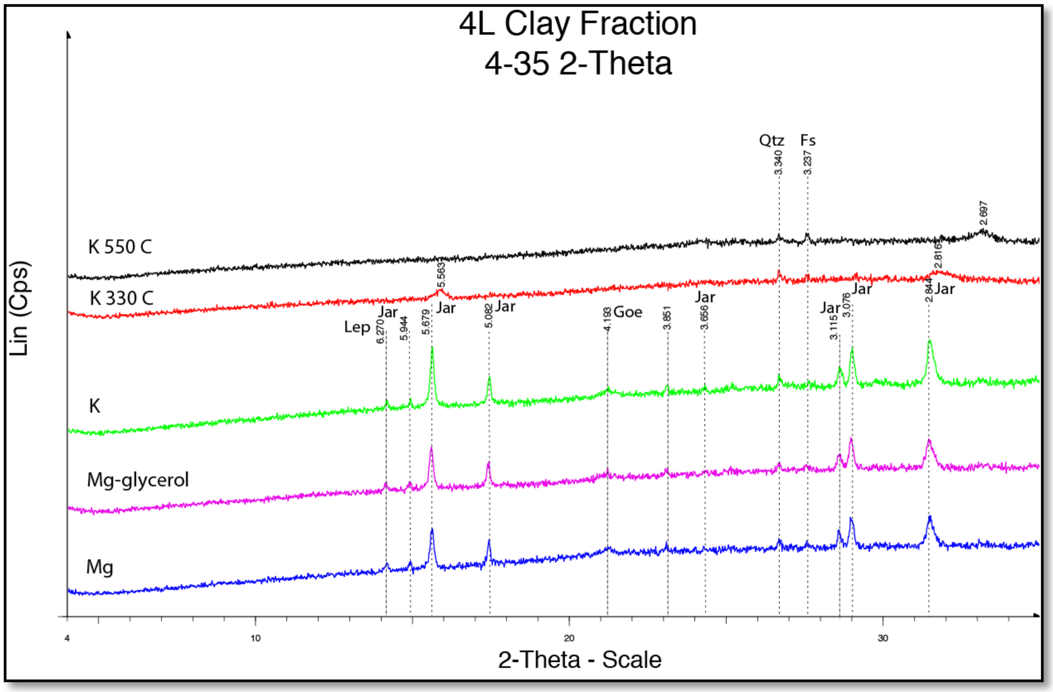

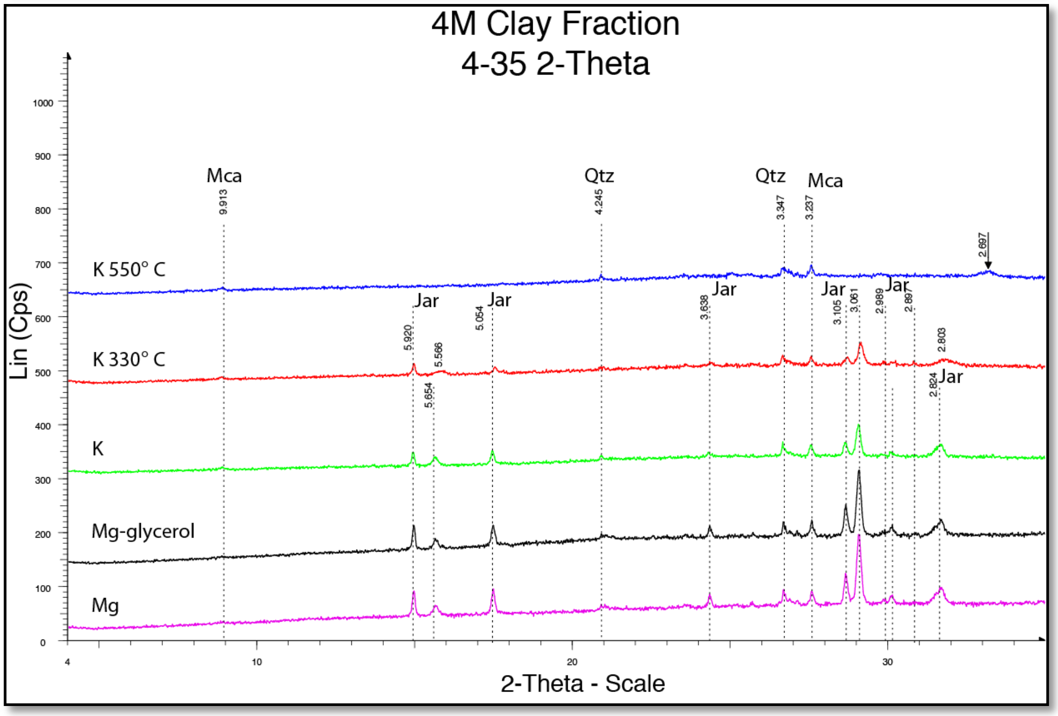

Figure 33. X-Ray Diffraction patterns for the clay fraction. Includes 4L and 4M showing Mg-saturation, Mg-saturation with glycerol solvation, K-saturation, K-saturation heated at 330 C, K-saturation heated at 550 C.
Abbreviations: Fs=feldspar; Jar=jarosite; Lep=lepidocrocite; Mca=mica; Qtz=quartz

gypsum and starkeyite. This is consistent with a study done by Romero (2006) on oxidized and unoxidized mine waste in the Zimapan area, in which such minerals were absent and a depletion of Ca and Mg observed in oxidized tailings.

Clay Fraction Mineralogy

Clay XRD analysis revealed the presence of several minerals common to the other fractions, including mica, quartz, jarosite and poorly crstalline Fe(oxy)hydroxides (Figure 33). The magnesium and potassium saturations showed that there were no intermediate weathering products of primary silicates such as vermiculite, kaolinite or smectite. This suggests that these minerals have already been dissolved by the low-pH AMD solution (Karathanasis, 2002). Lepidocrocite was also confirmed to be present in 4L, as indicated by peaks located at 6.248, 3.341 and 2.450 Angstrom.

Clay fraction minerals were also evaluated using transmission electron microscopy (TEM). Figure 34 presents a conglomeration of particles exhibiting colloform morphology, suggesting precipitation from colloidal suspension (Ramdohr, 1969). The selected area electron diffraction analysis reveals that the particle is poorly crystalline, with few visible points. A characteristic EDS spectra (Figure 34) indicates the major component of the particle to be Fe. Al, Si and As also were significant components. Thus, the particle is likely a poorly crystalline conglomerate of HFO and amorphous silica. Poorly crystalline HFO minerals have been found to sorb significant amounts of

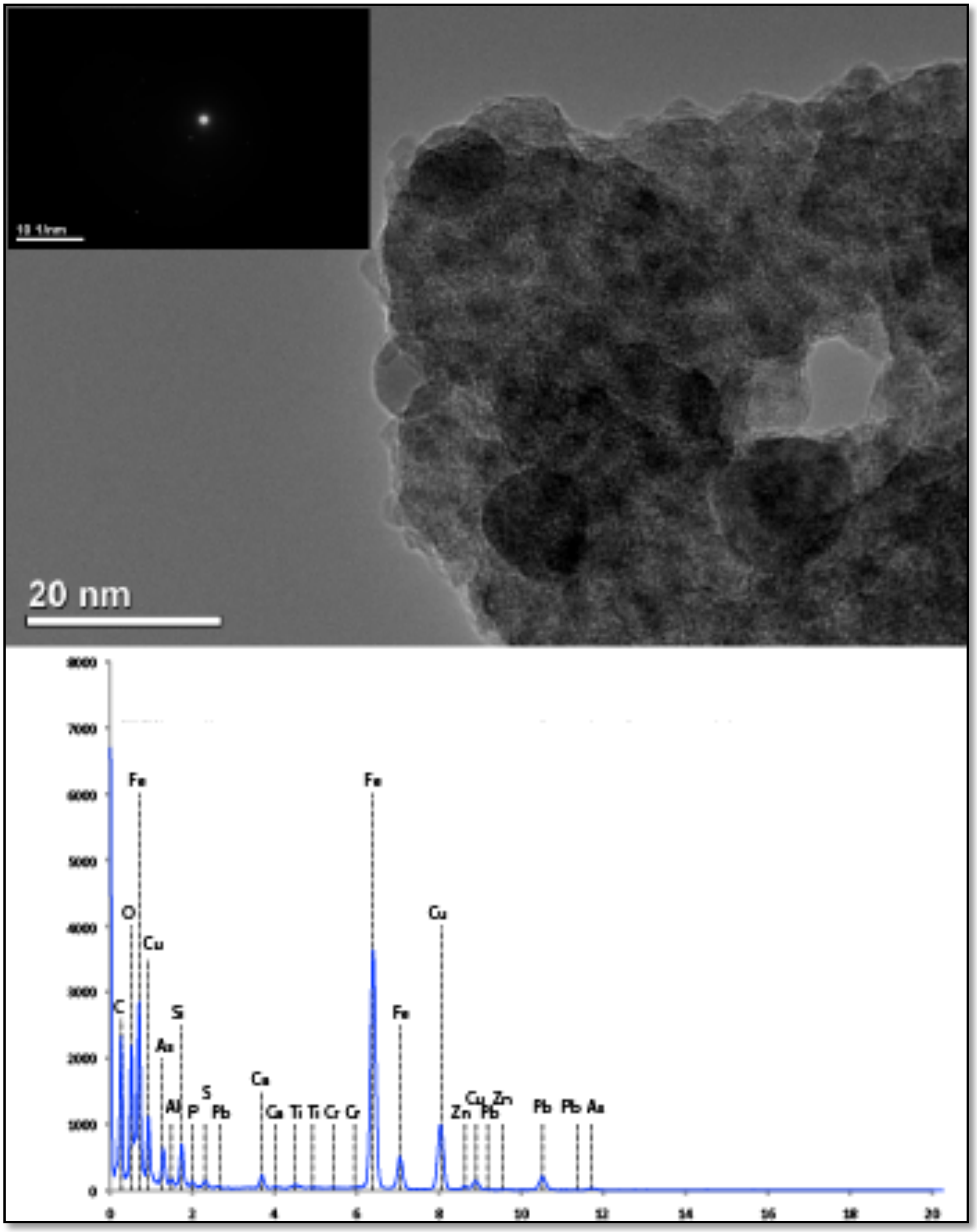

Figure 34. Transmission Electron Microscope image with a representative EDS spectrum and SAED pattern (inset).

As (Courtin-Nomade and Grosbois, 2009), thus the As is likely associated with the HFOs. Minor elements included Ti, Sb and Zn. Sb and Zn tend to be at least partly retained by sorption onto HFO surfaces (Flakova et al., 2012). Ti may due to the presence of highly resilient Ti-oxide phases such as rutile or anatase. Cu may have also beenpresent, however the Cu grid likely accounts for the strong signal indicated on the EDS spectra.

Sample Differences

Sample differences in terms of mineralogical composition were minor. The major differences were expressed in sample color. Sample 4M, a yellowish-brown, contained goethite as the chief HFO mineral. Goethite is characteristically a yellowish-brown color (Bigham et al., 2002), as expressed in the sample color. Sample 4L, a reddish-brown, contained a mixture of goethite and hematite. The presence of hematite lends a rich red color element to the sample (Bigham et al., 2002).

CHAPTER IV

GEOCHEMISTRY

Relative concentrations of various elements were evaluated to determine the relative stages of weathering and degree of metal attenuation. Elemental composition, free iron and total carbonates were evaluated for unoxidized samples (4D and 4K) and oxidized samples (4L and 4M). Because the weathered and unweathered tailings originated from parent material mined from el Monte deposits, the initial composition of the tailings from all tailing samples was assumed to be very similar. However, the input of leached phases into the oxidized tailings may have occurred.

Major Components

Major compositional elements (Si, Al, Fe, Ca, Mg, K, Na, Mn and Ti) were evaluated to determine relative degree of weathering to major minerals found in the el Monte mining deposits near Zimpan, Mexico. These minerals include quartz, mica, feldspars, wollastonite, hornblende, augite, calcite and dolomite (Garcia and Querol, 1991). The major compositional elements were also analyzed to estimate the retention of components released from the above minerals resulting from weathering. Concentrations of the major elements were compared to zirconium and titanium concentrations as a ratio. The patterns were identical when compared to the raw concentrations, so the raw concentrations were used in the analysis. All major components were analyzed as their respective oxides when applicable.

Aluminum, silicon, calcium, magnesium, manganese and titanium

Aluminum, silicon, calcium, magnesium, manganese and titanium were reported as their respective oxides, Al_2O_3, SiO_2, CaO, MgO (Figure 35), MnO_2 and TiO_2 (Figure 36). Concentrations in the oxidized samples are compared to the concentrations in the unoxidized samples. Silicon concentrations inidicated a relative depletion in the red oxidized, 4L, and enrichment in sample 4M. Aluminum, sodium and potassium remained in relatively equivalent concentrations in sample 4L compared to the unoxidized samples, but enrichment of these oxides was observed in sample 4M relative to the unoxidized samples.

Calcium and magnesium were relatively depleted in both oxidized samples. The depletion of silicon in 4L compared to 4M indicates that the weathering of silicates. The relative enrichment of aluminum, potassium and sodium (Figures 35 and 36) in sample 4M suggests that silicates such as micas and feldspars have been more heavily weathered in 4L over 4M. Calcium and magnesium depletion in the oxidized samples is likely due to the absence of carbonates such as dolomite and calcite, as confirmed in the total carbonate analysis. Total carbonate analysis indicated these minerals were not present in the oxidized samples and likely consumed by acidity. A similar depletion was encountered at other

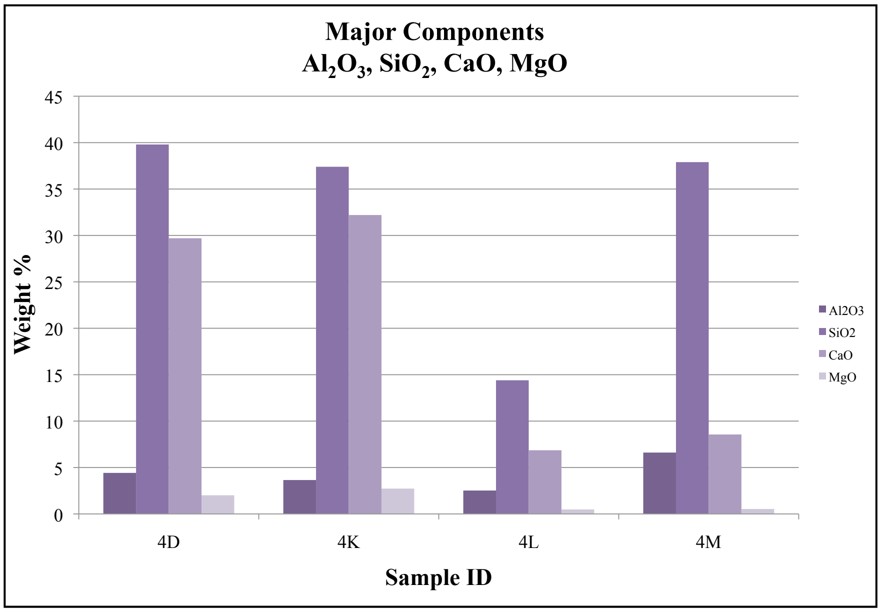

Figure 35. Total elemental composition, expressed as oxides, for Al, Si, Ca and Mg.

sites near Zimapan (Romero, 2006; Romero, 2007). Depletion of these components may also be partly accountable to the depletion of silicates partly composed of Ca and Mg such as wollastonite (Ca), hornblende (Ca, Mg) and augite (Ca, Mg). X-Ray diffraction analysis of the oxidized samples confirmed the relative depletion of these minerals (Mineralogy Chapter of this report). Manganese (MnO), originating from silicates such as wollastonite, hornblende and augite, was depleted in both oxidized samples.

Manganese may also originate from manganese oxides, but these mineral phases are difficult to identify using the methods to determine mineral composition in this study. The depletion of manganese was likely due to the element not being retained well following weathering of manganese-containing minerals. This is likely due to manganese being mobile in low-pH conditions (Lizarraga-Mendiola et al., 2009; Dixon & White, 2002).

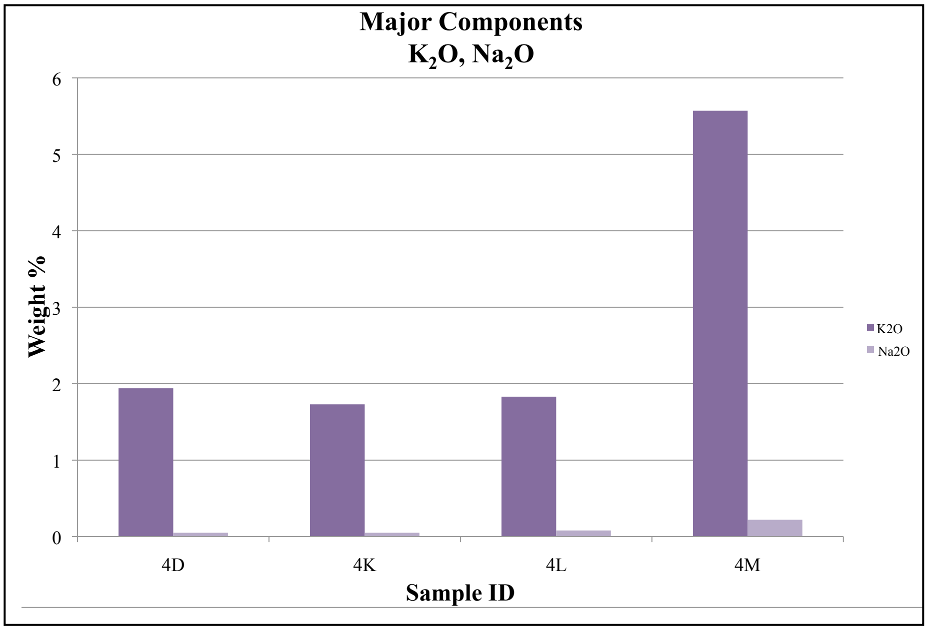

Figure 36. Total elemental composition, expressed as oxides, for Na and K.

Titanium (TiO_2) concentration in 4L was relatively equivalent to that of the unoxidized samples, while there was a slight enrichment in 4M. Titanium-containing minerals, including titanium oxides, are resistant to weathering even in low-pH conditions. Thus, titanium has persisted in the oxidized tailings despite an acidic environment (Figure 37). The relative enrichment of titanium in 4M is likely due to the earlier stage of weathering of the sample relative to 4L.

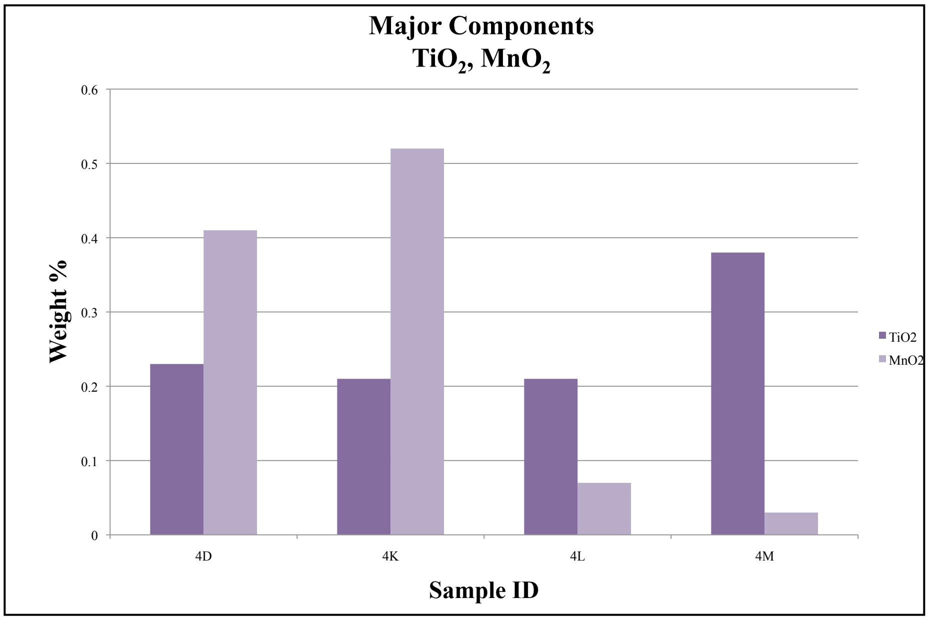

Figure 37. Total Elemental Composition, expressed as oxides, for Ti and Mn.

Iron

Iron (Fe_2O_3) concentrations remained relatively equivalent in 4M when compared to the concentrations in the unoxidized samples, while 4L showed enrichment (Figure 38). This trend concurs with the iron oxide quantification, in which 22% of 4L and 7.5% of 4M was found to contain free iron as Fe_2O_3. Iron originates in the unoxidized tailings as iron sulfides, iron-containing silicate minerals (e.g. biotite, hornblende, augite), and likely some primary iron oxides. As these minerals weather, the iron is retained in the form of poorly to well-crystalline hydrous ferrous oxides (HFO). As other components of the tailings weather, iron becomes more concentrated in the tailings. The relatively low concentration of iron in 4M versus 4L further supports less weathering of the sample compared to 4L.

Trace Components

Trace components (S, As, Cu, Ni, Pb and Zn) were evaluated on an elemental basis, rather than as oxides. Sulfur was enriched in both of the oxidized tailings compared to the unoxidized tailings (Figure 38). Comparing 4L to 4M, 4L contained more sulfur than 4M. Originating from sulfide minerals, sulfur is retained in acid mine drainage conditions in the form of gypsum and jarosite. Based on mineralogical analysis, both of these minerals were significant components of the oxidized samples. As silicate minerals are weathered and their components leached (e.g. Si, Al, K, Na, Ca, Mg), sulfur concentrations increase. The relative lack of sulfur in 4M versus 4L points to an earlier stage of weathering for 4M compared to 4L.

Arsenic concentrations were enriched in sample 4L, while 4M showed depletion (Figure 39). Oxidized tailings with enrichment of arsenic have been encountered at other sites near Zimpan (Romero, 2006; Romero et al., 2007). It has also been found in numerous studies that arsenic is attenuated in AMD conditions, as it adsorbs to iron-oxides even in low-pH conditions (Madera et al., 2003, Romero et al., 2007, Acero et al., 2006). The lower concentration of As in sample 4M can be attributed to the lower Fe and free iron as Fe_2O_3 present in the sample as compared to 4L. Zinc and nickel concentrations were depleted in the oxidized samples versus the unoxidized samples, and slightly more depleted in 4M versus 4L (Figures 39 and 40). Zinc occurs as sphalerite in the tailings, while nickel tends to be associated with pyrrhotite (Ribet et al., 1994; Garcia et al., 2004). Zinc and nickel are not very strongly sorbed on HFO minerals, particularly at low pH (Johnson, 1986) and both tend to be sensitive to loss during transformation of HFO minerals into more crystalline phases (Moncur et al., 2009; Ranville et al., 2003) and thus are not very well retained upon weathering of the primary minerals in which they occur.

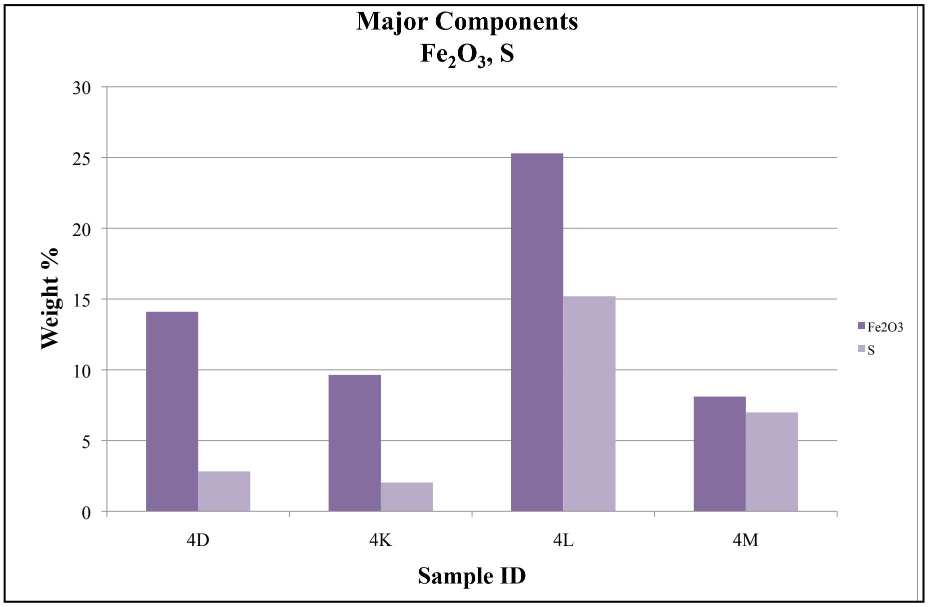

Figure 38. Total elemental composition for Fe, expressed as oxides, and S.

Copper remained at a similar concentration in both oxidized samples as the unoxidized samples, with a very slight depletion in 4M (Figure 39). Copper is very strongly sorbed to and attenuated by early-formed HFO minerals, but prefers Al-hydroxides, which form at higher pH. Cu also has a tendency to be retained during transformation of HFO to more crystalline phases, thus would be retained as the HFO minerals in the tailings "mature" (Moncur et al., 2009; Knodiar et al., 1999).

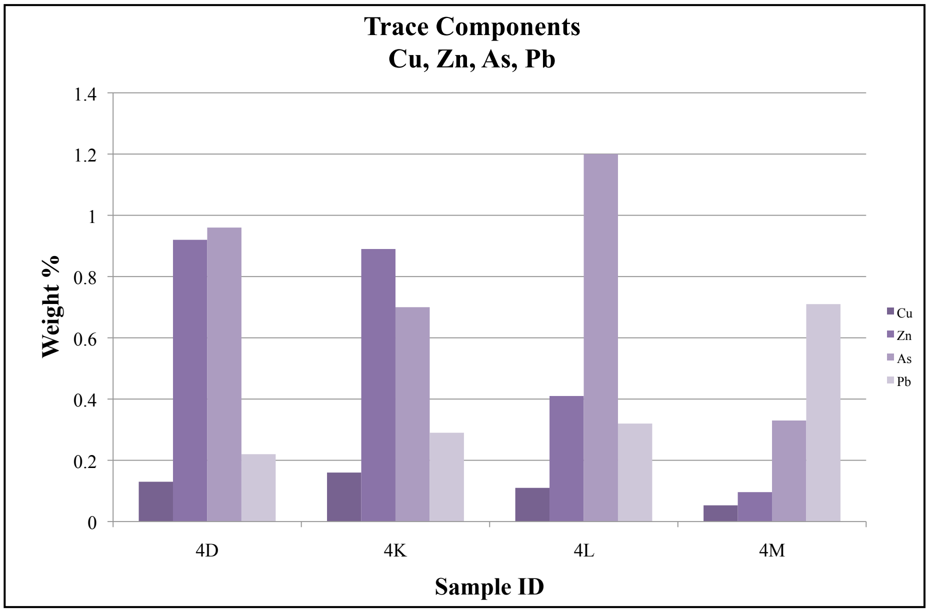

Figure 39. Total elemental composition for Cu, Zn, As and Pb.

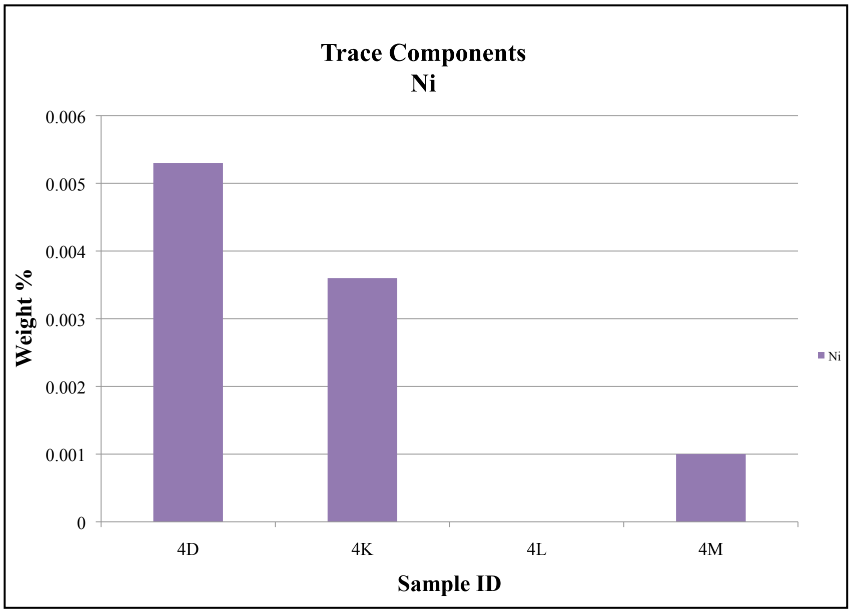

Figure 40. Total elemental composition for Ni.

Lead concentrations also remained at a similar concentration in sample 4L as the unoxidized samples (Figure 39). The element is sorbed to HFO minerals and can also be substituted for Al in jarosite. Lead also tends to remain sorbed into HFO minerals even as they “mature” and become more crystalline over time (Acero et al., 2006; Moncur et al., 2009).

CHAPTER V

SUMMARY, CONCLUSIONS AND FUTURE STUDIES

Acid-producing Minerals

The primary sulfide minerals identified in the oxidized and unoxidized samples include pyrite (FeS_2), Fe-containing sphalerite [(Zn,Fe)S], arsenopyrite (FeAsS) and chalcopyrite ($CuFeS_2$). Each of these sulfide minerals would produce acidity during oxidation, and therefore would contribute to the total acid production resulting from weathering of the unoxidized and oxidized tailings (Reactions 5 and 6). In addition to acid-producing potential, sphalerite, arsenopyrite and chalcopyrite will also release heavy metals as a result of oxidation of the minerals. The low pH of the oxidized tailings also increases the risk of metal release due to metals having greater solubility at low pH. In addition, at low pH the HFO minerals are more soluble, resulting in higher concentrations of dissolved Fe^{3+}. Fe^{3+} is known to accelerate the reaction rate of Fe-containing sulfide oxidiation (Singer and Stumm, 1970). The remaining pyrite (and other Fe-containing sulfides) in the oxidized tailings would therefore oxidize more rapidly than the Fe-containing sulfides present in the unoxidized tailings.

Acid-consuming Minerals

Minerals that are capable of neutralizing acidity were also identified in the unoxidized and oxidized samples. In the unoxidized samples, the acid-consuming minerals include carbonates (e.g., calcite and dolomite) and silicates (e.g., feldspars, mica and wollastonite). The oxidized samples also contained acid-neutralizing silicate minerals, specifically feldspars and mica minerals. Wollastonite was not identified in the oxidized tailings, suggesting it is either greatly depleted or absent. Total carbonates were determined to be approximately 17% in the course unoxidized, 22% in the fine unoxidized and 0% in the oxidized samples. Considering only carbonate neutralization of acidity, the coarse unoxidized tailings would have considerably greater neutralization copacity compared to the fine oxidized tailings. The oxidized tailings are devoid of carbonates, thus they have lost significant neutralization potential to the acid mine drainage solution. Carbonate minerals offer greater acid neutralization capabilities than acid-neutralizing silicate minerals potential due to greater reaction kinetics. Thus, the unoxidized samples have greater neutralization potential than the oxidized samples. This is also confirmed by the relatively high pH of the unoxidized tailings (7.8 – 8.2) compared to the oxidized tailings (2.2 to 2.4).

Trends in Metal Concentrations

High concentrations of heavy metals such as As, Pb, Zn and Cu were indicated in the unoxidized tailings. The oxidized tailings, which have undergone sulfide mineral oxidation and subsequent heavy metal release, have attenuated several heavy metals, especially As and Pb. These metals are particularly well-sorbed to HFO at low pH. As and Pb were also enriched in the oxidized samples. This observation suggests that some leaching from other source areas has occurred. To a lesser degree, Cu and Zn were also detected in the oxidized tailings, as indicated by EDS spectra of HFO minerals contained in the oxidized tailings. However, Cu and Zn were depleted in the oxidized tailings compared to the unoxidized tailings, as indicated by XRF analysis. This is likely due to the poor sorption of these metals to HFO minerals at low pH. Fe and S were enriched in the oxidized tailings, which may further indicate that other sources have contributed to the composition of the oxidized tailings.

Additional Research Needed

Vertical coring studies that investigate the changes in mineralogy and oxidation patterns with depth from the exposed surface of the oxidized tailings. In addition, horizontal coring studies designed to investigate the mineralogical changes and oxidation patterns laterally from the exposed wall of the oxidized tailings would help understanding of oxidation patterns horizontally from the oxidized tailings. Studies of these types can help to understand the localization and mechanism of oxidation in the tailings heaps.

REFERENCES

Acero, P., Ayora, C., and Carrera, J., 2007, Coupled thermal, hydraulic and geochemical evolution of pyritic tailings in unsaturated column experiments: Geochimica et Cosmochimica Acta, v. 71, p. 5325-5338.

Armienta, M.A., Rodriguez, R., Cruz, O., Ceniceros, N., and Aguayo, A., 1996, Arsenic pollution of the groundwater of Zimapan, Mexico, and its health impact, *in* Nath, B., Land, I., Meszaros, E., Robinson, J.P., and Hens, L., eds., International Conference on Environmental Pollution, Volume 1 and 2: Budapest, Hungary, p. 579-583.

Arroya, Y., and Seibe, C., 2008, Weathering of sulphide minerals and trace element speciation in tailings of various ages in the Guanajuato mining district, Mexico: Catena, v. 71, p. 497-506.

Bigham, J.M., Fitzpatrick, R.W., and Schulze, D.G., 2002, Iron oxides, *in* Dixon, J., Schulze, D., and Amonette, J., eds., Soil Mineralogy with Environmental Applications: Madison, WI, Soil Science Society of America, Inc.

Bigham, J.M., and Nordstron, D.K., 2000, Iron and aluminum hydroxysulfates from acid sulfate waters: Reviews in Mineralogy and Geochemistry, v. 40, p. 351-403.

Courtin-Nomade, A., Grosbois, C., Bril, J., and Roussel, C., 2005, Spatial variability in some iron-rich deposits generated by acid mine draining: Applied Geochemistry, v. 20, p. 383-396.

Courtin-Nomade, A., Grosbois, C., Marcus, M., Fakra, S., Beny, J., and Foster, A., 2009, The weathering of a sulfide orebody: speciation and fate of some potential contaminants: The Canadian Mineralogist, v. 47, p. 493-508.

Dixon, J.B., and White, G.N., 2002, Manganese oxides, *in* Dixon, J., Schulze, D., and Amonette, J., eds, Soil Mineralogy with Environmental Applications: Madison, WI, Soil Science Society of America, Inc.

Donner, H., and Grossl, P., 2002, Carbonates and Evaporites, *in* Dixon, J., Schulze, D., and Amonette, J., eds, Soil Mineralogy with Environmental Applications, Volume 7: Soil Science Society of American Book Series: Madison, WI, Soil Science Society of America, Inc., p. 199-228.

Dreimanis, A., 1962, The Chittick Procedure: Journal of Sedimentary Petrology, v. 32., pp. 520-529.

Evangelou, V.P., and Zhang, Y.L., 1995, A review - pyrite oxidation mechanism and acid-mine drainage prevention: Critical Review in Environmental Science and Technology, v. 25, p. 141-199.

Fanning, D.S., Rabenhorse, M.C., Burch, S.N., Islam, K.R., and Tangren, S.A., 2002, Sulfides and Sulfates, *in* Dixon, J., Schulze, D., and Amonette, J., eds., Soil Mineralogy with Environmental Applications: Soil Science Society of America Book Series: Madison, WI, Soil Science Society of America, Inc., p. 229-260.

Fernandez-Caliani, J.C., Barba-Brioso, C., and Perez-Lopez, R., 2008, Long-term interaction of wollastonite with acid mine water and effects on arsenic and metal removal: Applied Geochemistry, v. 23, p. 1288-1298.

Fitzpatrick, R.W., and Chittleborough, D.J., 2002, Titanium and Zirconium Minerals, *in* Dixon, J., Schulze, D., and Amonette, J., eds., Soil Mineralogy with Environmental Applications: Madison, WI, Soil Science Society of America, Inc.

Flakova, R., Zenisova, Z., Sracek, O., Krcmar, D., Ondrejkova, I., Chovan, M., Lalinska, B., and Fendekova, M., 2012, The behavior or arsenic and antimony at Pezinok mining site, southwestern part of the Slovak Republic: Environmental Earth Sciences, v. 66, p. 1043-1057.

Garcia, A., Armienta, M.A., and Cruz, O., 2001, Sources, distribution and fate or arsenic along with Toliman River, Zimapan, Mexico, In Acreman, M.C., ed., Hydro-ecology: Linking Hydrology and Aquatic Ecology Proceedings of the International Association of Hydrological Sciences July 1999 Meeting: Birmingham, UK, IAHS Publ. No. 266.

Garcia, C., Ballester, A., Gonzalez, F., and Blazquez, M.L., 2004, Factors affecting the transformation of a pyritic tailing: scaled-up column tests: Journal of Hazardous Materials, v. A118, p. 35-43.

Garcia, G., and Querol, F., 1991, Description of some deposits in the Zimapan District, Hidalgo: The Geology of North America, v. P-3, p. 295-313.

Hillier, S., 1999, Use of an air brush to spray dry samples for X-ray powder diffraction: Clay Minerals, v. 34, p. 127-135.

Jambor, J.L., 1994, Mineralogy of sulfide-rich tailings and their oxidation products: Environmental Geochemistry of Sulfide Mine-Waste, v. 22, p. 59-102.

Jambor, J.L., Dutrizac, J.E., and Chen, T.T., 2000, Contribution of specific minerals to the neutralization potential in static tests, 5th International Conference on Acid Rock Drainaige (ICARD): Denver, CO.

Johnson, C.A., 1986, The regulation of trace element concentrations in river and estuarine waters contaminated with acid mine drainage: the adsorption of Cu and Zn on amorphous Fe oxyhydroxides: Geochimica et Cosmochimica Acta, v. 50, p. 2433-2438.

Johnson, D.B., and Hallberg, K.B., 2005, Acid mine drainage remediation options: a review: Science of the Total Environment, v. 338, p. 3-14.

Jonckbloedt, R.C., 1997, Olivine dissolution in sulphuric acid at elevated temperatures - implications for the olivine process, an alternate waste acid neutralizing process: Journal of Geochemical Exploration, v. 62, p. 337-346.

Jurjovec, J., Placek, C.J., and Blowes, D.W., 2002, Acid nuetralization mechanisms and metal release in mine tailings: A laboratory column experiment: Geochimica et Cosmochimica Acta, v. 66, p. 1511.

Karathanasis, A.D., 2002, Mineral equillibria in environmental soil systems, *in* Dixon, J., Schulze, D., and Amonette, J., eds, Soil Mineralogy with Environmental Applications: Madison, WI, Soil Science Society of America, Inc.

Khaodhiar, S., Azuzzian, M., Osathapan, K., and Nelson, P., 1999, Copper, chromium, and arsenic adsorption and equillibrium modeling in an iron-oxide coated sand, background electrolyte system: Water, Air and Soil Pollution, v. 119, p. 105-120.

Lizarraga-Mendiola, L., Gonzalez-Sandoval, M.R., Duran-Dominguez, M.C., and Marquez-Herrera, C., 2009, Geochemical behavior of heavy metals in a Zn-Pb-Cu mining in the State of Mexico (central Mexico): Environmental Monitoring and Assessment, v. 155, p. 355-372.

Mendez, M., and Armienta, M.A., 2002, Arsenic phase distribution in Zimapan mine tailings, Mexico: Geofisca Internacional, v. 42, p. 131-140.

Moncur, M.C., Jambor, J.L., Ptacek, C.J., and Blowes, D.W., 2009, Mine drainage from the weathering of sulfide minerals and magnetite: Applied Geochemistry, v. 24, p. 2362-2373.

Murphy, W.M., and Helgeson, H.C., 1987, Thermodynamic and kinetic constraints on reaction rates among minerals and aqueous solutions. III. Activated complexes and the pH-dependence of the rates of feldspar, pyroxene, wollastonite, and olivine hydrolysis: Geochimica et Cosmochimica Acta, v. 51, p. 3137-3153.

Nicholson, A.D., 2003, Incorporation of silicate buffering in predicting acid rock drainage from mine wastes - a mechanistic approach: Mining Engineering, v. 55, p. 33-37.

Ongley, L.K., Armienta, M.A., and Mango, H., 2003, Concentrations of heavy metals in soil, Zimapan, Mexico: Journal de Physique IV, v. 107, p. 983-986.

Ramdohr, P., 1969, The Ore Minerals and their Intergrowths: Oxford, UK, Pergamon Press.

Ranville, M., Rough, D., and Flegal, A.R., 2004, Metal attenuation at the abandoned Speceville copper mine: Applied Geochemistry, v. 19, p. 803-815.

Ribet, I., Ptacek, C.J., Blowes, D.W., and Jambor, J.L., 1995, The potential for metal release by reductive dissolution of weathered mine tailings: Journal of Contaminant Hydrology, v. 17, p. 239-273.

Romero, F.M., Armienta, M.A., and Gonzalez-Hernandez, G., 2007, Solid-phase control on the mobility of potentially toxic elements in an abandoned lead/zinc tailings impoundment: Applied Geochemistry, v. 22, p. 109-127.

Romero, F.M., Armienta, M.A., Villasenor, G., and Gonzalez, J.L., 2006, Mineralogical constraints on the mobility of arsenic in tailings from Zimapan, Hidalgo, Mexico: International Journal of Environment and Pollution, v. 26.

Scracek, O., Armienta, M.A., Rodriguez, R., and Villasenor, G., 2009, Discrimination between diffuse and point sources of arsenic at Zimapan, Hidalgo state, Mexico: Journal of Environmental Monitoring, v. 12, p. 329-337.

Silverman, M.P., 1967, Mechanism of bacterial pyrite oxidation: Journal of Bacteriology, v. 94, p. 1046.

Simon, M., Martin, F., Garcia, I., Bouza, P., Dorronsoro, C., and Aguilar, J., 2005, Interaction of limestone grains and acidic solutions from the oxidation of pyrite tailings: Environmental Pollution, v. 135, p. 65-72.

Singer, P., and Stumm, W., 1970, Acidic mine drainage: the rate-determining step: Science, v. 167, p. 1121-1123.

Stoffregen, R.E., Alpers, C.N., and Jambor, J.L., 2000, Alunit-jarosite crystallography, thermodynamics and geochronology: Reviews in Mineralogy and Geochemistry, v. 40, p. 453-479.

Thompson, M.L., and Ukrainczyk, L., 2002, Micas, *in* Dixon, J., Schulze, D., and Amonette, J., eds, Soil Mineralogy with Envirionmental Applications: Madison, WI, Soil Science Society of America, Inc.

Weber, P.A., Thomas, J.E., Skinner, W.M., and Smart, R.C., 2005, A methodology to determine the acid-neutralization capacity of rock samples: The Canadian Mineralogist, v. 43, p. 1183-1192.

Young, R.A., 1993, The Rietveld Method, International Union of Crystallography Monograms on Crystallinity, Volume 5: New York, Oxford University Press.

APPENDIX A: SEM DATA

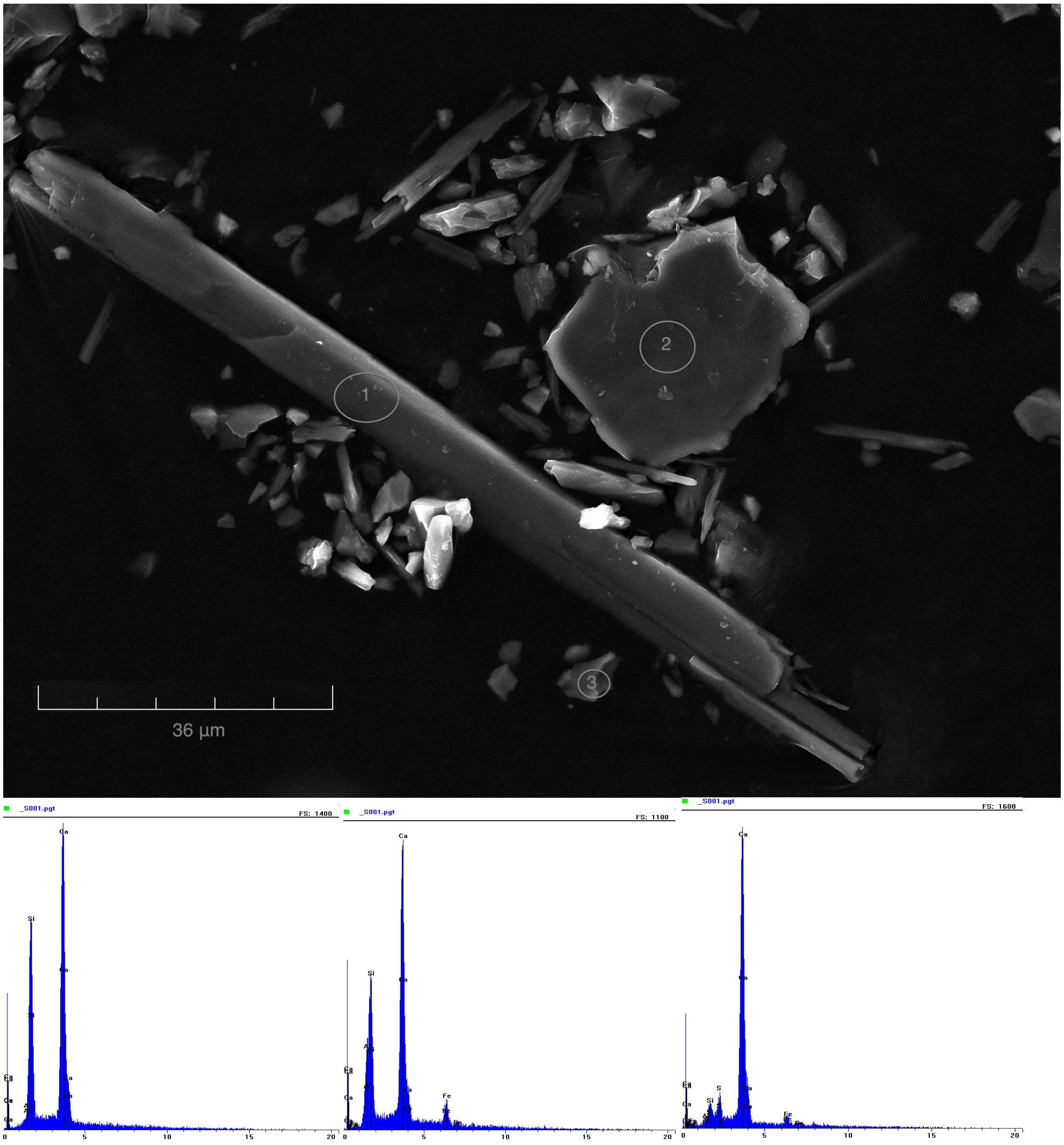

SEM backscattered image of unoxidized fine sample and EDS spectra (from left to right, 1, 2 and 3) for particles labeled 1, 2 and 3.

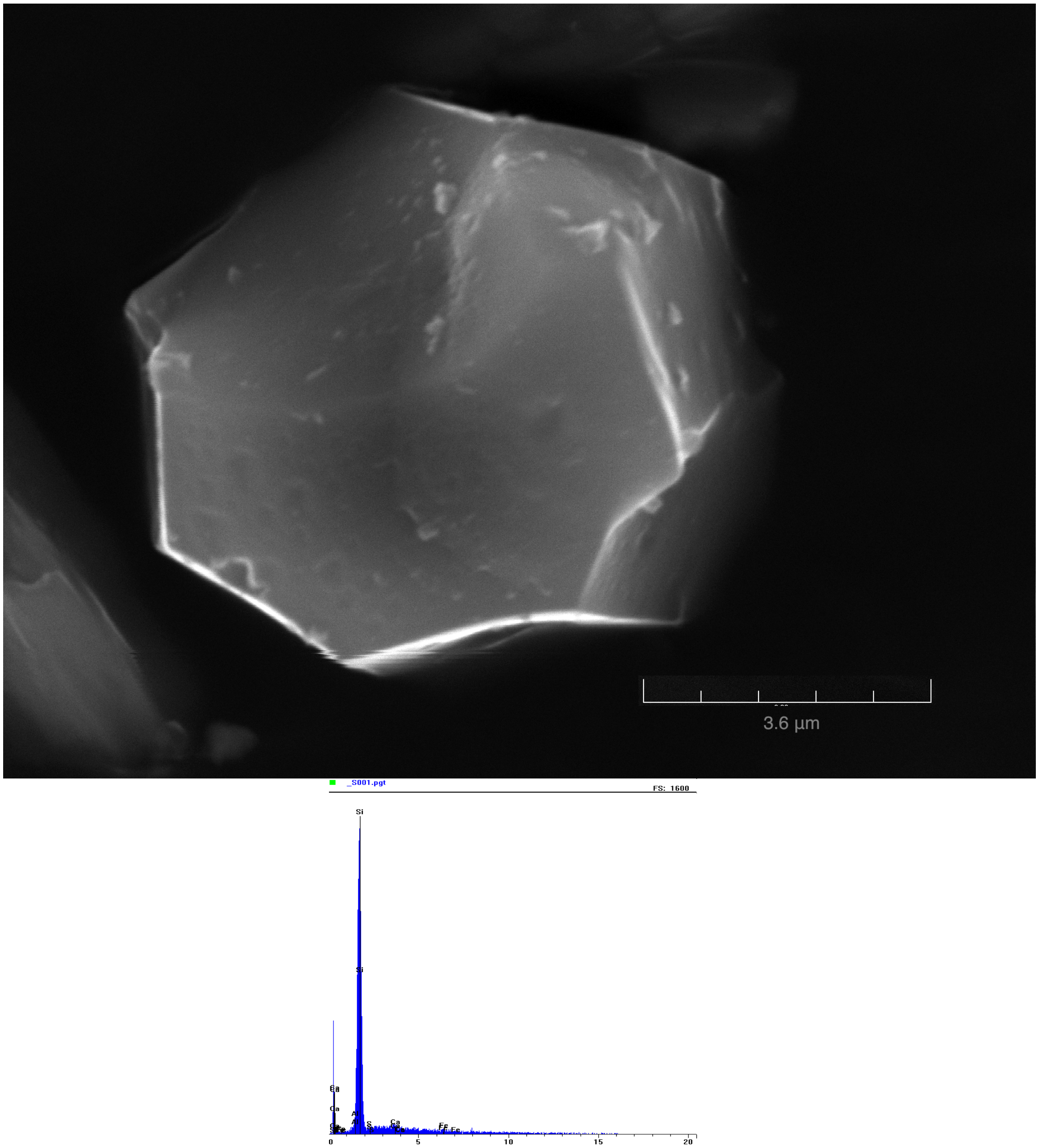

SEM image and EDS spectra of the fine unoxidized tailings

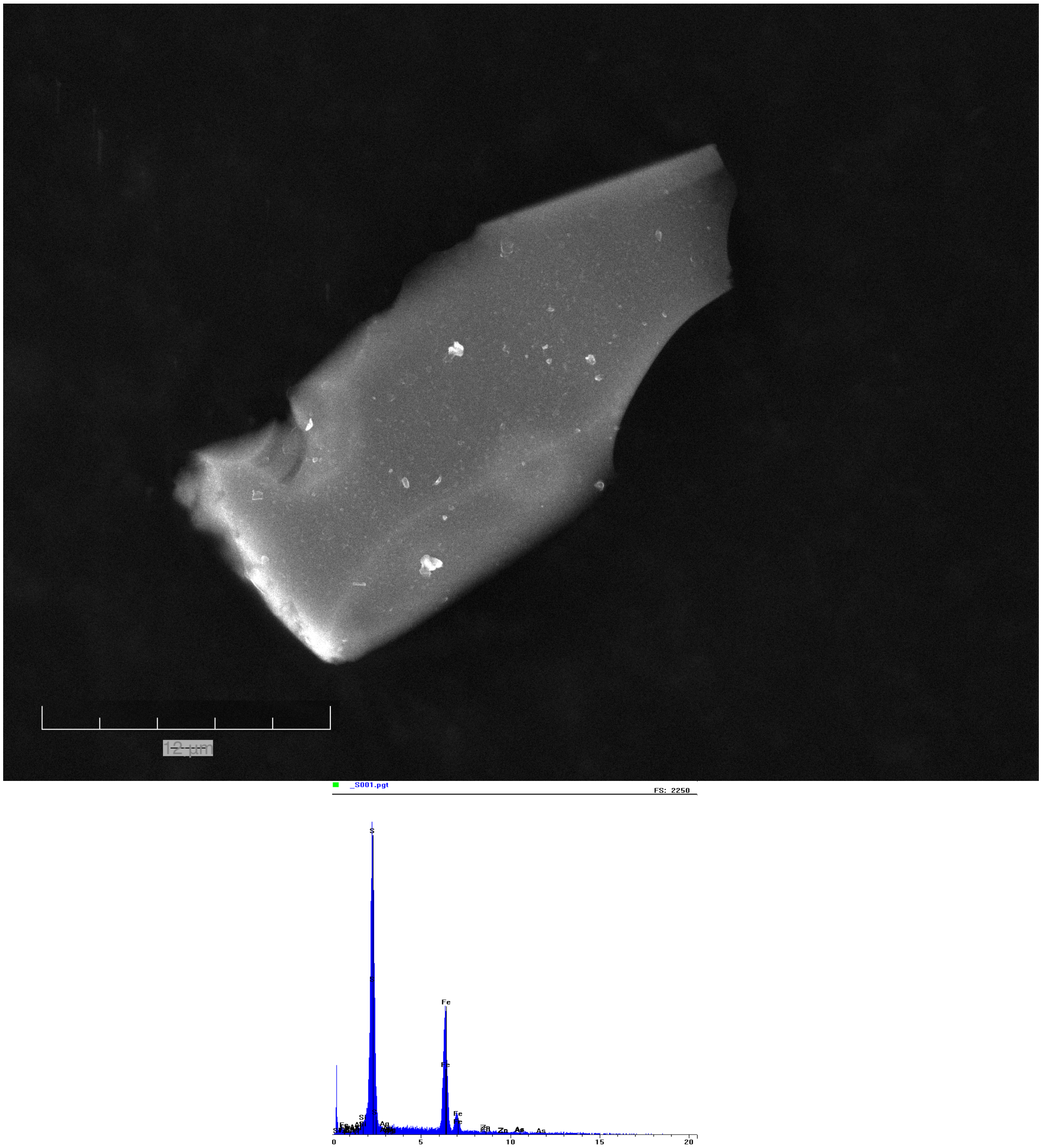

SEM image and EDS spectrum of fine unoxidized tailings.

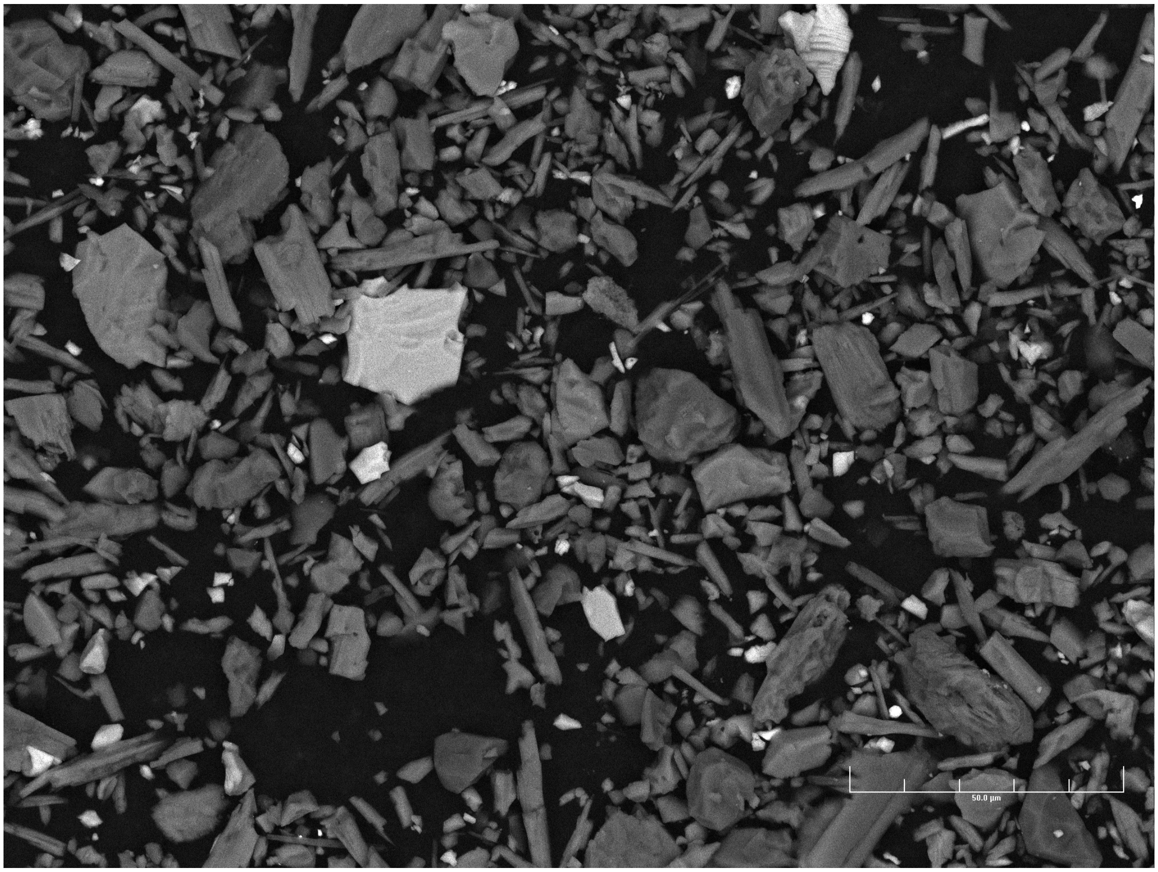

SEM backscattered image of the fine unoxidized tailings.

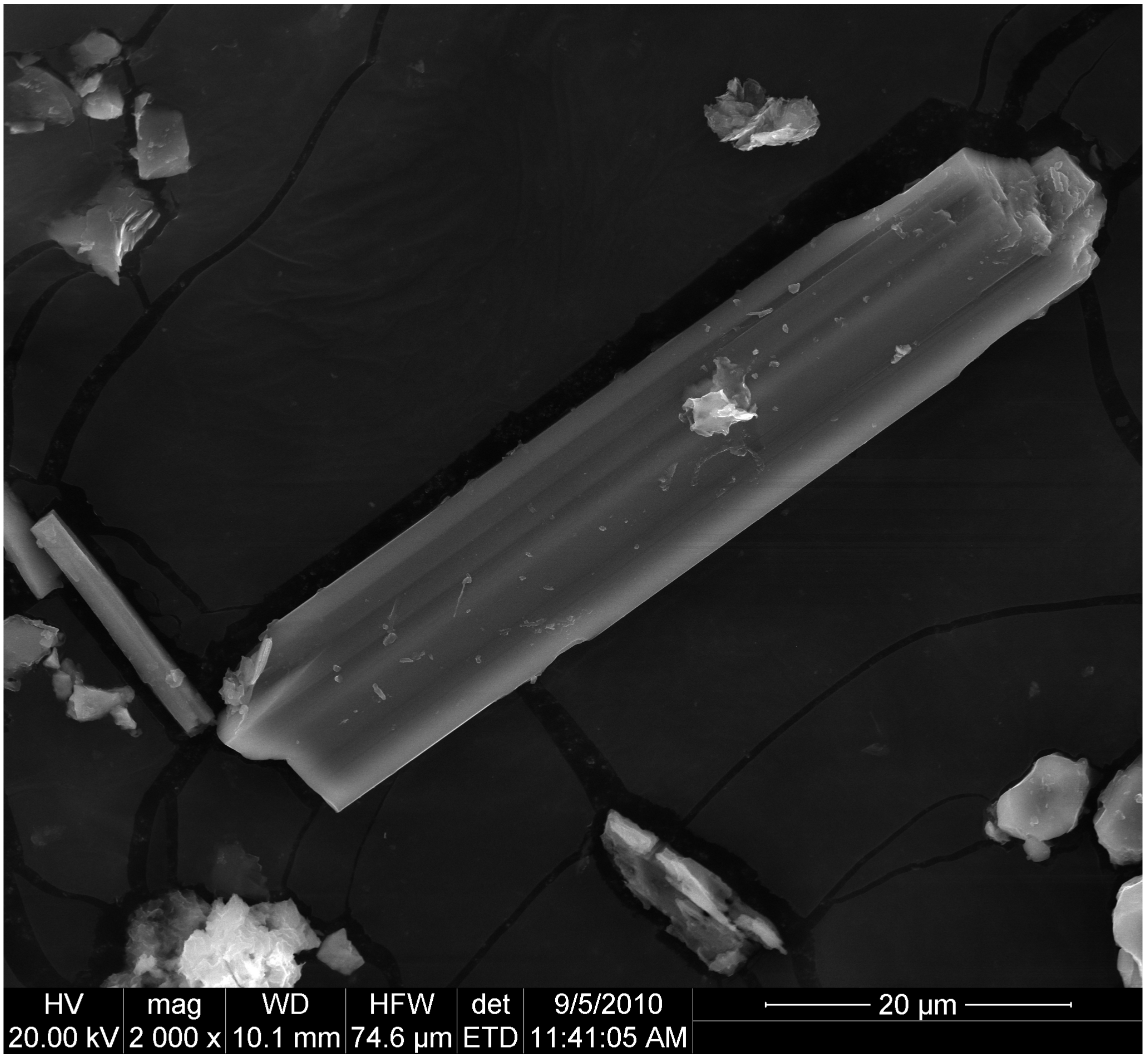

SEM image of the coarse unoxidized tailings.

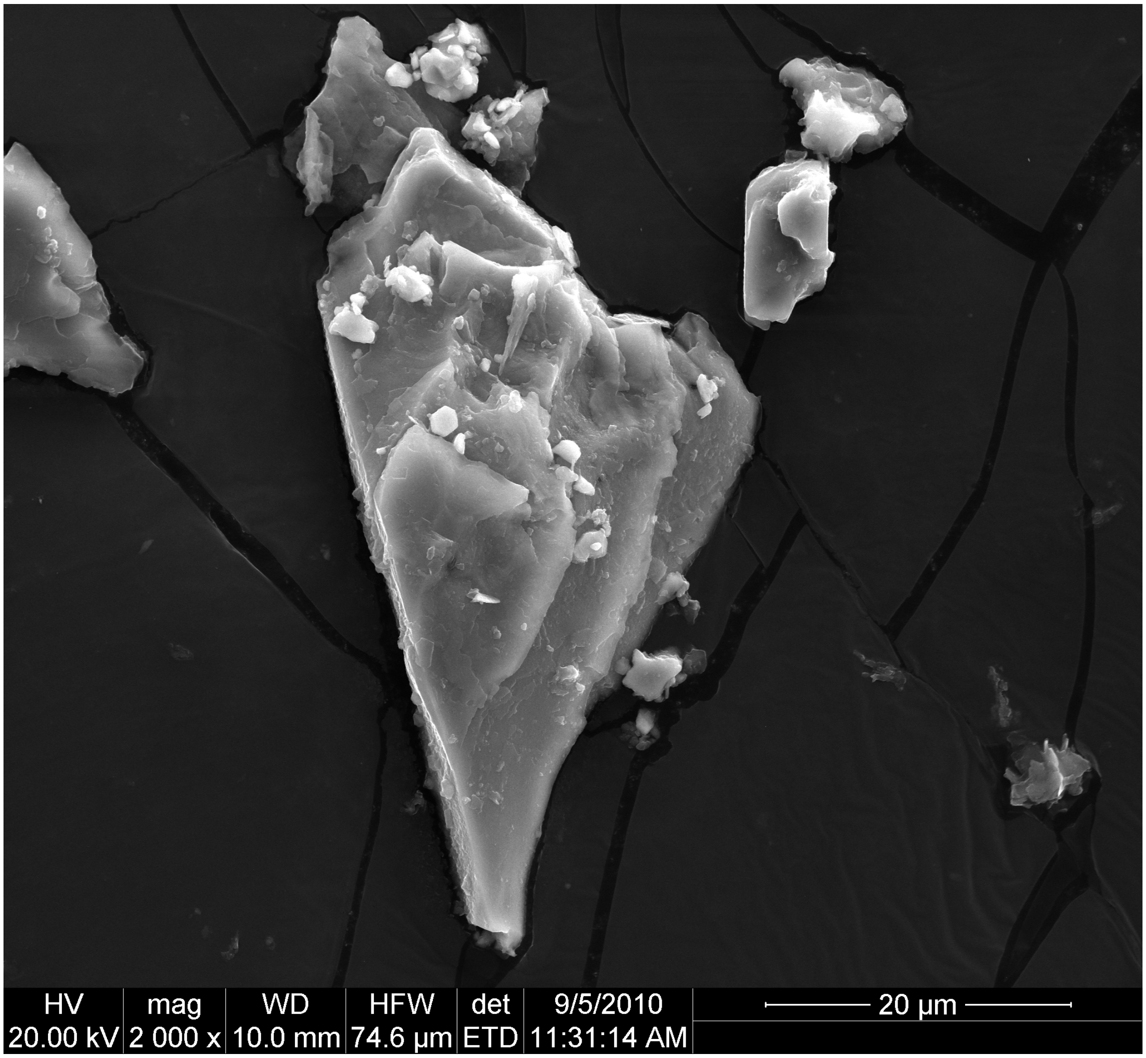

SEM Image of coarse unoxidized tailings.

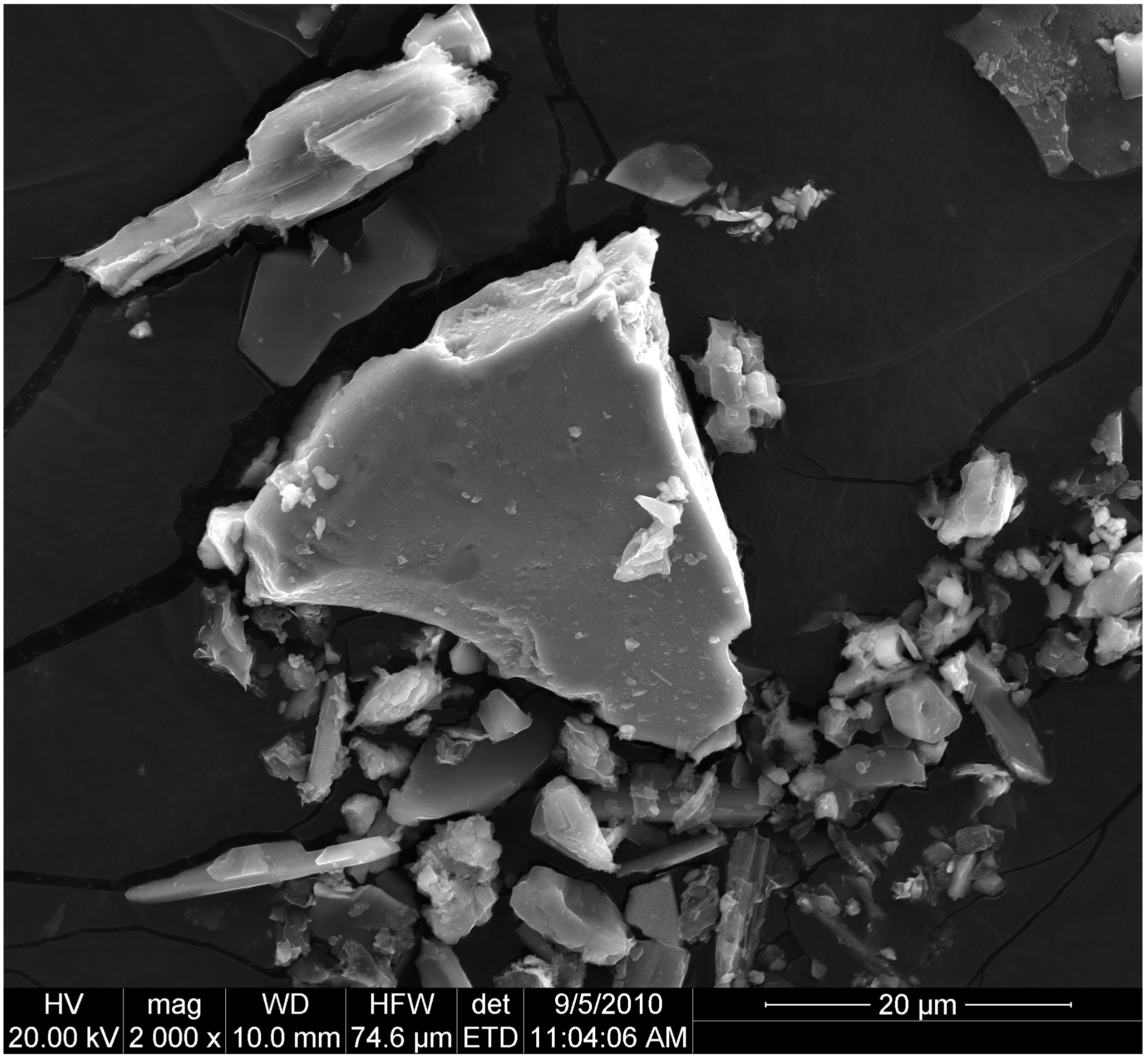

SEM image of coarse unoxidized tailings.

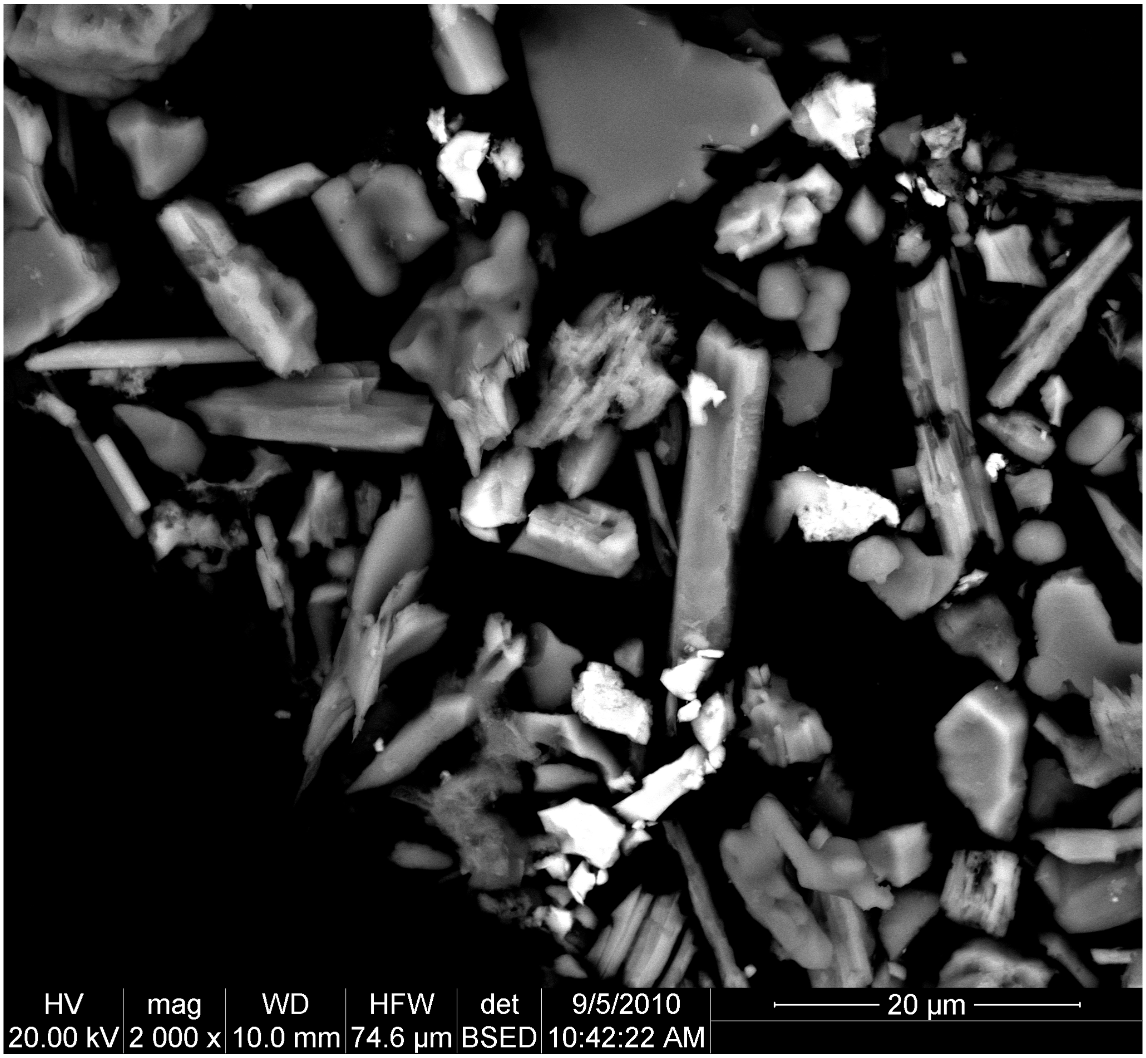

SEM backscattered image of coarse tailings.

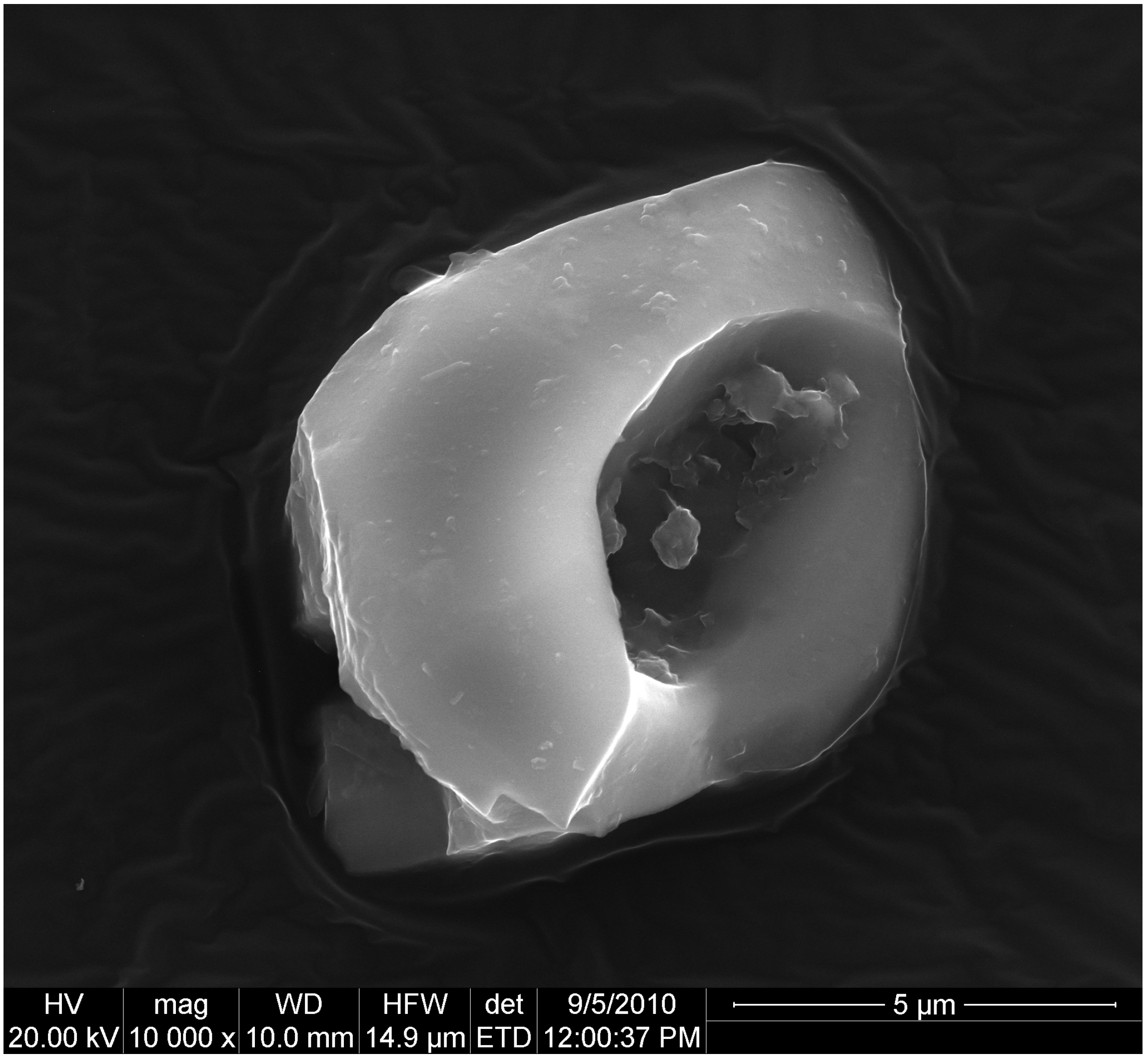

SEM image of coarse unoxidized tailings.

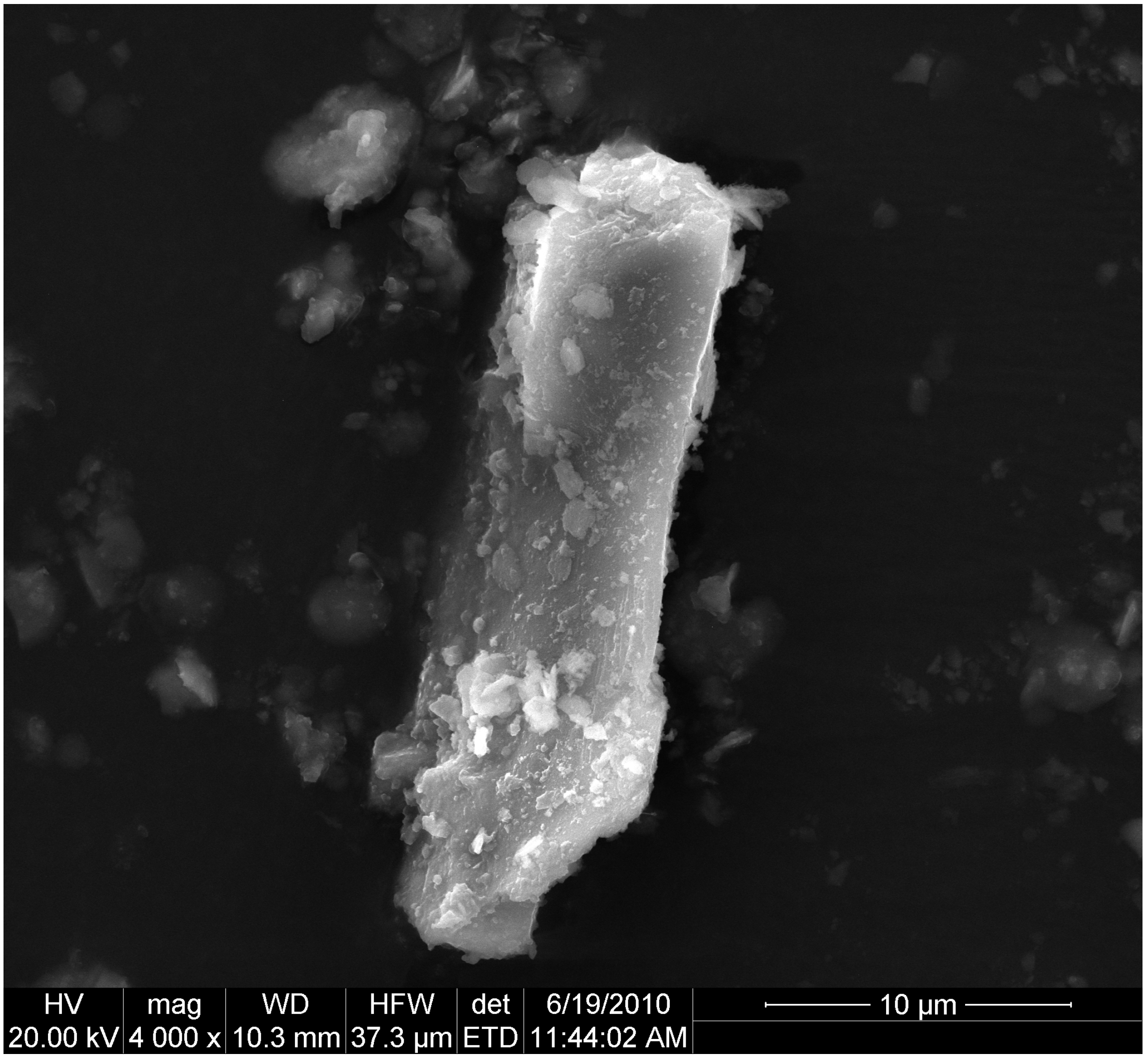

SEM image of the yellow oxidized tailings.

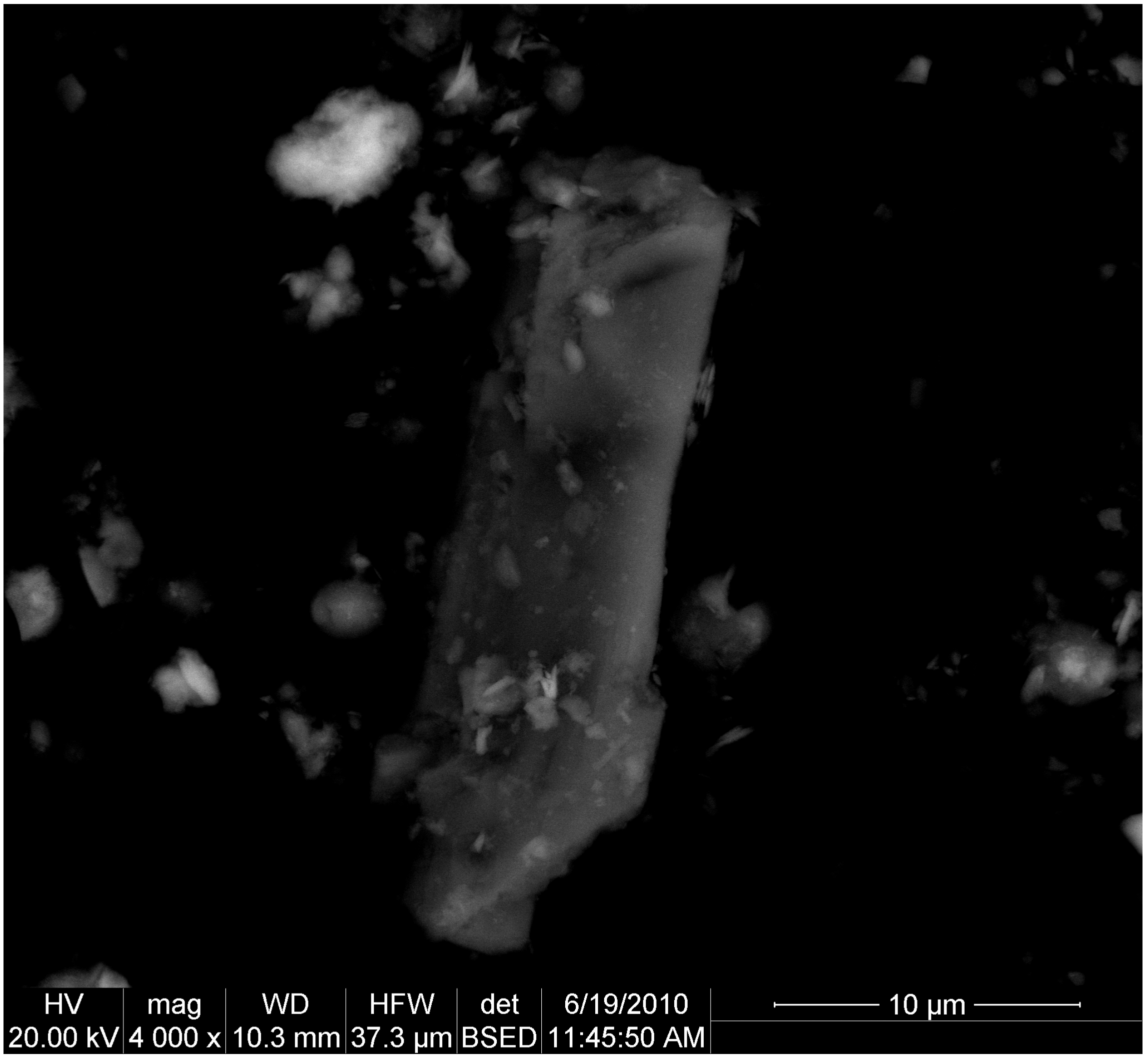

SEM backscattered image of the yellow oxidized tailings.

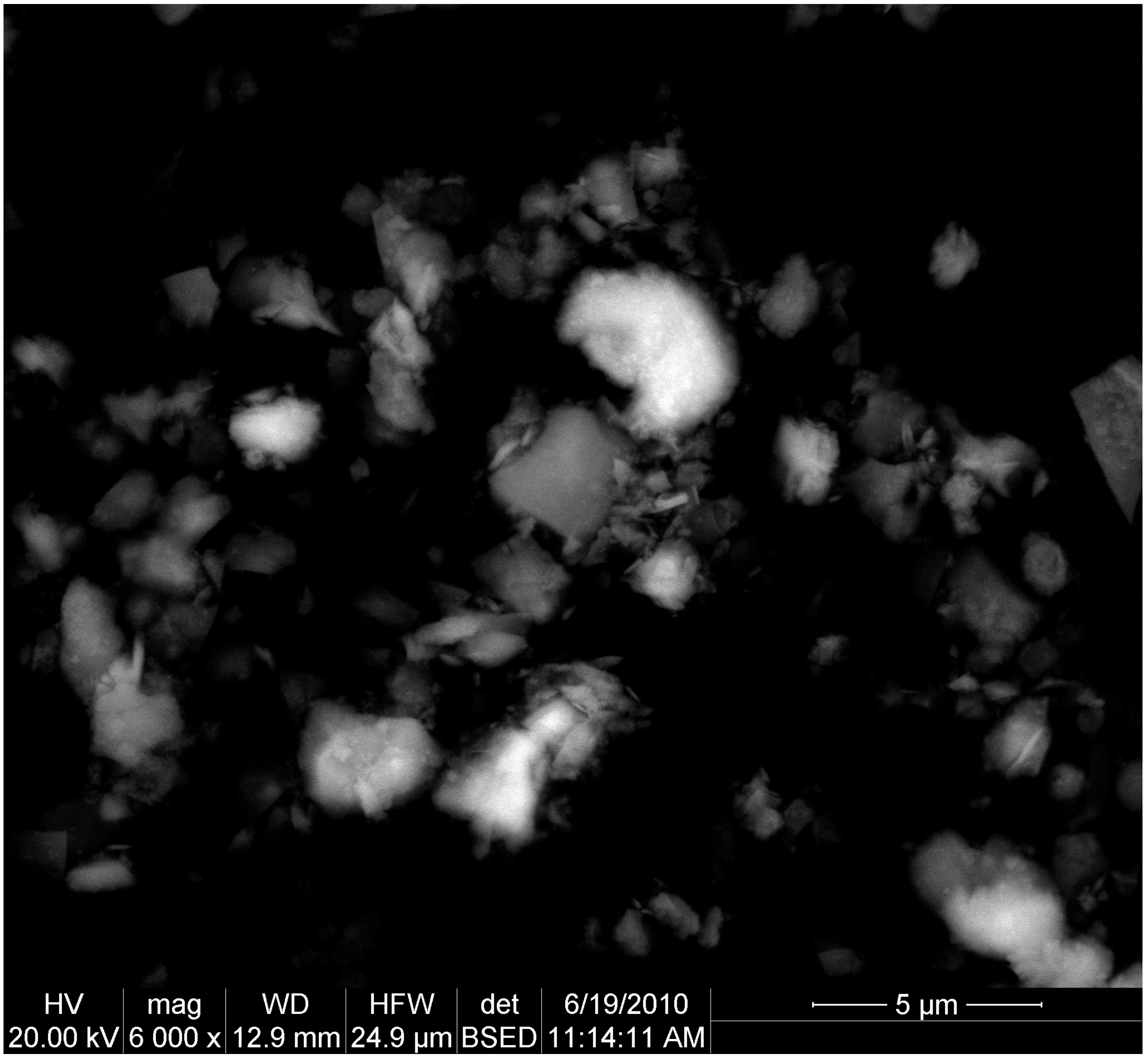

SEM backscattered image of the yellow oxidized tailings.

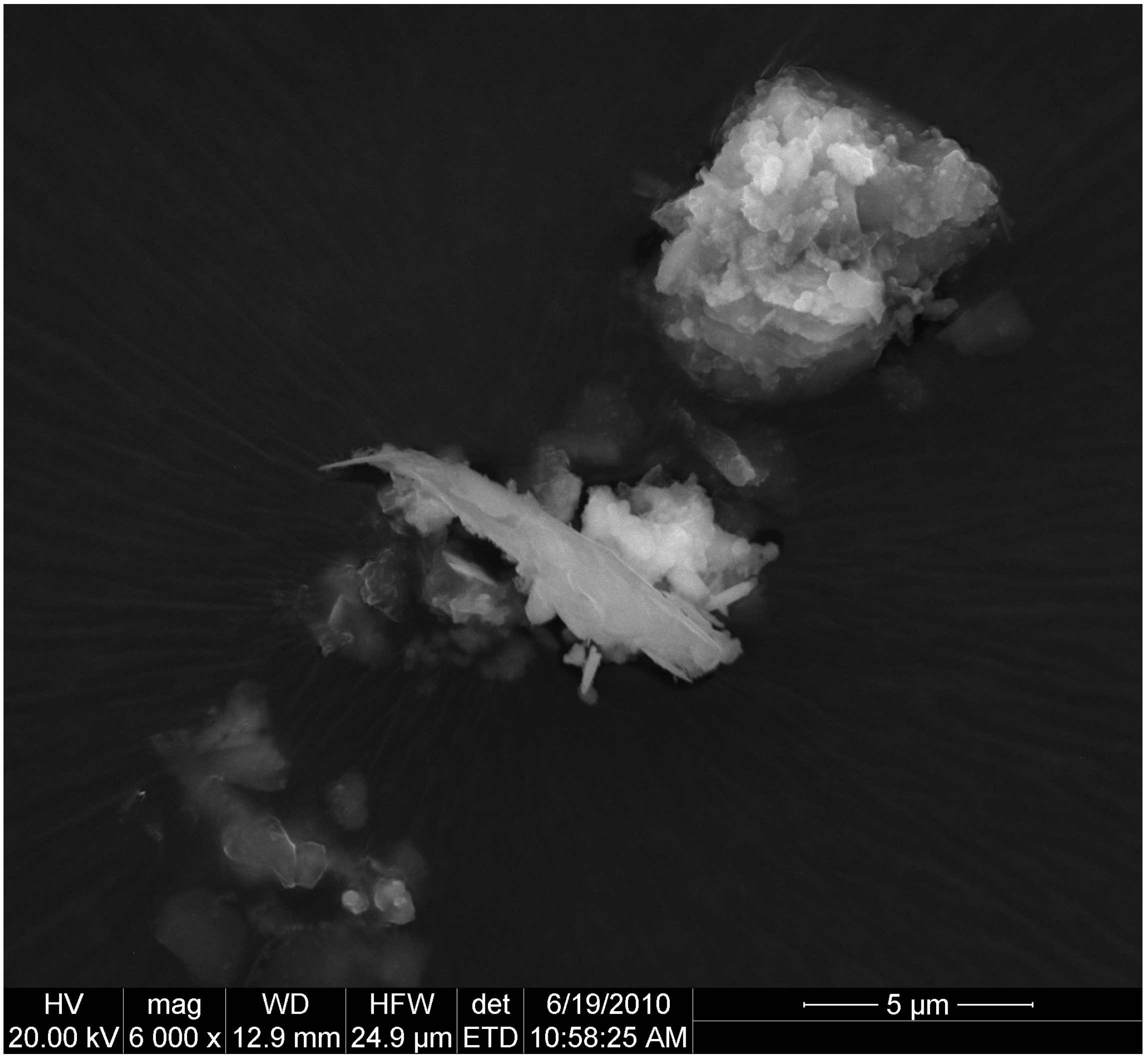

SEM image of the yellow oxidized tailings.

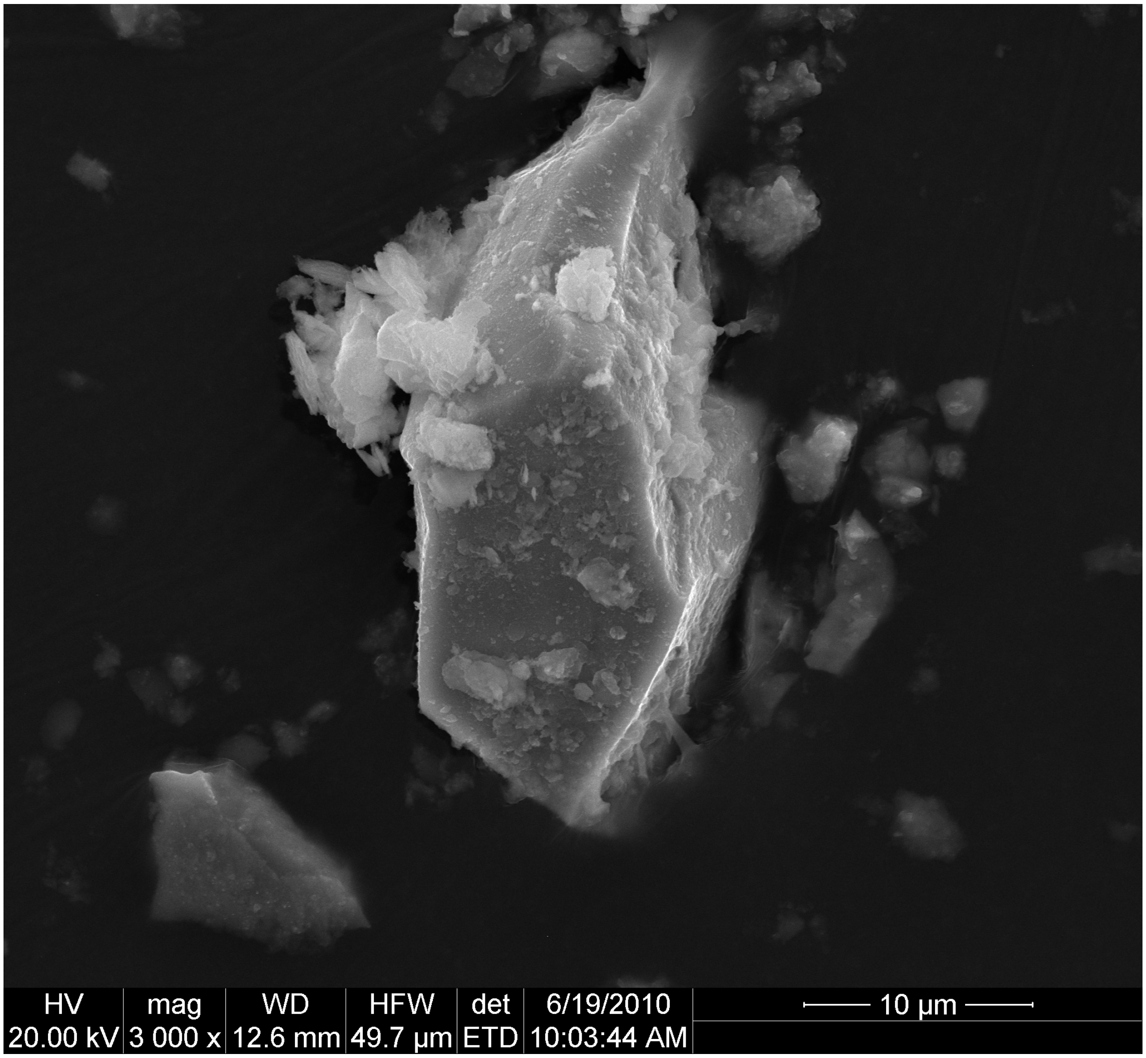

SEM Image of the red oxidized tailings.

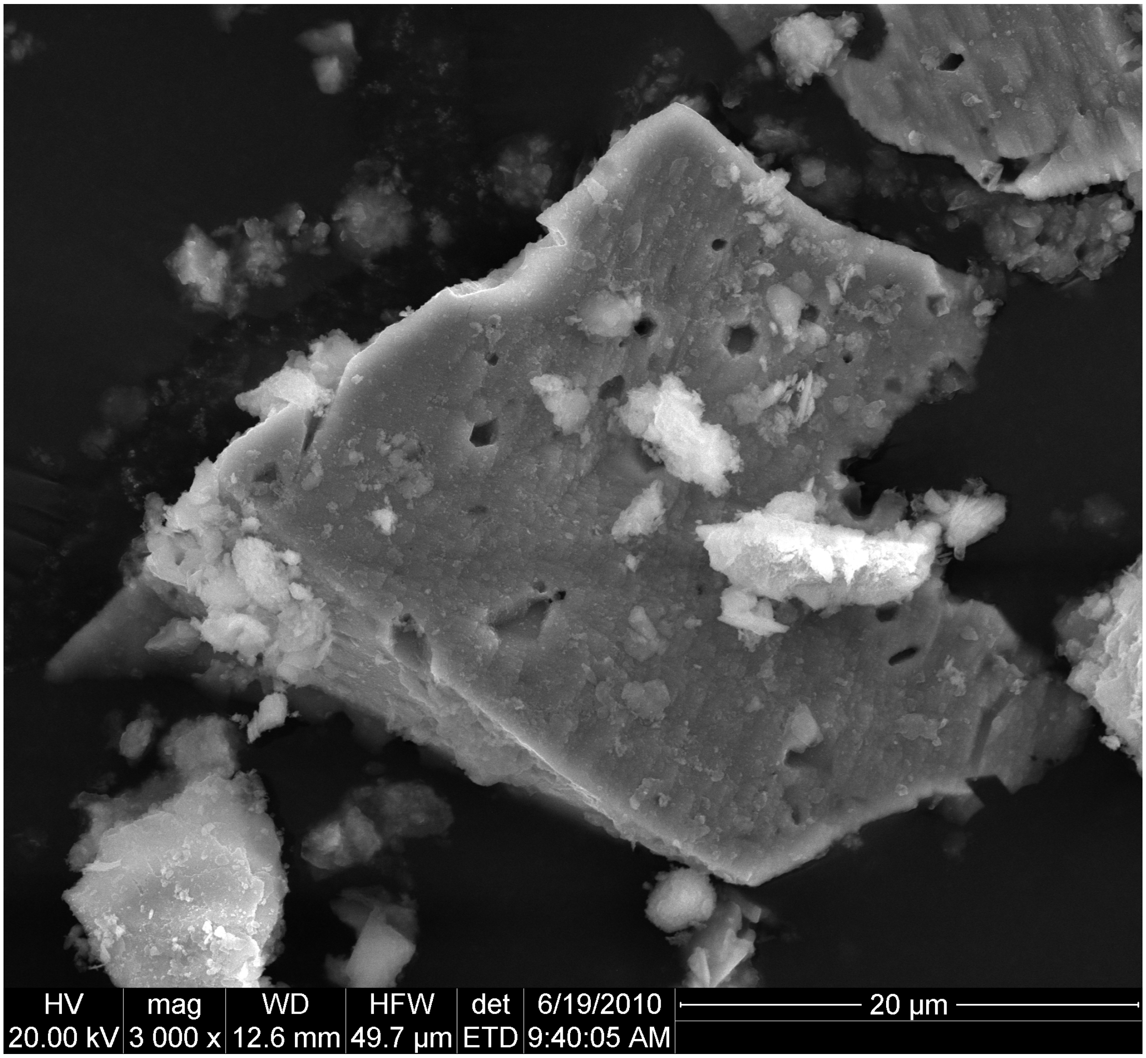

SEM image of the red oxidized tailings.

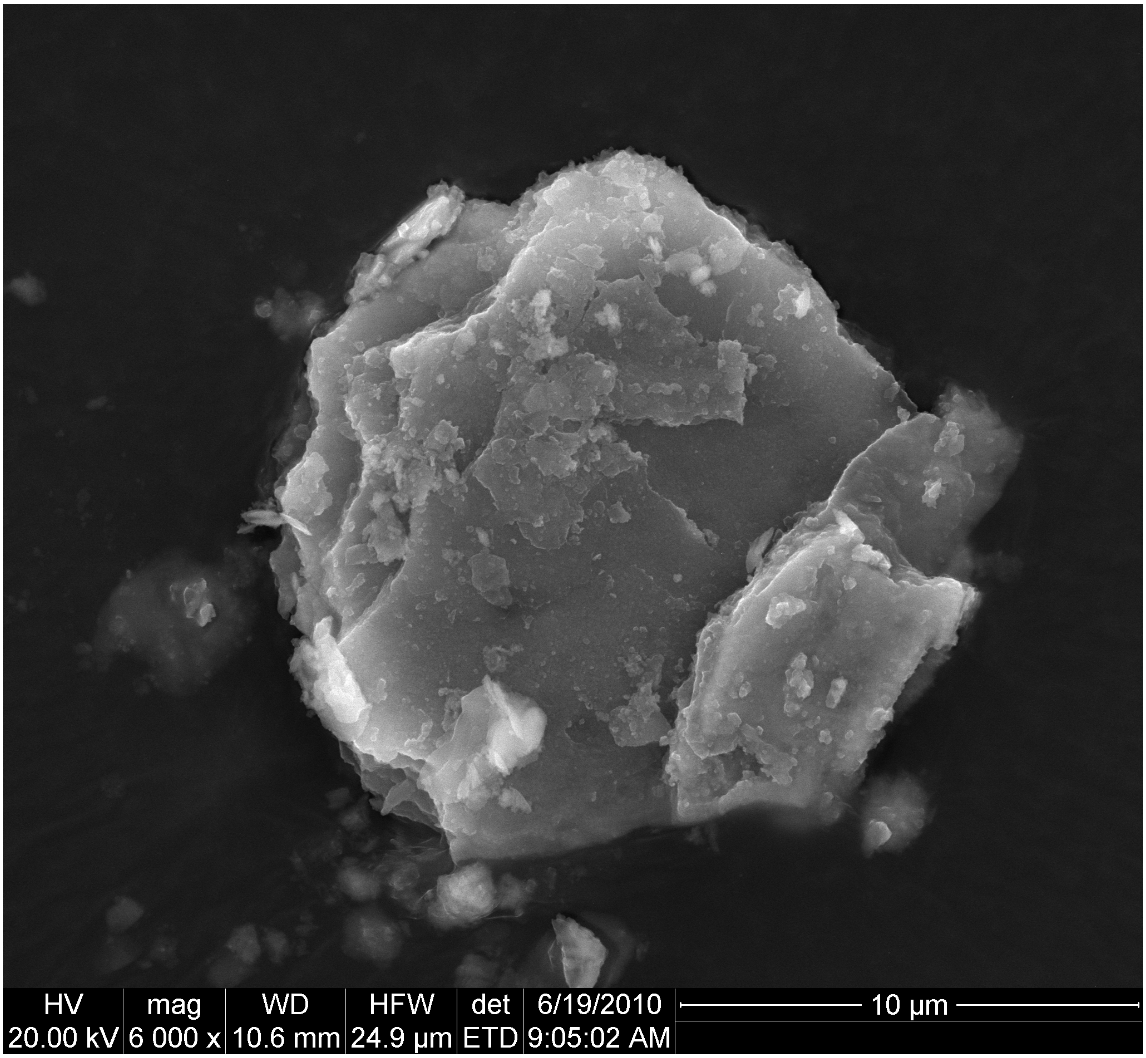

SEM image of the red oxidized tailings.

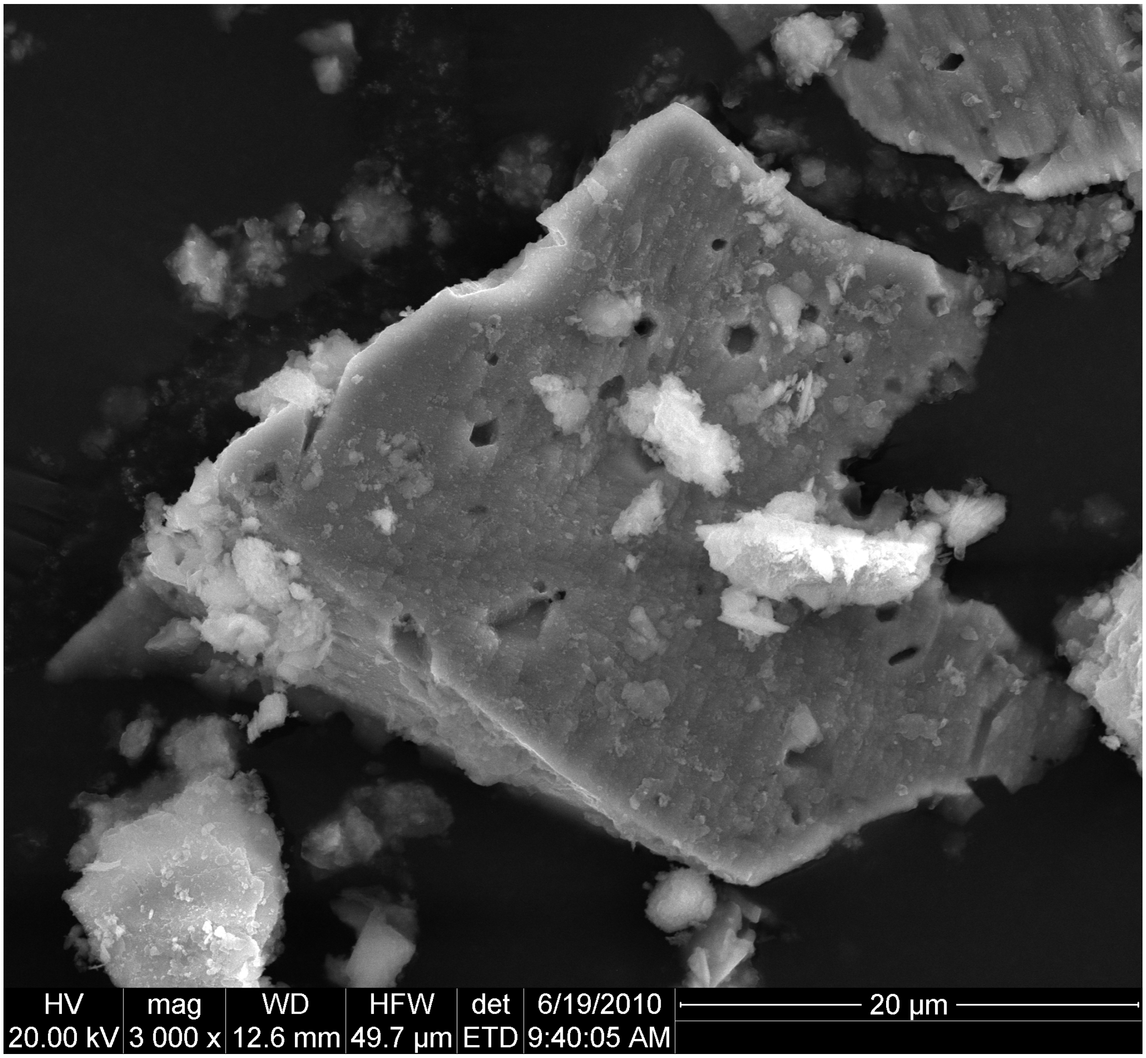
HV
20.00 kV
mag
3 000 x
WD
12.6 mm
HFW
49.7 µm
det
ETD
6/19/2010
9:40:05 AM
20 µm

APPENDIX B: TEM DATA

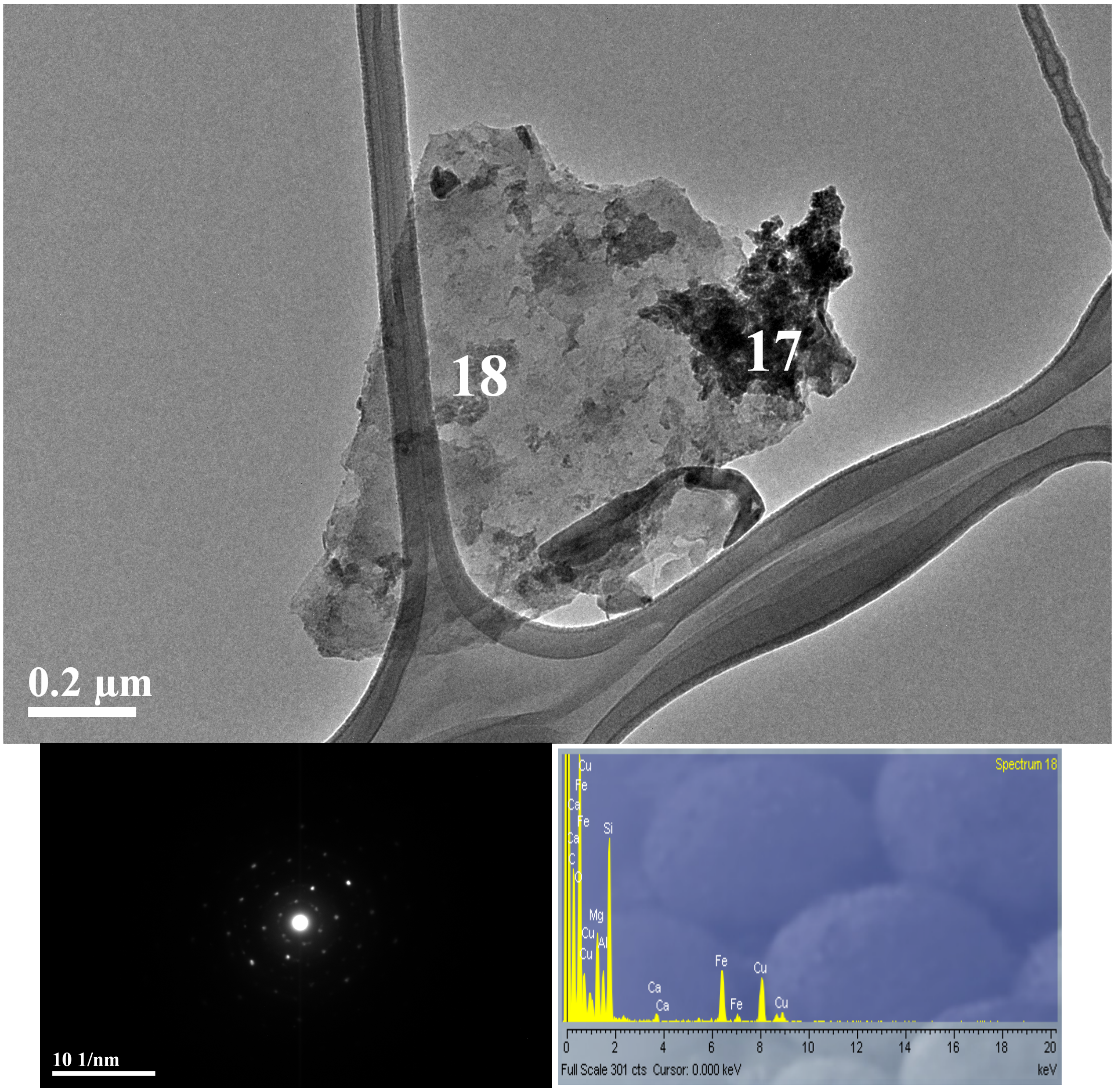

TEM image, SAED and EDS spectrum for the coarse unoxidized tailings

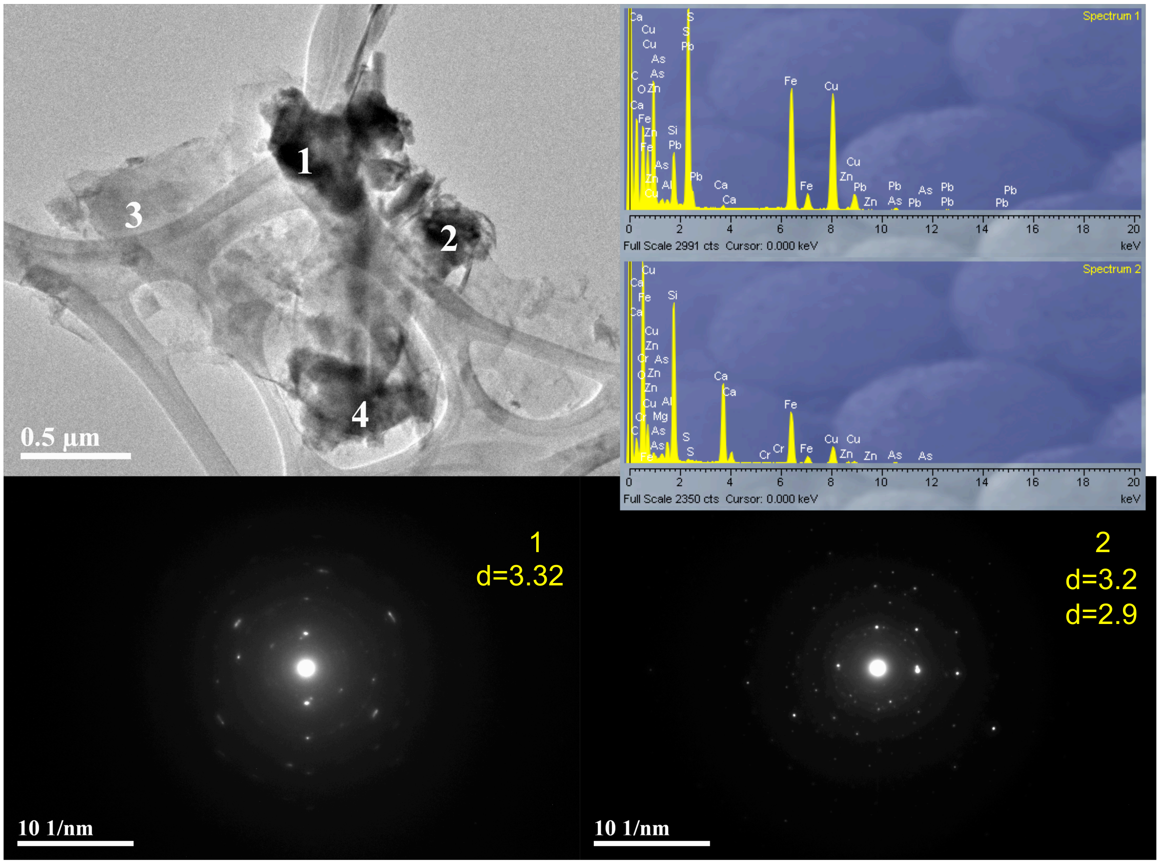

TEM image, SAED and EDS spectra for the fine onoxidized tailings.

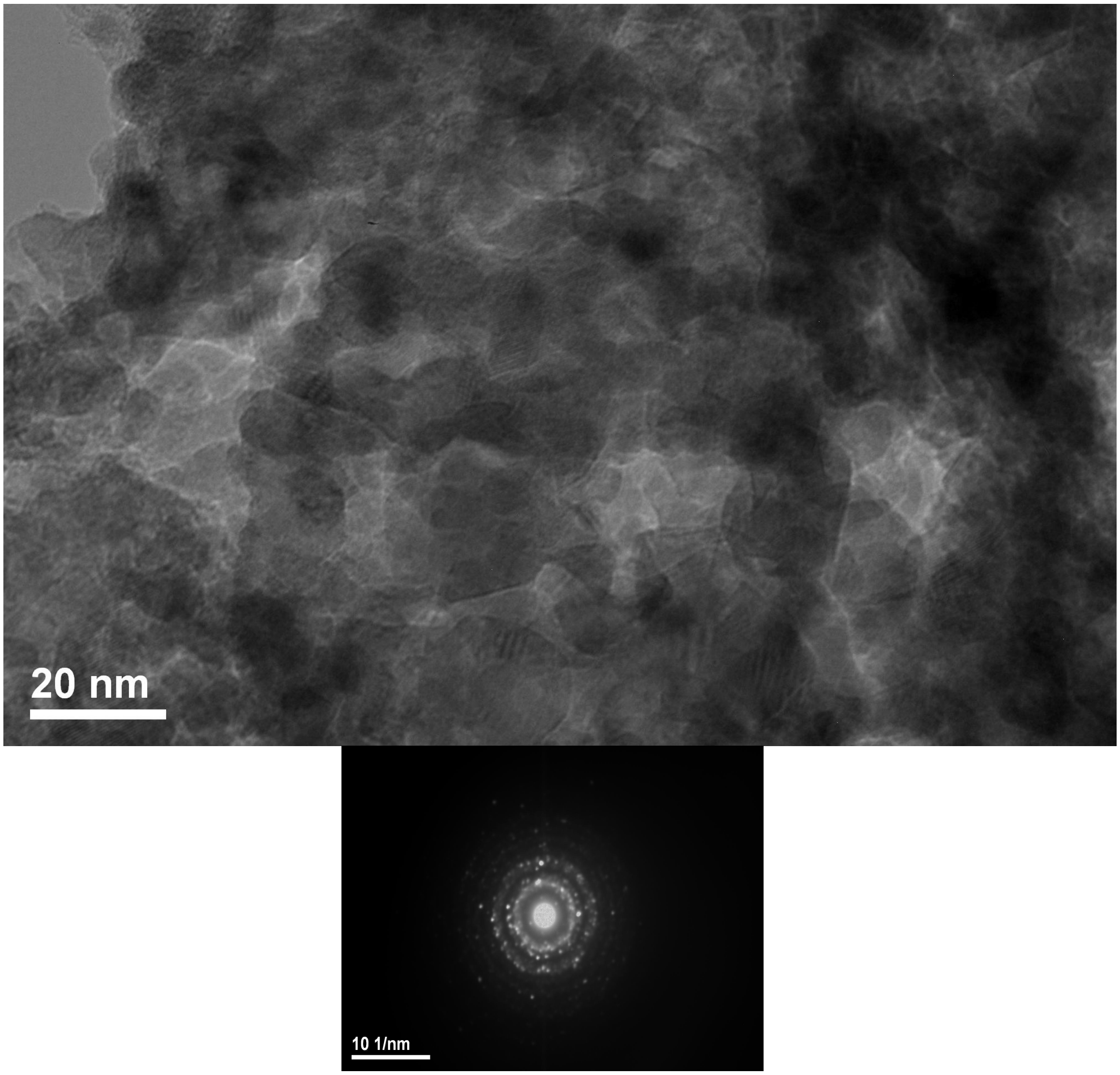

TEM image and SAED image for red oxidized tailings.

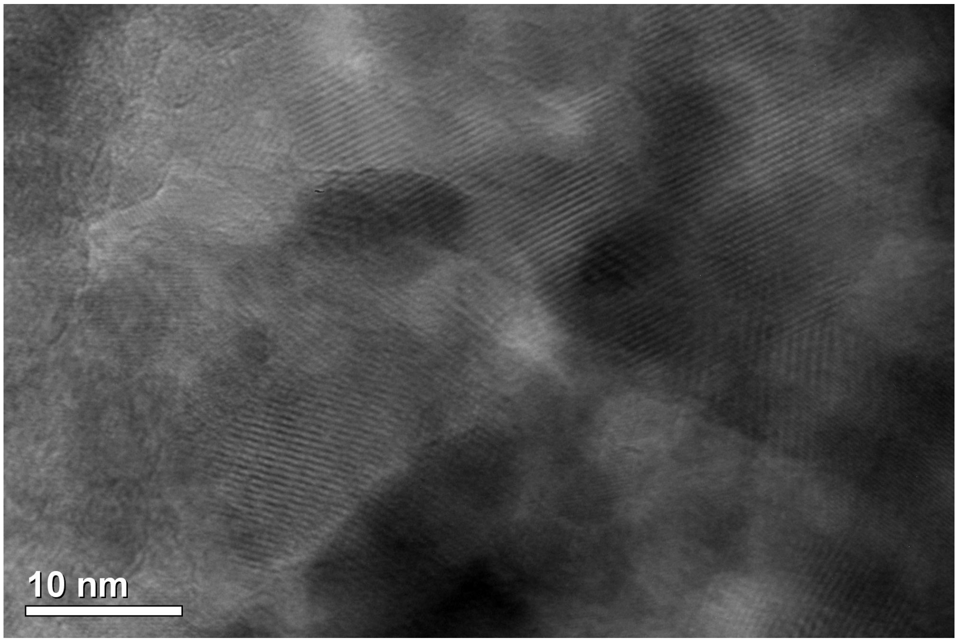

TEM image of the red oxidized tailings.

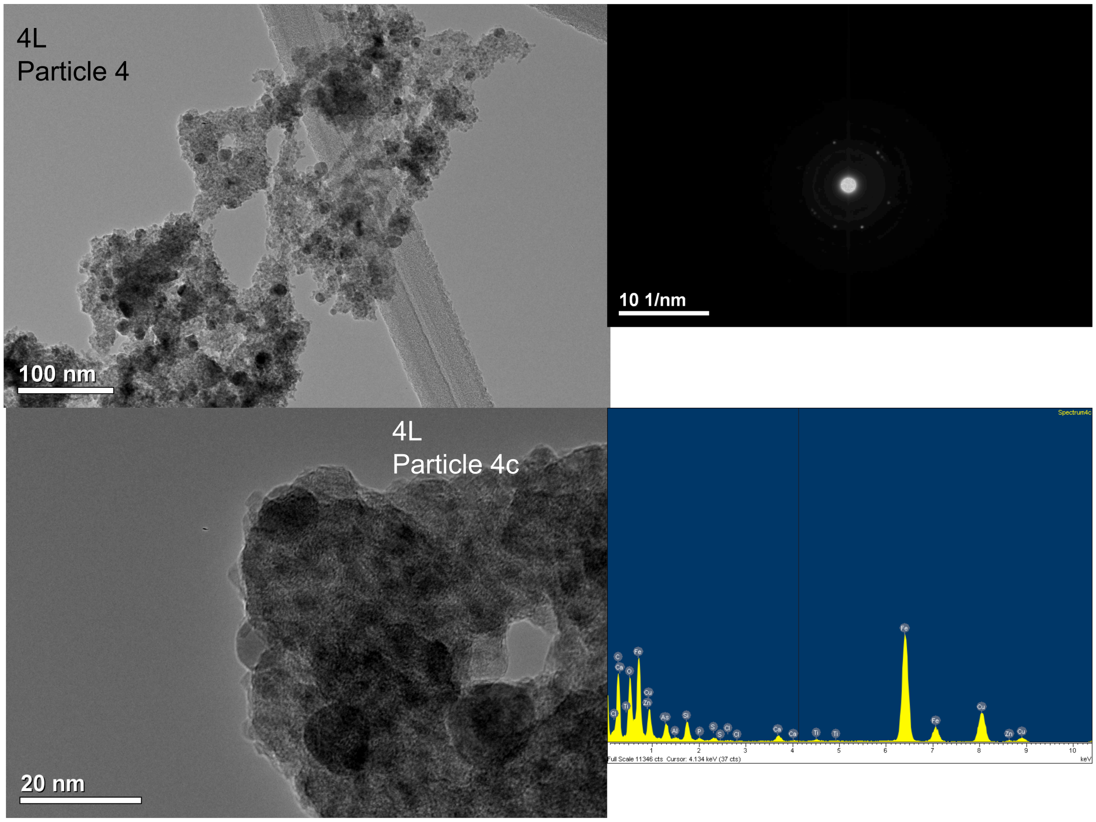

TEM images, SAED image and EDS spectrum for the red oxidized tailings.

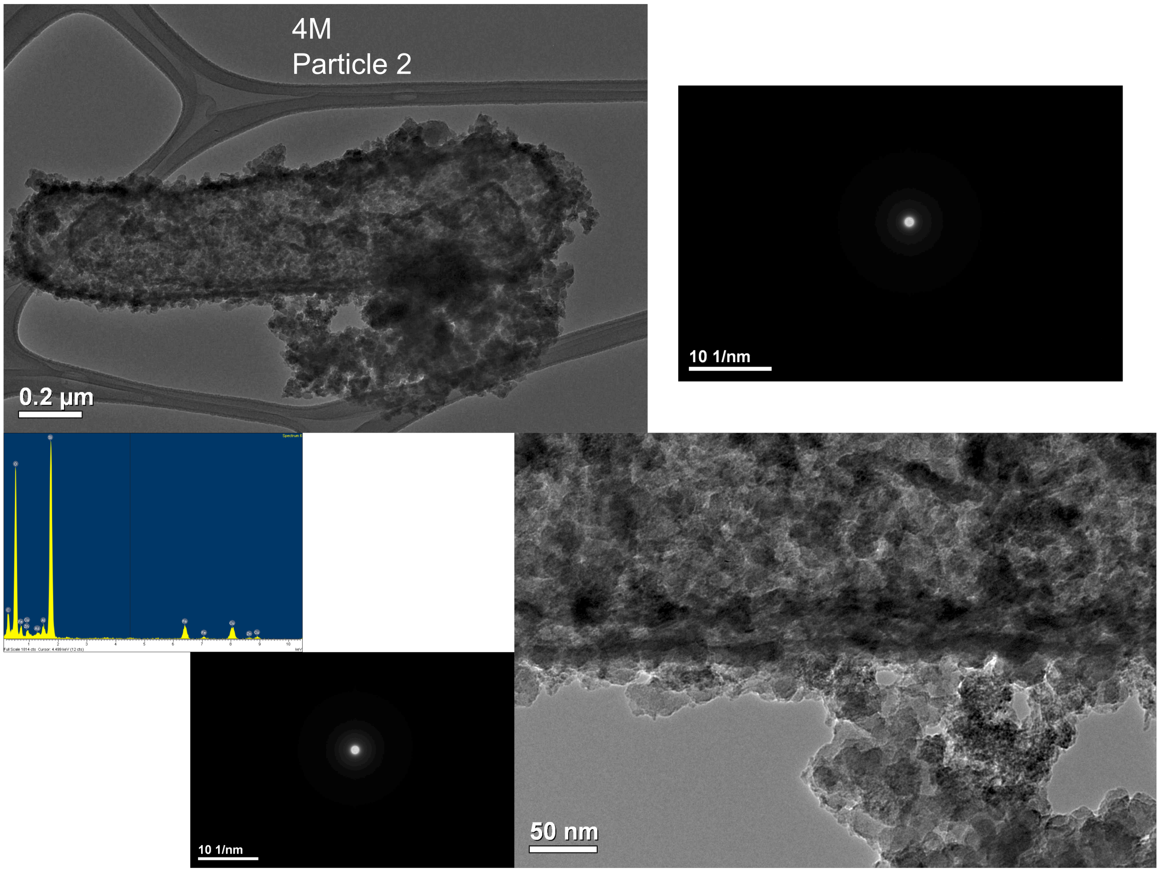

TEM images, SAED images and EDS spectrum for the red oxidized tailings.

APPENDIX C: RIETVELD REFINEMENT MODELS

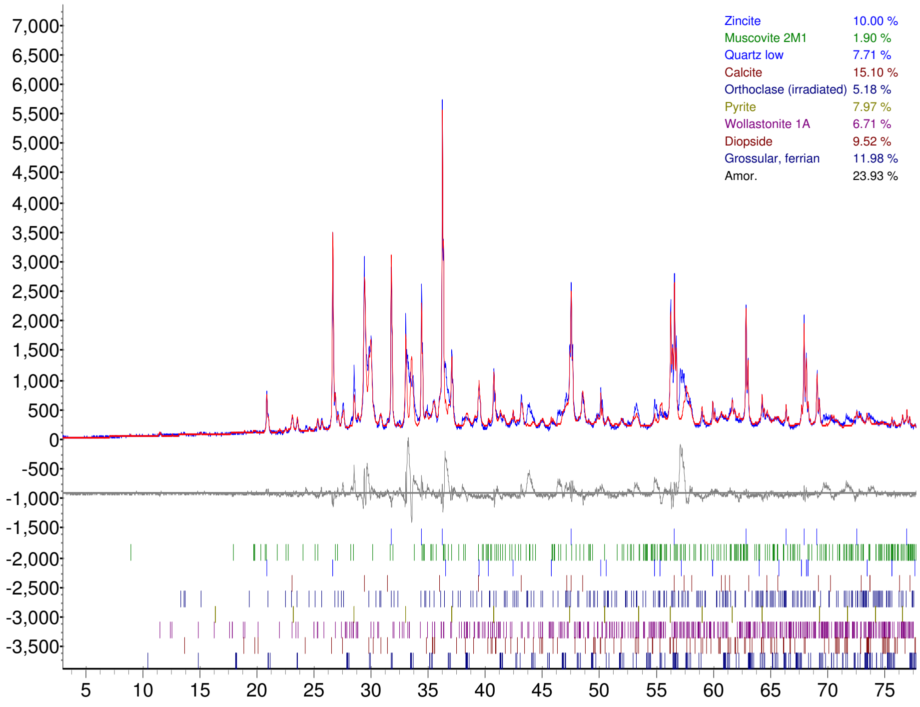

Rietveld refinement model for the coarse unoxidized tailings.

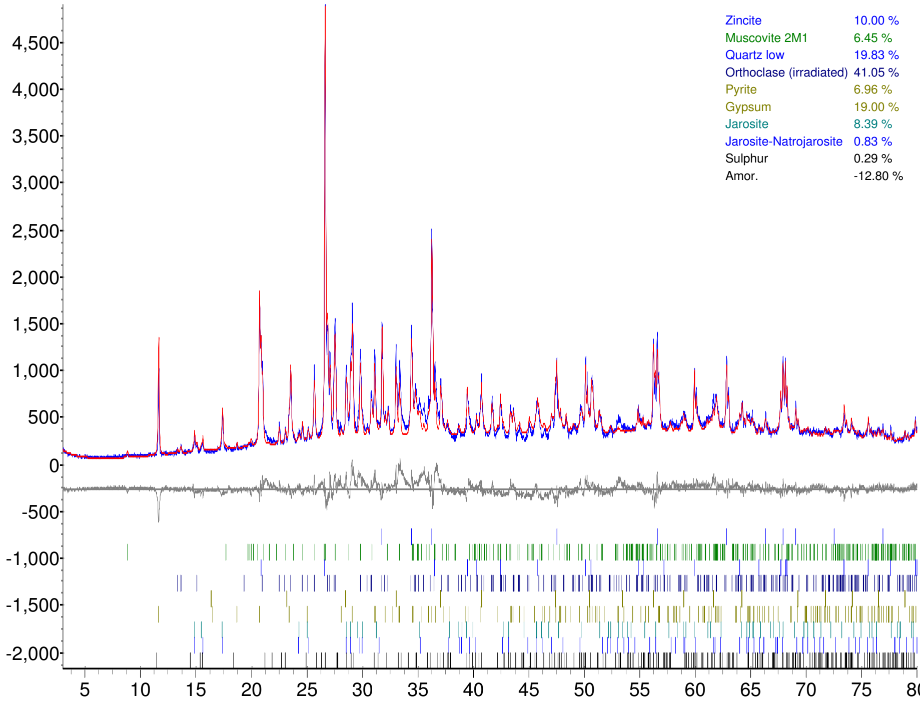

Rietveld refinement model for fine unoxidized tailings.

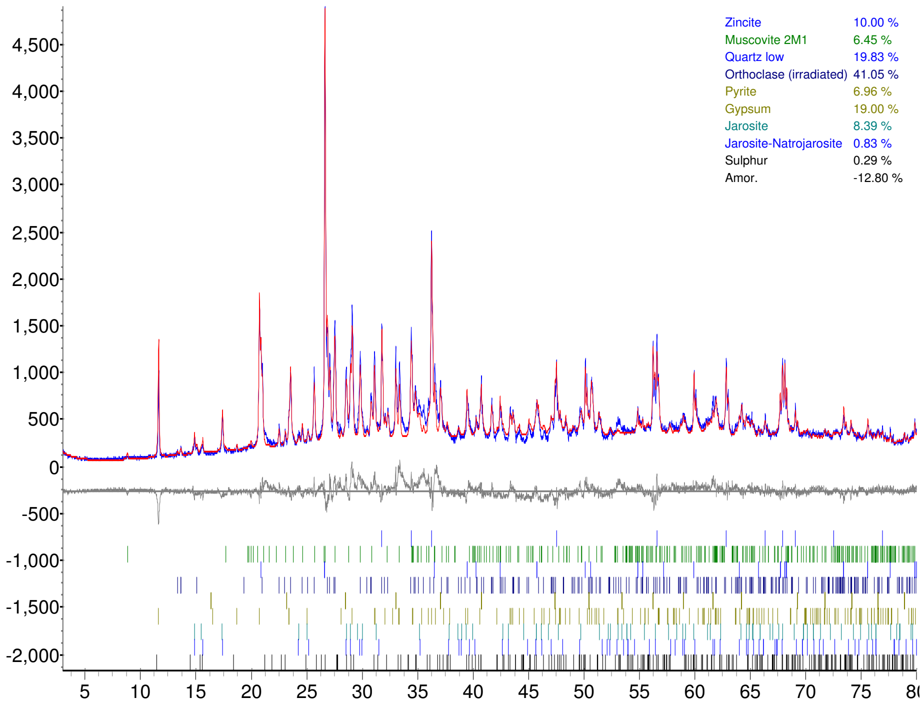

Rietveld refinement model for red oxidized tailings.

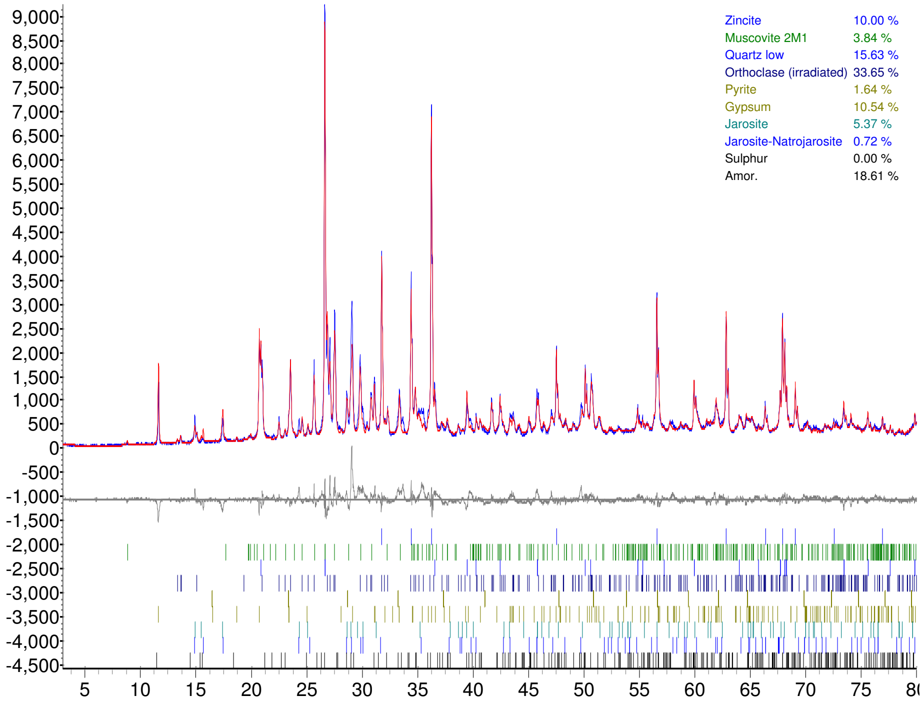

Rietveld refinement model for yellow oxidized tailings.